Absorption and refractive index dynamics in waveguide semiconductor electroabsorbers

Romstad, Francis Pascal

Publication date:
2002

Document Version
Publisher's PDF, also known as Version of record

Ph.D. Thesis

Absorption and refractive index dynamics in waveguide semiconductor electroabsorbers

Francis Romstad
Research Center COM
Technical University of Denmark

Supervisors:
Professor Jørn M. Hvam
Associate Professor Jesper Mørk

March 2002

Abstract

This thesis describes the optical characterization of waveguide semiconductor electroabsorbers with an InGaAsP multi-quantum well heterostructure. The investigations have focused on applying the electroabsorbers as electroabsorption modulators or as saturable absorbers. The components have been manufactured within the Danish research council sponsored SCOOP-programme (Semiconductor COmponents for Optical signal Processing) in collaboration with the Danish company GiGA-An Intel Company. The focus of the SCOOP-programme is to develop new semiconductor components for optical signal processing in telecommunication systems.

Both the amplitude and phase transfer functions of electroabsorption modulators as function of reverse bias and wavelength, are measured using a heterodyne detection technique. With this information, the bias and wavelength dependent α_H-parameter is calculated and so is the electroabsorption modulator response to a 10 Gb/s modulation of the bias. It is concluded that operation close to the absorption edge is advantageous both chirp-wise and with respect to lowering the drive voltage. This however comes at the expense of a higher insertion loss. A comparison between a component with 10 shallow quantum wells and a component with 5 deep quantum wells shows that the shallow 10 quantum wells component is preferable with respect to chirp, extinction ratio and potentially also the insertion loss. Calculations of the refractive index change confirms the measurements and show, that the fabricated electroabsorption modulators can generate high quality pulses for optical fiber transmission.

The all-optical wavelength conversion and demultiplexing capabilities of the electroabsorbers, when operated as saturable absorbers, are investigated using femtosecond laser pulses in an amplitude and phase sensitive heterodyne pump-probe experiment. It is shown that the absorption can be bleached effectively by optical generation of carriers. The absorption recovery is measured as a function of pump pulse energy and reverse bias applied to the component and

it is shown that a 10 ps switching window with 9.6 dB of extinction ratio can be realized. The sign of the refractive index change, induced by optical generation of carriers in the active region, is seen to depend both on the optical power and on the reverse bias applied to the saturable absorber. The trends of the observed refractive index dynamics are explained from a combination of band filling and field screening. It is concluded, that for the right bias and wavelength it is possible to wavelength convert into negatively chirped pulses.

Resumé

Denne afhandling beskriver optiske undersøgelser af halvleder elektroabsorbere med bølgeleder geometri. Komponenternes optisk aktive del er en InGaAsP kvantebrøndsstruktur. Undersøgelserne har fokuseret på anvendelsen af elektroabsorbere som elektroabsorptionsmodulatorer eller som mætbare absorbere. Komponenterne er blevet udviklet under det danske forskningsråd sponsorerede SCOOP-program (Semiconductor COmponent for Optical Signal Processing) i samarbejde med det danske firma GiGA-An Intel Company. SCOOP-programmets målsætning er at udvikle nye halvlederkomponenter til optisk signal processering i telekommunikations systemer.

Både amplitude og fase overføringsfunktionerne af elektroabsorptionsmodulatorerne som funktion af spænding og bølgelængde er blevet undersøgt. Ved brug af denne information, er den spændings og bølgelængde afhængige α_H-parameter blevet udregnet. Elektroabsorptionmodulatorens respons til en 10 Gb/s modulation af spændingen er også blevet udregnet. Derved kunne det konkluderes at operation tæt på absorptionskanten er fordelagtigt med hensyn til en reduktion af chirp og drivspænding, dog med et forøget indsætningstab. Sammenligning mellem en komponent med 10 lave kvantebrønde og en komponent med 5 dybere kvantebrønde viser, at den førstnævnte er både bedre med hensyn til chirp, kontrastforhold og potentielt også indsætningstab. Udregning af den refraktive indeksændring understøtter målingerne og viser, at de udviklede elektroabsorptionsmodulatorer kan bruges til at lave højkvalitetspulser til optisk fibertransmission.

Mulighederne for rent-optisk bølgelængdekonvertering og demultipleksing i mætbare absorbere undersøges ved brug af femtosekund laserpulser i et amplitude- og faseføls omt pumpe-probe eksperiment. Det vises, at absorptionen kan mættes effektivt ved optisk at generere ladningsbærere i den aktive del af komponenten. Absorptions dynamikken er målt som funktion af pumpe pulse energien samt spændingen over komponenten og det bliver vist at et 10 ps transmissions vindue med 9.6 dB i kontrastforhold kan realiseres. Den pumpe inducerede re-

fraktive indeks ændring bliver også målt som funktion af pumpe pulse energien og spændingen over den mætbare absorber. Det bliver derved observeret, at fortegnet for den refraktive indexændring afhænger af spændingen over den mætbare absorber. Princippet for denne afhængighed bliver forklaret ved en kombination af ladningsbærer generation og felt reduktion. Det konkluderes, at ved den rigtige bølgelængde og spænding over den mætbare absorber, er det muligt at bølgelængde konvertere til pulser med negativt chirp.

Preface

The work presented in this thesis was carried out in the Optoelectronics group at Research Center COM, Technical University of Denmark under the supervision of Professor Jørn M. Hvam and Associate Professor Jesper Mørk. I am very grateful for their support and guidance. On the technical side of the thesis work, I would like to thank primarily Paola Borri, presently at Lehrstuhl für Experimentelle Physik EIIb, Universität Dortmund, for introducing me patiently to the laser system and heterodyne pump-probe set-up during the first year of my Ph.D. program. Dan Birkedal has also contributed importantly to maintain a working lab and I am thankful for his invaluable assistance with the always troublesome laser system. I also want to thank all partners in the SCOOP-programme for creating a stimulating work environment and especially Sune Højfeldt and Leif K. Oxenløwe for good companionship. Finally, I wish to express my gratitude towards my family for their invaluable support during my many years of studying.

The work was financially supported by the Danish research council through the SCOOP-programme.

Copenhagen, March 2002
Francis Romstad

Publications

F. Romstad, P. Borri, S. Bischoff, J. Mørk, W. Langbein, and J. M. Hvam, "Sub-picosecond pulse break-up in an InGaAsP optical amplifier," in proceedings to Danish Physical Society Annual Meeting, (1999).

F. Romstad, P. Borri, S. Bischoff, J. Mørk, W. Langbein and J. M. Hvam. "Sub-picosecond pulse distortion in an InGaAsP optical amplifier," in proceedings to European Conference on Optical Communication, ECOC'99 Technical digest II, pp. 28 (1999).

Borri, P. Romstad, F. Langbein, W. Kelly, A.E. Mørk, J. Hvam, J.M. "Separation of coherent and incoherent nonlinearities in a heterodyne pump-probe experiment," Optics Express 7 (2000).

Romstad, F. Borri, P. Mørk, J. Hvam, J. Heinrichsdorff, F. Mao, M.-H. Bimberg, D. "Pulse distortion in a quantum dot optical amplifier," in proceedings to Conference on Lasers and Electro-Optics, CLEO 2000, pp. 471 (2000).

Romstad, F. Borri, P. Langbein, W. Mørk, J. Hvam, J.M. "Measurement of pulse amplitude and phase distortion in a semiconductor optical amplifier: from pulse compression to breakup," IEEE J. Photon. Technol. Lett., 12 pp. 1674-1676 (2000).

S. Hughes, F. Romstad, A. Knorr, P. Borri, J. M. Hvam "Ultrashort Pulse Compression in a Semiconductor Optical Amplifier," in proceedings to Conference on Lasers and Electro-Optics, CLEO 2001, Vol. 2, p. 500-501 (2001).

Mork, J., Yvind, K.,Oxenlowe, L., Skovgaard, P.M.W., Romstad, F., Bischoff, S., Hojfeldt, S., Tersigni, A., Christiansen, L., Nik, A., Ohman, F., Hvam, J.M., Hanberg, J., Hoppe, K., and Lobel, M. "SCOOP-semiconductor components for optical signal processing," Journal of the Danish Optical Society, DOPS-NYT, 16, p. 25 (2001)

L.K. Oxenløwe, E. Hilliger, A. Tersigni, A.M. Nik, S. Højfeldt, F. Romstad, K. Yvind, P.M.W. Skovgaard, K. Hoppe, J. Hanberg "All-optical Demultiplexing and Wavelength Conversion in an Electroabsorption Modulator," in proceedings to European Conference on Optical Communication, ECOC'01, paper Th.B.2.5 (2001).

L.K. Oxenløwe, F. Romstad, A. Tersigni, S. Højfeldt, K. Yvind, P.M.W. Skovgaard, K. Hoppe and J. Hanberg "Characterisation of a MQW Electroabsorption Modulator as an All-Optical Demultiplexer," Conference Proceedings - Lasers and Electro-Optics Society Annual Meeting-LEOS, Vol.1, pp. 36-37 (2001).

F. Romstad, D. Birkedal, J. Mørk and J.M. Hvam "Measurement of the amplitude and phase transfer functions of an optical modulator using a heterodyne technique," in proceedings to Lasers and Electro-Optics Society Annual Meeting, LEOS 2001, Vol.1, pp. 34-35 (2001).

S. Hughes, P. Borri, A. Knorr, F. Romstad, J. M. Hvam "Ultrashort Pulse-Propagation Effects in a Semiconductor Optical Amplifier: Microscopic Theory and Experiment," IEEE J. Sel. Top. Quantum Electron., Vol.7 Issue 4, pp. 694-702 (2001).

F. Romstad, D. Birkedal, J. Mørk and J.M. Hvam "Heterodyne technique for measuring the amplitude and phase transfer functions of an optical modulator," to be published in IEEE J. Photon. Technol. Lett., May 2002 issue (2002).

L.K. Oxenløwe, F. Romstad, A. Tersigni, E. Hilliger, A.M. Nik, S. Højfeldt, K. Yvind, P.M.W. Skovgaard, K. Hoppe, J. Hanberg "All-optical Signal Processing using Electroabsorption Modulators," in proceedings to International Workshop on Optical Signal Processing, Denmark, Nov. 29-30, 2001, p. 57-58 (2001).

F. Romstad, J. Mørk and J.M. Hvam "Absorption and refractive index recovery in an InGaAsP MQW electro-absorption modulator," in proceedings to International Workshop on Optical Signal Processing, Denmark, Nov. 29-30, 2001, p. 59-61 (2001).

Contents

Chapter 1

Introduction

The explosive growth of data traffic in communication networks during the past two decades has forced hardware producers to look for new high-speed solutions. An endless list of services has been provided to the customers, ranging from "old fashioned" voice transfer to live picture broadcast from single customers. At the moment, download speeds are fast enough to stream radio, download short movie clips, have a reasonable two-way audio communication and a low quality visual communication. To provide this to end users, the backbone network has a 10 Gb/s base rate. The backbone is optical whereas the access network is still electrical. The need for electric-to-optic (E/O) converters is obvious. Fast E/O converters are necessary and for the coming upgrading of the 10 Gb/s base rate to 40 Gb/s, light modulators based on the electroabsorption effect in semiconductor multi quantum well structures seem promising. The manufacturing of these components has matured during the last 10 years and companies such as Alcatel (France), Oki (Japan), CyOptics (Israel), and Corning (USA), now have prototypes for 40 Gb/s electroabsorption modulators (EAMs).

The semiconductor electroabsorber has proven itself an incredibly versatile component, not only for realizing operations such a E/O conversion, but furthermore for incorporation in sup-picosecond pulse sources such as mode-locked lasers [1] and is used for wavelength conversion [2], all-optical demultiplexing [3], electrical demultiplexing [4] and clock recovery [4]. The electroabsorber can thus be expected to be an important component for the future telecommunication system, both in the transmitter and detection parts, but also for inline signal processing.

This thesis addresses the issues relating to the application of electroab-

sorbers made for high bit-rate optical signal processing from an experimental point of view. It will be shown, that the components can indeed be used for high speed signal processing both in an E/O scheme and an all-optical (O/O) scheme. Apart from being fast, measurements of the refractive index dynamics will also show, that these components have the capability to generate negatively chirped pulses both in the O/E and the O/O scheme. Hence, precompensation of pulse broadening in standard single mode fiber is possible.

An overview of the physics behind the electroabsorber and a discussion of the component with respect to the functionalities needed in an optical telecommunication system is given in Chapter 2. A presentation of the available alternatives to the electroabsorber is also given. Chapter 3 reports on the wavelength and bias dependence of the absorption for a number of multi-quantum well structures. The results are discussed with respect to finding optimum conditions for operating the components as electrically modulated absorbers. The heterodyne measurement set-up, used for the measurements reported in the last two chapters of the thesis is presented in Chapter 4. In Chapter 5, measurements of the capability of the EAMs to generate high extinction ratio, narrow pulses with low or negative chirp are reported and discussed. Chapter 6 focuses on measurements revealing the feasibility of operating the electroabsorber as a saturable absorber. The recovery time, absorption bleaching and refractive index changes following an optical injection of carriers is investigated.

Chapter 2

The electroabsorber used for optical signal processing

In an optical telecommunication system many different tasks have to be performed. Signals have to be converted from the electrical domain to the optical, and back. In the optical domain, the information can be multiplexed to utilize the full bandwidth of the transmission system. The information has to be switched at the different nodes of the transmission system and possibly regenerated to compensate accumulated fiber loss and cross-talk. For switching or detection, the information must be demultiplexed from the high density information data stream. The clock of the detection has to be recovered from the incoming bit-stream, such as to read the right bits at the right time.

Many components have been introduced or proposed in order to solve these tasks in a simple, effective and fast way. This chapter presents the operation principles of the electroabsorber and how the electroabsorber can be used to perform many of the signal processing tasks necessary in an optical telecommunication system. Alternative components are also presented.

2.1 The waveguide electroabsorber

2.1.1 Component description

The electroabsorbers investigated in this thesis are manufactured from quaternary alloys of Indium (In), Gallium (Ga), Arsenic (As) and Phosphorus (P). The components are grown by low pressure metalorganic vapor phase epitaxy (LP-MOVPE) deposition. In this process the alloys are deposited on an InP wafer with almost monolayer precision. Together with photo-lithography and different etching techniques, waveguide structures can be realized, which can guide an optical mode travelling in the plane of the wafer. The out of wafer plane confinement is done by properly designing the alloys in the layered structure, such that a layer with high refractive index (the separate confinement layer) is "sandwiched" between two layers of lower refractive index. The active material is incorporated within the mode confining layers. The active material of the components presented in this thesis is a so-called multi quantum well (MQW) structure. Figure 2.1 shows a schematic illustration of the layer structure of the component with the waveguide. The n- and p-doped layers on the bottom and top of the component are contacted with metal alloys. This enables the application of an external bias across the structure. A layer of the insulating polymer BCB (Benzocyclobutene) on both sides of the ridge, planarizes the wafer and enables metal contacts extending from the waveguide. The waveguide ridge is 2-3 μm broad, depending on the design. The component length is chosen when the individual components are cleaved from the wafer. The typical length is 100 μm to 300 μm depending on the application.

When the component is cleaved and mounted, the coupling of the light into and out of the component is either done using high numerical aperture lenses or so-called tapered fibers, where the fiber-end is processed into a small lens. The component can be packaged with fibers, a temperature controller and the electrical connection and be directly mounted on a print-board.

2.1.2 The active material

As shown in Figure 2.1, the active material of the electroabsorber is a MQW structure embedded in the intrinsic layer of the p-i-n heterojunction. The MQW structure consists of alternating layers of different band gap material, realized by changing the InGaAsP alloy composition. The electronic states in the low band gap material are so-called quasi-two dimensional, since the motion perpendicular to the layers is restricted. This results in a steplike density of states for low energies, compared to the square-root shaped density of states function for unconfined states. Due to the increased spatial overlap between the electron and hole wavefunctions in the quantum well, the oscillator strength of the bound electron and hole state (the exciton) is increased. The confinement

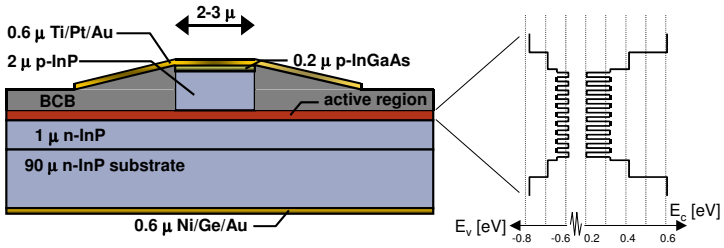

Figure 2.1: Schematic illustration of the electroabsorber waveguide and epitaxial structure. The light travels perpendicularly to the plane of the paper. At the right of the structure is shown a zoom of the active region with the quantum well structure within the separate confinement layer. Figure by L. Oxenløwe (SCOOP/COM).

of the wavefunctions result in a steeper absorption edge, compared to the bulk material.

When an electric field is applied to the component, in the direction of the growth, the optical characteristics are changed. If the potential is increased on the p-side of the component compared to the n-side, the component is so-called forward biased. In that case, the junction potential is lowered and carriers can be electrically injected into the intrinsic region of the p-i-n junction and into the quantum wells. Thereby, the optical field travelling through the active region can experience amplification through stimulated emission. The component is in that case operated as a so-called semiconductor optical amplifier (SOA). If the SOA is not anti-reflection coated, the feedback will, for an increasing current through the component, eventually result in lasing action. The component is then called a semiconductor edge emitting laser. If the potential is lowered on the p-side compared to the n-side the component is reverse biased. Optically injected carriers will in that case be swept out of the intrinsic region due to the high field. When operated with a fixed reverse bias, the component can be used as a field enhanced saturable absorber, where the absorption can be saturated by an optical field, but shown to have a fast recovery due to the fast sweep out of the photogenerated carriers.

When the intrinsic region is subject to an external reverse bias, the optical properties of the states are changed. The quantum well potential is modified and the electron and hole wavefunctions are forced in opposite directions. The change in the optical properties due to the field is called the quantum-confined Stark effect (QCSE) [5].

The QCSE includes the quantum confined Franz-Keldysh effect (QCFKE). The QCFKE describes the influence of a field on the quantum well states, neglecting the excitonic effect. Figure 2.2 shows a schematic illustration of

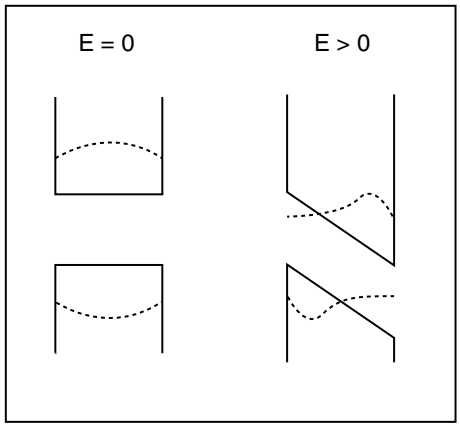

Figure 2.2: Schematic illustration of the QCFKE. The quantum well barriers are assumed infinite and only the lowest energy state is shown. By applying a field perpendicular to the quantum wells (E), a finite penetration of the wavefunction into the band gap is possible and a shift of the state energies is observed, resulting in a finite absorption probability below the zero field band gap.

the QCFKE. When the field over the quantum well is non-zero, the potential depends on the position in the quantum well. The barriers are here infinite. When the field is applied, the wavefunctions will experience a finite penetration into the band gap and a shift in the state energy and thereby effectively enable absorption below the band gap. The effect of the QCFKE is also to reduce the overlap between the electron and hole wavefunctions, which results in a weaker transition strength.

The QCSE also includes the influence of the field on the quantum well exciton. Not including the quantum well potential, the external field will distort the Coulomb potential as shown in Figure 2.3. The distorted Coulomb potential has no more truly bound states and therefore the exciton lifetime decreases and a broadening of the exciton absorption line is observed. The field also effectively "widens up" the Coulomb potential resulting in a shift of the exciton resonance to lower energies [5].

The QCSE makes it possible to change the absorption at a specific wavelength by changing the reverse bias applied to the component. When the reverse bias is increased, the absorption edge red-shifts and increases the absorption below the band gap. Figure 2.4 shows a schematic illustration of the red-shift and reduction of the absorption with increasing reverse bias. If the wavelength of the incoming field is, as indicated by the dashed arrow, the absorption will increase with increasing reverse bias. A component working by these principles

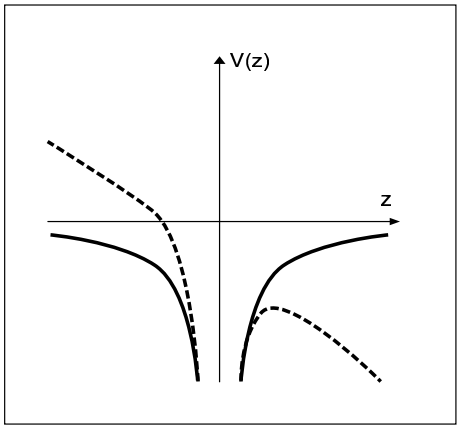

Figure 2.3: Schematic illustration of the Coulomb potential, binding the electron and the hole into an exciton. The full line is the potential without an external field, while the dashed line shows the potential with an external field. The field "widens up" the potential and enables the dissociation of the exciton and results in a red-shift and broadening of the exciton resonance.

is called an electroabsorption modulator (EAM).

The light polarization is an issue in MQW based components. Due to the different dipole matrix elements between TE and TM polarized light and the light and heavy hole states, the components have a polarization dependent absorption. The use of tensile strained material allows one to shift the material light-hole band gap with respect to the heavy-hole band gap and equalize, to some degree, the TE and TM absorption [6, 7, 8, 9].

2.2 The transmitter

The transmitter is very important in an optical telecommunication system, since all electrical-to-optical conversion is done in a transmitter. The typical transmitter used for 10 Gb/s optical systems is the directly modulated DFB semiconductor laser. However, operation above 10 Gb/s is very difficult due to relaxation oscillations and capacitance limitations. Only few experiments on 20 Gb/s direct modulation of semiconductor laser have been reported [10, 11]. No 40 Gb/s direct modulation of semiconductor lasers has, to this authors knowledge, been reported. Operation of the directly modulated laser as a transmitter, is schematically shown in Figure 2.5 a). The laser modulator has also the disadvantage of generating chirped light pulses when modulated

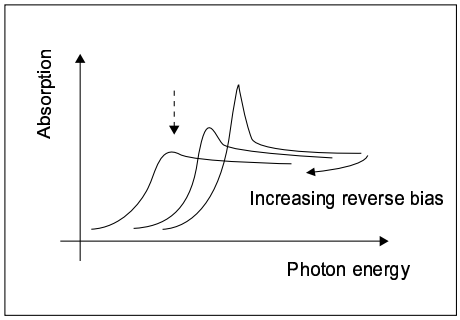

Figure 2.4: Schematic illustration of the absorption edge, including the exciton states. As the reverse bias is increased, the absorption edge red-shifts, the exciton resonance broadens and the transition strength of the states is reduced. Photons with energy indicated by the dashed arrow will experience an increased absorption with increased reverse bias.

fast, explained by refractive index change accompanying the carrier density change. The coupling between the gain and the refractive index, results in an blue-shifted leading pulse edge and a red-shifted trailing pulse edge. The blue components travel faster in a standard single mode fiber in the 1550 nm window than the red. Therefore the chirp results in a faster broadening of the pulses, than if the pulses where not chirped. The directly modulated laser is however a very simple transmitter and is therefore extensively used at bit-rates up to 10 GB/s.

The Lithium Niobate ($LiNbO_3$) modulator has facilitated high speed modulation. The $LiNbO_3$ modulator is an external modulator operating on the principles of the Mach-Zehnder interferometer, where the electro-optic $LiNbO_3$ acts as phase shifters in the two arms (schematically shown in Figure 2.5 b)). By external modulator is meant that the modulator is separate from the light source. Because the refractive index dependence on the externally applied field is small, the phase shifting elements have to be several centimeters. The electrodes contacting the phase shifting elements are of the so-called travelling type, where the electrodes are designed in such a way, that they represent a waveguide for the high frequency electric field. For the right design, the optical and the RF velocity can be matched, resulting in a much higher bandwidth due to the reduced capacitance. Having lumped element electrodes, the bandwidth would be limited to below 1 GHz [12]. In the last years, companies such as Agere, Corning and Codeon have started to ship 40 Gb/s $LiNbO_3$ modulators. The chirp on the modulated signal can be controlled externally by the offset biases to the phase shifting elements. The modulators can generate pulses with zero chirp and even pulses which will initially be compressed by the fiber

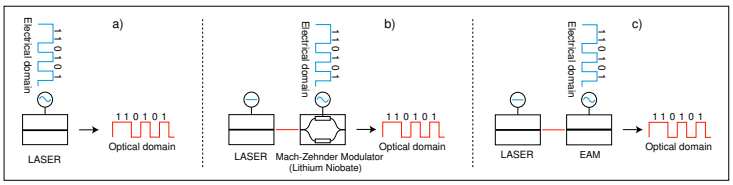

Figure 2.5: Schematic illustration of transmitters mentioned in the text. a) The directly modulated semiconductor laser, b) the $LiNbO_3$ external modulator and c) the external EAM.

dispersion [12]. The $LiNbO_3$ is polarization dependent. The drive voltage is typically ∼3 V peak-to-peak for 40 Gb/s modulation.

EAMs with a MQW active region have also shown bandwidths above 40 GHz, see for example [6, 13]. The EAM as an external modulator is schematically shown in Figure 2.5 c). For operation at 1550 nm both the InGaAsP/InGaAsP and the InGaAs/InAlAs material systems have used successfully [6]. Compared to the $LiNbO_3$ modulator, the EAM is small and can be integrated with the light source, for example a DFB laser. More than 40 GHz bandwidth has been demonstrated using an EAM-integrated DFB laser [14]. The EAMs can also be made polarization insensitive and properly designed EAMs have been demonstrated less than 1 dB of polarization dependent loss [6]. The drive voltage is typically 3 V peak-to-peak. A refractive index change also accompanies an absorption change in EAMs [15, 16]. As with $LiNbO_3$ modulators, it is possible to generate pulses with a chirp that initially compensates the fiber dispersion induced pulse broadening [17, 18]. Chapter 5 will look into the details of the chirping properties of the EAMs made during this project. No companies are, to this authors knowledge, shipping 40 Gb/s EAM modulators. However, Alcatel in France, Oki in Japan CyOptics in Israel and Corning in the US have all 40 Gb/s InP based EAM in their product portfolio. Figure 2.6 shows a realized 40 Gb/s modulation of the absorption in a packaged EAM developed in the SCOOP-programme. The electrical signal has a 2.6 V_{pp} amplitude and the offset bias is -1.2 V. The optical signal has a 7.45 dB extinction ratio.

EAMs are also successfully used for generating short pulses. Generation of pulses with 4–5 ps intensity-FWHM (full width half maximum) were demonstrated using a 40 GHz sinusoidal modulation, with a 2 V amplitude [19]. In an other experiment, 4.1 ps pulse were generated by modulating the bias with a 20 GHz sine function, however with 10.1 V of drive voltage [20]. A 10 GHz pulse train of 200 fs pulses has also been generated using an EAM and a compressive piece of fiber [21]. Figure 2.7 a) shows, that by applying a sinusoidal modulation (10 GHz) of the reverse bias to an EAM a 13 dB extinction ratio, 30 ps intensity-FWHM, 10 GHz pulse train can be generated. The EAM

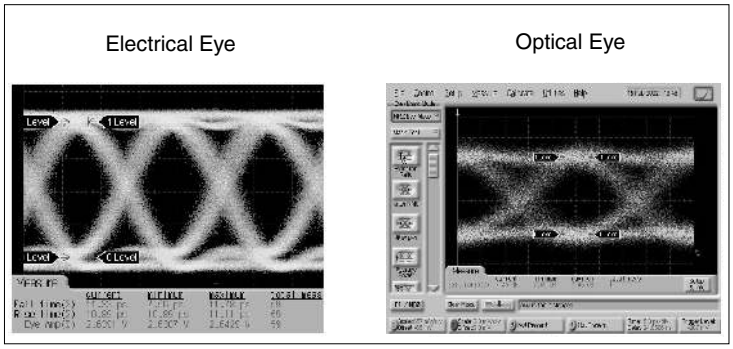

Figure 2.6: The 40 Gb/s NRZ electrical signal applied to a SCOOP-EAM (eye shown) and the resulting optical eye. The electrical signal has a 2.6 V_{pp} amplitude and the offset bias is -1.2 V. The extinction ratio of the optical signal is 7.45 dB. The figure is kindly borrowed from M. Løbel (GiGA-An Intel Company).

was manufactured within the SCOOP-programme. In an other configuration, the electroabsorber is incorporated in a laser cavity and acts as a saturable absorber. Thereby the pulsed laser action of the laser becomes preferable and modelocking can be realized [22, 23, 24]. In Figure 2.7 b) is shown the autocorrelation of a 1.8 ps intensity-FWHM pulse generated by a external cavity modelocked laser [1]. The modelocked laser was developed within the SCOOP-programme.

2.3 Wavelength conversion and regeneration

One of the ways to pack information closely and thereby use the full bandwidth of optical fibers, is by so-called wavelength division multiplexing (WDM). Here, each information channel, having a specific wavelength (different from the others) is transmitted in a single fiber. Record experiments with hundreds of closely spaced channels with each 10 Gb/s of information have been realized [25, 26]. In a WDM system, the individual wavelengths can be chosen in order to connect certain destinations. Therefore, switching of information in the nodes of the WDM system can be realized by converting the wavelength of the incoming bit-pattern to a new wavelength, in order to reach the correct destination. The operation is called wavelength conversion and different components are typically mentioned in connection with this operation.

Four-wave mixing (FWM) in either an optical fiber or a SOA is an instantaneous process, which has been used to wavelength convert [27, 28]. The optical signal is mixed with a CW or pulsed probe and the conjugate signal

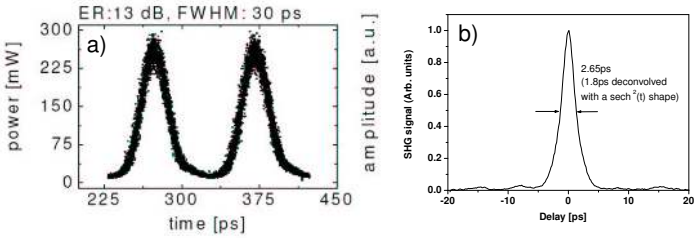

Figure 2.7: a) Optical pulse train generated by sinusoidal modulation of the reverse bias of an EAM with a 10 GHz electrical signal. The pulses have 13 dB of extinction ratio and a 30 ps intensity-FWHM. The EAM was manufactured within the SCOOP-programme. The figure has kindly been borrowed from L. Oxenløwe (SCOOP/COM). b) A 1.8 ps intensity-FWHM pulse, generated by a external cavity modelocked laser with a field enhanced saturable absorber region. The figure is borrowed from K. Yvind (SCOOP/COM).

generated in the FWM process becomes frequency shifted. Up to 200 Gb/s wavelength conversion has been realized in a SOA [29]. Wavelength conversion using cross-gain modulation in SOAs has been shown at 100 Gb/s [30]. In that case, the signal saturates the gain of the SOA and can thereby control the transmission through the component at an other wavelength. Interferometric wavelength converters based on SOAs as the phase shifting element have shown very high speed. For example with the UNI configuration (Ultrafast-Nonlinear Interferometer), 80 Gb/s wavelength conversion has been realized and with in the DISC configuration (Delayed-Interference Signal-wavelength Converter) 168 Gb/s has been shown [31, 32]. Monolithic interferometric wavelength converters have also been realized and are more easy to handle compared to the UNI and DISC. Speeds have until now been limited to 40 Gb/s [33] and the complexity of these components challenges the manufacturing.

Electroabsorbers used as wavelength converters are a good alternative to the above mentioned components and cross-absorption modulation has been shown to enable 40 Gb/s wavelength conversion [2]. In that case, the electroabsorber is operated as a saturable absorber where the incoming signal bleaches the absorption and thereby enables the transmission of light at an other wavelength. The all-optical regenerative properties of wavelength converters are also an important function in the optical transmission system. Reshaping distorted signals and retiming has been realized in SOA based interferometric regenerators at 40 Gb/s [34] and in electroabsorbers both at 10 Gb/s and 40 Gb/s [35, 2].

Figure 2.8 shows the realized wavelength conversion in a saturable absorber. The component was manufactured within the SCOOP-programme. A 10 Gb/s

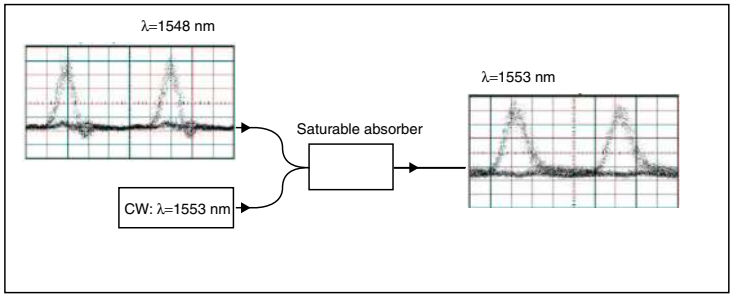

Figure 2.8: All-optical wavelength conversion on 10 Gb/s RZ pulses using a saturable absorber. The incoming signal is wavelength converted from 1548 nm to 1553 nm. The component is manufactured within the SCOOP-programme. Measurements done by from L. Oxenløve (SCOOP/COM).

return-to-zero (RZ) signal was wavelength converted and regeneration was also observed [3]. Chapter 6 reports on the measurements of speed and chirping properties of the saturable absorber.

2.4 Demultiplexing

The optical time division multiplexed (OTDM) system works by delaying each of the base-rate channel (working with return-to-zero (RZ) formats) by a certain amount of time with respect to the next channel. The channels are then all coupled into the same fiber, resulting in a train of light pulses with the multiplexed signal. Figure 2.9 shows the principle of a OTDM system with 4 base-rate channels working for example at 10 Gb/s RZ. By delaying each channel appropriately with respect to the previous channel, the multiplexed channels will not overlap temporally. After transmission, the channel containing the information for a certain destination has to be demultiplexed from the OTDM signal before detection. Demultiplexing is realized by opening a transmission window in time, which only transmits the pulse of interest. Demultiplexing from 1.28 Tb/s to 10 Gb/s has been realized in a so-called non-linear loop mirror, based on instantaneous nonlinearities in fibers [36]. However, fiber based demultiplexers are cumbersome due to the several meters of fiber necessary. Four-wave-mixing in fibers has also been realized with 500 Gb/s to 10 Gb/s demultiplexing and 200 Gb/s to 10 Gb/s demultiplexing using four-wave-mixing in a SOA has equally been shown [37, 38]. With the more compact monolithically integrated Mach-Zehnder interferometer, with SOA phase shifting elements, 160 Gb/s to 10 Gb/s demultiplexing has been demonstrated

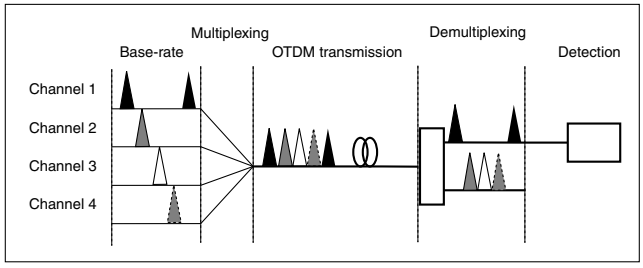

Figure 2.9: Schematic illustration of the principle of optical time division multiplexing (OTDM). Here, 4 base-rate channels are delayed with respect to each other and combined into one fiber. After transmission, the channel of interest can be demultiplexed from the OTDM signal and detected.

[39, 40]. 160 Gb/s to 10 Gb/s demultiplexing has also been realized in SOA based hybrid demultiplexers such as the UNI and the SLALOM (Semiconductor Laser Amplifier in a LOop Mirror) [41, 42])

Both electrical and optical demultiplexing is possible in electroabsorbers. For electrical demultiplexing, the switching window is realized by electrically modulating the absorption (the electroabsorber is operated as an EAM), whereas for optical demultiplexing, the absorption is modulated by optical carrier generation (the electroabsorber is operated as a saturable absorber). Electrical demultiplexing from 160 Gb/s to 10 Gb/s has been shown using two EAMs in series, the so-called tandem configuration [4]. All optical demultiplexing from 40 Gb/s to 10 Gb/s has been reported using a saturable absorber [3], and 80 Gb/s to 10 Gb/s has been performed by L. Oxenløwe (SCOOP/COM), however not with an error free conversion [3, 43]. Figure 2.10 shows the 80 Gb/s OTDM signal comprising 8, 10 Gb/s channels. The limitations in the detection equipment prohibits a good measurement of the high bit-rate OTDM signal. After all-optical demultiplexing in the saturable absorber, one of the 10 Gb/s channels is observed to be extracted from the 80 Gb/s signal.

2.5 Thesis objectives

The work presented in this thesis has focused on characterizing the electroabsorbers as stand-alone components and not as a part of a transmission system. This characterization is necessary before the limitations of the components within a full system can be understood. The thesis work has two goals. The one is to experimentally characterize the absorption and refractive index dynamics in the EAM. From these measurements the optimal points for operation

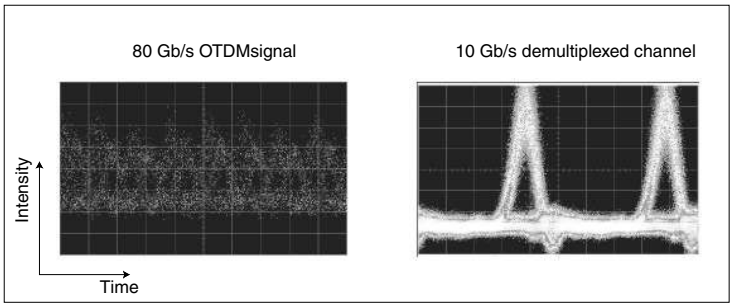

Figure 2.10: 80 Gb/s OTDM signal and the optically demultiplexed 10 Gb/s channel. The demultiplexing was done using a SCOOP saturable absorber. Measurements done by L. Oxenløwe (SCOOP/COM).

of electroabsorbers as transmitters, with respect to extinction ratio, chirp and insertion loss are discussed. The second goal is to characterize the absorption and refractive index dynamics in saturable absorbers, for operation as all-optical wavelength converters and demultiplexers. This is done in order to investigate how fast the components are, describe the refractive index dynamics and discuss the optimal operation condition with respect to speed, extinction ratio and chirp. The following chapter will present some of the basic characterizations of the EAMs. The investigations were performed in order to find an optimal active region design and estimate the loss terms adding to the EAM insertion loss.

Chapter 3

Basic EAM characterization

Before the more advanced investigations of the electroabsorbers are presented, this chapter reports on the more basic characterizations of the EAMs. By basic is meant characterization of the absorption spectra and the insertion loss of the components. The EAMs have been developed from "scratch" and therefore basic characterizations have been performed extensively. Different designs of the active region have been tried. The goal has been to increase the extinction ratio for a given drive voltage and lower the component insertion loss. The typical design issues concerning EAMs are presented and discussed together with the measurements. Finally, calculations of the absorption spectra are shown to fit the measured absorption spectra well.

3.1 EAM design considerations

To design an electroabsorber for high speed operation as an EAM is not a simple task and involves having experience within many fields. The areas of expertise include the knowledge on optical mode control, epitaxial growth, band gap and wavefunction calculations, carrier dynamics and electrical properties such as device impedance and the resulting demands on the drivers. The work on designing and growing the EAM epitaxial structures has primarily been done by K. Yvind (SCOOP/COM), J. Hanberg (GiGA-An Intel Company) and S. Højfeldt (SCOOP/COM). A fulfilling description of the issues involved in the design, epitaxial growth and processing is beyond the scope of this thesis. Therefore only a short overview of the considerations with respect to EAM optimization will be given, such as to understand the reasons for the realized EAM designs and the following investigation reported in this chapter.

The focus of the EAM design is set on optimizing the absorption change for a given voltage swing. In that case, the red-shift of the absorption edge is sought to be as large as possible, as function of the reverse bias. The shift of the absorption edge includes a shift of the conduction band states and the valence band states. The effective heavy hole mass is much larger than the effective electron mass in the InGaAsP alloys used[1]. Therefore the hole states have a smaller zero-point energy, for a structure where the well depths for the hole and electrons are equal. Heuristically, the states close to the bottom of the well "experience" a higher energy shift with changing electric field, because these states follow closely the field distorted quantum well [44]. Hence, the red-shift of the absorption edge is primarily due to the shift of the hole states. Therefore, to maximize the red-shift of the absorption edge, it is primarily advantageous to reduce the hole zero-point energy. This is done by reducing the hole well depth [45].

Another consequence of the difference in zero-point energy of the electron and hole states, is the reduced attenuation of the electron states in the barrier, compared to the hole states. For a balanced structure, where the electron well depth is increased compared to the hole depth, the penetration probability can be made equal [45]. Thereby the quenching of the transition due to premature dislocation of the electron state can be prohibited. With this optimization the quantum well structure becomes so-called balanced, having low hole barriers and high electron barriers, as illustrated in Figure 3.1. Calculations by Yip et al. on InGaAsP alloys, showed that the overlap between the electron and hole states, for flat bands (at zero field), is maximized for a electron well depth 9 times the depth of the hole well [45]. When an electric field is applied perpendicular to the quantum wells, the electron and hole wavefunctions start to

[1]The light hole states are neglected in this discussion, because the absorption of TE polarized light, of interest here, is mainly due to the heavy hole-electron transition. If not otherwise mentioned, the hole will be the heavy hole.

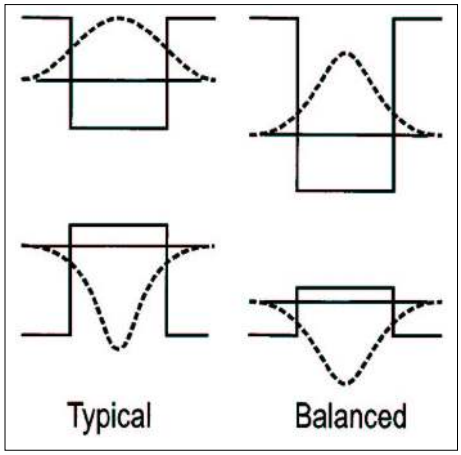

Figure 3.1: Schematic illustration of unbalanced and balanced quantum wells. In the unbalanced quantum well, the electron state is less confined than the hole state due to the lower electron mass. The balanced quantum well equalizes the confinement of the electron and hole state by increasing the height of the electron barrier and optimizes thereby the transition strength. At the same time the hole barrier is lowered, resulting in a lower hole zero-point energy, which increases the energy shift per unit field. From [45].

leak into and through the barriers with different rates. The optimized ratio between the electron and hole well depths, resulting in a equal leaking for the electrons and holes, depends on the field applied to the component and can therefore not be optimized for all biases [45]. Still, the electron wells should, generally, be deeper than the hole wells. It should here be pointed out, that an optimized structure for a large red-shift per unit field is not at the same time optimized for keeping the overlap between the electron and hole state in the quantum well as high as possible. This is because an important red-shift is accompanied with an important spatial shift of the states to the low energy sides of the wells. Therefore, an optimal design has to be based on the specific demands for the modulator and a compromise between the absorption edge red-shift and quenching.

A large quantum well width ensures a low zero-point energy, advantageous for the absorption edge red-shift. This also results in an increased spatial polarization of the electrons and holes in the quantum well, when an electric field is applied. The typical well width for EAMs is 10 nm or less, being somewhat inferior to the exciton Bohr radius, hence assisting in bolstering the state [45].

The limited output power of the EAM driver limits the magnitude of the ex-

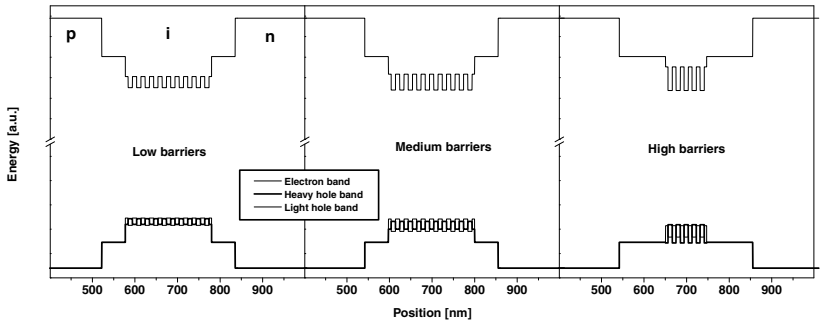

Figure 3.2: Band lineup calculations for the low, medium and high barrier components performed by S. Højfeldt (SCOOP/COM).

ternal field applicable to the EAM. Since the EAM has a non-zero capacitance, being a combination of the junction capacitance and the electrical pad capacitance, the field applied to the intrinsic region will be reduced with increasing modulation frequency. It is therefore important to reduce the component capacitance. The junction capacitance can be reduced by increasing the intrinsic layer thickness and decrease the component dimensions. Increasing the intrinsic region has however the consequence of reducing the electric field over the quantum wells for a given drive voltage. However a wider intrinsic region can contain more quantum wells, increasing the overlap between the optical field and active region. Decreasing the component size, such as the length also reduces the total absorption change induced by a given drive voltage. Reducing the ridge width has consequences on the optical mode size, possible resulting in a multimode waveguide.

Finally, the escape time from the quantum wells is also an issue. The optically generated carriers have a longer escape time from deep quantum wells than for shallow quantum wells, because the high barriers reduce the escape probability. The modulation bandwidth of the EAM can therefore be limited by pile-up of carriers. Hence, low barriers are advantageous with respect to carriers escape. The speed limitations due to the carrier dynamics will be investigated in Chapter 6.

All these considerations resulted in the manufacturing of 3 epitaxial structures. The growth numbers are G286, G285 and G287 and will in the following be called low barrier component, medium barrier component and high barrier component, respectively. The energy band diagram for the intrinsic region of the components are shown in Figure 3.2. The calculations were done by S. Højfeldt (SCOOP/COM) assuming Tersoff's theory for lineup [46]. The heavy hole-electron band gap is $\sim$1475 nm.

The high, medium, and low barrier components have electron band off-sets of approximately 150 meV, 70 meV, and 50 meV, respectively. The hole band off-sets are about the half of the electron band off-sets.

The intrinsic layer thicknesses have in all cases been chosen to be 310 nm. The electric field over the intrinsic region is therefore the same for all components for a given applied bias. Hence, the components can be directly compared, with respect to drive voltage and offset bias. The low barrier and medium barrier components have 10 quantum wells, while the high barrier component has only 5 quantum wells. The fewer quantum wells in the high barrier component are due to the fact, that the deep wells in this structure resulted in a higher strain. This prohibited the successful growth of more quantum wells without generating unwanted dislocations in the structure. The well width for all the structures is 10 nm, which is also equal to the barrier width for the three structures, except for the high barrier component having 8.8 nm barrier widths. The reduced barrier width for this epitaxial structure is due to the strain compensation necessary in the structure. For all of the structures grown, the light hole to electron transition is of type two, stating that the light hole wavefunction is confined at the position of the electron barrier. This results in a reduced light hole-electron transition strength at zero electric field compared to the heavy hole-electron transition. However, for an increasing electric field, the light hole and electron wavefunctions increase their overlap, opposite to the heavy hole and electron wavefunctions. In all structures, the hole barriers were made lower than the electron barriers in an effort to compensate the premature delocalization of the electron states. The hole barrier heights were chosen to be low, in order to increase the field dependent red-shift of the states. However, the lower limit of the well depth is determined by the thermal effects. These effects play a role when the localization potential becomes comparable to the thermal energy ($kT \sim$25 meV).

No efforts to reduce the polarization dependent absorption was done. The EAM is expected to be operated close to the light source, having a well defined polarization, typically TE. Lowering of the polarization dependent absorption of the EAM is not crucial, since polarization maintaining fibers can be used between the light source and the modulator.

The purpose of the three structures was primarily to see if the well depth differences had any effect on the speed limitations and the absorption change attainable for a given drive voltage. From the conclusions drawn from the measurements on these structures, new and optimized EAM components could be designed. The measurements presented in this chapter are only the static characterizations of the components. The dynamic measurements were performed by A. Tersigni (SCOOP/COM), L. Oxenløwe (SCOOP/COM) and K. Hoppe (GiGA-An Intel Company) and are reported in the thesis of L. Oxenløwe [47].

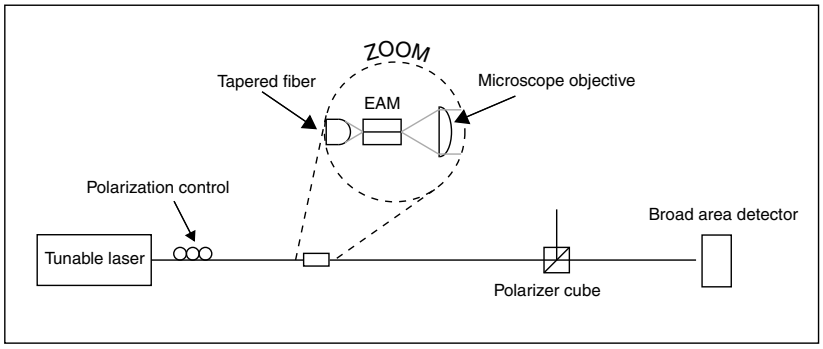

Figure 3.3: Schematic illustration of the experimental set-up used to measure the absorption spectra as function of wavelength and polarization of the light, and the reverse bias applied to the EAMs.

3.2 Experimental set-up

A set-up, as illustrated in Figure 3.3, was built to measure the absorption of the EAMs as function of wavelength and reverse bias. A CW laser, tunable from 1461 nm to 1605 nm delivers the input optical power. A polarization controller follows the lasers and enables the control of the polarization state of the light. To couple the light into the waveguide of the component, a tapered fiber from Optospeed is used. The outcoming light from the component is collimated using a Thorlabs aspheric microscope lens. The numerical aperture of the lense is 0.65. Both the tapered fiber and the microscope lens are mounted on XYZ controllable stages. The collimated light is pointed towards a Hitachi broad area Germanium detector. The detector diameter is 5 mm, ensuring that all light collimated by the microscope lens is detected. A polarizer cube is inserted between the microscope lens and the detector. The polarizer cube is used together with the polarization controller, to set the polarization of the laser light to either TE or TM. The distance between the microscope lens and the detector is $\sim$ 1.5 m. The current from the detector is amplified using a current preamplifier. The voltage from the preamplifier is measured on a 120 MHz digital oscilloscope. A function generator is used to bias the component. The component is mounted on a Peltier cooler, and the temperature is set to approximately 20 deg Celcius. The bias is applied to the component using a needle, contacted to the component metal pad using a XYZ controller stage.

To coarsely align the tapered fiber to the EAM, the EAM is forward biased and the power entering the tapered fiber is detected and maximized by moving the tapered fiber tip with respect to the waveguide. The optical power coupled into the tapered fiber is measured by a power meter inserted at the position

of the CW laser. The microscope lens is aligned by the same procedure, using the broad area detector to detect the optical power.

The fine adjustment of the coupling into and out of the component is done by coupling optical power into the component, oscillating the reverse bias over the component with a few tenths of Hz and then detect the out-coupled power on the broad area detector. The signal from the detector is displayed on the oscilloscope, which is triggered by the function generator. Thereby the component absorption-bias transfer curve is measured. A well optimized coupling shows both a low component loss at 0 V and a high extinction ratio. The two factors can not be optimized independently. Scattered light can be misinterpreted as a low insertion loss, however, resulting in a low extinction ratio.

The input optical power to the components is –12 dBm. The power is measured at the tip of the tapered fiber by focusing the fiber tip onto the broad area detector. The power from the laser is -8.1 dBm, but the insertion of the polarization controller and the fiber connectors add a loss of 3.9 dB.

An extinction between the TE and TM polarizations of the laser light of 20 to 30 dB was possible, using the polarization controller. The polarizer cube used in the set-up is specified to 30 dB of extinction between the orthogonal polarizations. The polarization of the laser light showed negligible variation with the laser wavelength.

When the component is aligned, the actual measurement of the absorption can be done. The component bias is set to the desired dc value and the laser wavelength is controlled by a Labview program through a standard GPIB interface. The data acquisition is equally done within the Labview program via a GPIB interface to the oscilloscope which is measuring the dc voltage from the preamplifier.

Because the facets are not anti-reflection coated, the measured absorption spectra show important Fabry-Perot fringes. The wavelength steps are chosen to be 0.5 nm, ensuring that the Fabry-Perot fringes are not under-sampled. This results in approximately 300 wavelength steps when the wavelength is scanned from 1461 nm to 1605 nm. A single scan takes around 3 minutes.

An important issue is the high dynamical range required for the experiment. Within one scan, above 30 dB of intensity change has to be measured. To follow the large change in intensity, the sensitivity of the preamplifier has to be changed during the acquisition.

The stability of the set-up is also important. Temperature and mechanical drifts can result in altered coupling. Measurements performed with this set-up showed very low or no drift with time. For this reason, the measurements on each device was done with only one optimized coupling.

3.3 Coupling and waveguide losses

The component insertion loss is one of the important issues when dealing with EAMs. The insertion loss is defined as the total loss experienced by light when coupled into and out of the component, when the EAM is set for the "on"-state. With "on"-state is meant the state where the EAM is transmitting. The "off"-state is defined as the state where the EAM is absorbing the light. The insertion loss includes multiple separate loss terms. First of all, a mode mismatch between the fiber mode and the waveguide mode induces a coupling loss into and out off the component. Secondly, loss due to propagation through the waveguide also adds to the insertion loss of the component. Reflection losses at the facets are also important if the component is not anti-reflection coated. All of the above mentioned loss terms are independent of the reverse bias applied to the component and to a certain extent also the wavelength. They are therefore called passive losses of the component. In addition to the passive losses, the insertion loss also contains losses caused by absorption into the electron states in the active region. This can appropriately be called active losses and depends both on the bias applied for the "on"-state and the wavelength of the light to be modulated. The total component loss can be written in equation form as

$$\mathcal{L} = C_{in}(1 - R_{in})C_{out}(1 - R_{out})\mathrm{e}^{-(\alpha_{wg}+\alpha_a(V,\lambda))l} \tag{3.1}$$

Where C_{in} and C_{out} are the input and output coupling losses, respectively. R_{in} and R_{out} are the reflections at the input and output facet of the component, respectively. The passive modal waveguide loss is α_{wg}. The active modal material loss is $\alpha_a(V, \lambda)$, depending on the wavelength (λ) and the bias (V) applied to the component. The length of waveguide is l. In most cases $C_{in} = C_{out}$ and $R_{in} = R_{out}$, which will also be assumed in the following analysis of the measured data.

Figure 3.4 shows the absorption spectrum for one component from each of the previously mentioned wafers. The three components are of equal length, namely 250 μm. The light is TE polarized, and no external electric field is applied to the components. The active material absorption is clearly observed as a component absorption increasing with decreasing wavelength. The absorption is expected to continue increasing with decreasing wavelength. Therefore, the decrease of the absorption for short wavelengths is not well understood. It is not likely to be an excitonic effect, since the built in field of the p-i-n junction is expected to ionize the exciton, due to the low barriers. Measurements on a similar structure by Devaux et al. showed no exciton resonance even at 2 K of temperature [6]. The explanation of this artifact can, at this moment, only be a guess. A possible explanation could relate to a change of the mode in the waveguide, resulting in an altered confinement factor. Calculations by K. Yvind (SCOOP/COM) have shown, that the waveguide indeed changes from

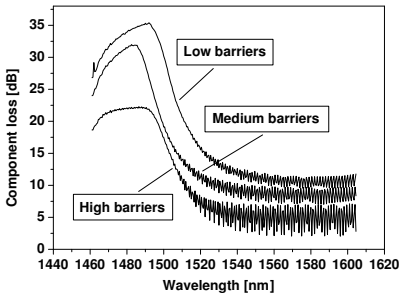

Figure 3.4: Absorption spectra measurements of the absorption edge of the 250 μm long components with low, medium, and high barriers. No external bias is applied to the components. The fringes on the long wavelength side are Fabry-Perot modes. The light is TE polarized.

being single mode to being multimode, when the wavelength is decreased.

The absorption for the high barrier component in the low wavelength part of the spectrum is lower than for the other components and more flat. More scattered light coupled into the detector, probably travelling outside the waveguide, is expected to be the reason.

The losses above ∼1560 nm are wavelength independent and are therefore not due to excitation of the active material, but caused by a combination of coupling losses, waveguide losses and reflections at the facets. From this part of the spectrum the passive waveguide loss can be calculated. The waveguide loss can be found from the ratio between the minimum and maximum power in the Fabry-Perot fringes and the reflection at the facets [48],

$$\mathcal{L}_{wg} = \mathrm{e}^{-\alpha_{wg} l} = \frac{1}{\sqrt{R_{in} \cdot R_{out}}} \frac{\sqrt{r} - 1}{\sqrt{r} + 1} \tag{3.2}$$

The ratio between the maximum and minimum power of the Fabry-Perot fringes is represented by r. In the following the facet reflections are set to 0.3.

Above 1560 nm, the measured max/min ratio of the low barrier component is 1.5 or 1.8 dB. The uncertainty is negligible due to the long wavelength span over which the max/min ratio is found. Equation (3.2) gives a waveguide loss of 5.2 dB or 2.1 dB/100-μm. The total passive device loss is 10.5 dB, which leaves 10.5 dB–5.2 dB= 5.3 dB of coupling loss. Since the component is not anti-reflection coated, 3 dB of the 5.3 dB of coupling loss are due to the reflection of light at the in coupling and out coupling. This finally results in a coupling loss due to the mode mismatch of 1.2 dB per facet. The losses

	Passive IL [dB]	α_w [dB/100-μm]	C [dB]
Low barriers	10.5	2.1	1.2
Medium barriers	8.3	1.6	0.6
High barriers	4.8	0.2	0.7

Table 3.1: Summarized passive (below band gap) component losses. Passive insertion loss (IL) represents the full passive component loss, the waveguide loss (α_w) is the propagation loss in the waveguide, and the coupling loss (C) represents the loss accompanying a coupling from the fiber mode to the waveguide mode. The coupling loss is per facet, not including the reflection.

measured on the components are summarized in Table 3.1.

The total passive losses have an important variation from component to component. The calculations show that the variation in the losses is primarily due to varying waveguide losses, whereas the coupling losses are approximately constant at 1 dB. The variation in the waveguide losses can be explained by varying quality of the waveguide etch from wafer to wafer. Many components showed higher losses and the results presented here are made on the good quality components.

3.4 Active material absorption

The absorption increases when the photon energy is high enough to excite the electron-hole states in the active material of the EAM. This is observed for a wavelength of around 1530 to 1550 depending on the quantum well design, as seen in Figure 3.4. Operation of the components as light modulators below this wavelength is not advantageous with respect to lowering the component insertion loss. However, the optimum operation wavelength of the component also depends on the reachable extinction ratio for a given drive voltage. Figure 3.5 a) shows the absorption spectra for different reverse biases for the low barrier component. As expected, an increase of the reverse bias over the component changes the absorption by shifting the absorption edge. The absorption is increased for all wavelengths. However the most important increase in absorption is observed just on the low energy side of the 0 V absorption edge. This is clearly seen in Figure 3.5 b) where the absorption change (extinction ratio) with respect to the 0 V curve is shown.

An extinction ratio of more that 10 dB can be attained with a 2 V drive voltage at 1513 nm. The active material absorption at 0 V is also shown in Figure 3.5 b). It is observed, that the high extinction ratio is accompanied by 8 dB of active material loss at the "on"-state. Together with the passive losses the insertion loss becomes 18 dB. How large an insertion loss is acceptable is

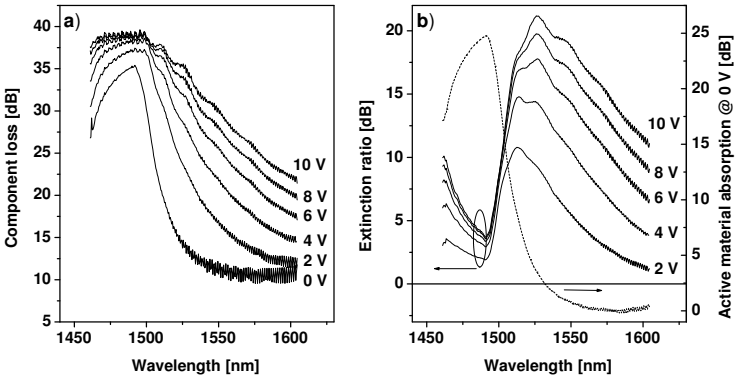

Figure 3.5: Absorption spectrum of the component with low barriers as a function of the applied reverse bias over the component for TE polarized light. a) shows the full component loss and b) shows the extinction ratio as a function of the reverse bias with respect to the 0 V curve. The active material absorption at 0 V is also shown.

difficult to say, since it depends on the CW source providing the light to be modulated and the following transmission system. However, typically, losses should be lower than 10 dB.

Operation at 1550 nm, with a 2 V drive voltage gives only $\sim$ 5.4 dB of extinction ratio. However, the active material loss is only 0.7 dB, which together with the passive losses results in a insertion loss of 11 dB. When anti-reflection coated the insertion loss will be 8 dB.

It is difficult to give an accurate value of the extinction ratio necessary for generating pulses for optical fiber transmission. This value depends on many details such as the fiber length, the pulse chirp, the amplifier noise and the detection scheme to mention a few of the most obvious. However, an extinction ratio of 7–10 dB can generally be a design guideline. Assume that the drive voltage has a 4 V amplitude. The component can then be operated with at least 7 dB of static extinction ratio from $\sim$1500 nm to $\sim$1575 nm. Which shows that a single EAM can easily cover the full C-band (1530 nm to 1565 nm).

Figure 3.6 a) shows the component loss for TM polarized light. The absorption spectra are very similar to the absorption spectra for TE polarized light and the passive loss is only $\sim$1 dB higher than for the TE light. The peak extinction ratio for the 2 V of drive voltage with the "on"-state having 0 V of bias is 11.7 dB (at 1505 nm), a bit higher than for the TE polarized light. At this operation wavelength, the active material absorption is 7 dB. At 1550 nm

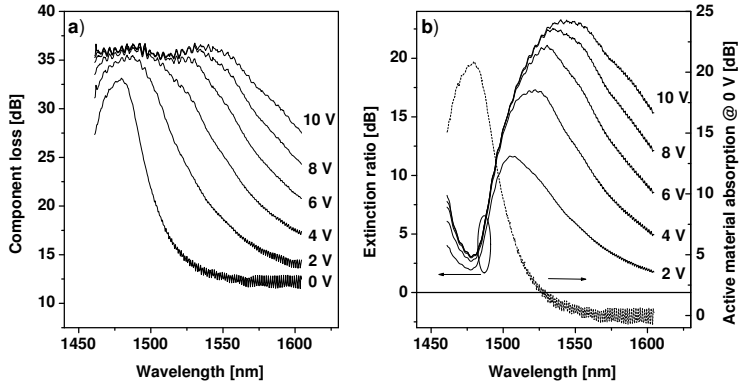

Figure 3.6: Absorption spectrum of the component with low barriers as a function of the applied reverse bias over the component for TM polarized light. a) shows the full component loss and b) shows the extinction ratio as a function of the reverse bias with respect to the 0 V curve. The active material absorption at 0 V is also shown.

the extinction ratio is 5.9 dB for a 2 V bias swing. This is only 0.4 dB higher than for the TE light. The differences between the TE and TM light absorption is less than expected, since no effort has been done to reduce the polarization dependent absorption. A further discussion of the quite complicated origin of the actual polarization dependency, caused by the heavy hole and light hole splitting and the strain in the structure, is not within the scope of this thesis.

A way to reduce the insertion loss, even though the wavelength is close to the absorption edge, is to make deeper wells. This results in a steeper absorption edge, because of the increased transition strength and lifetime of the quantum well states. However, the price is a reduced absorption edge red-shift per unit field and a slow absorption recovery. Figure 3.7 shows the TE absorption spectra for the medium and high barrier samples. From this figure and Figure 3.5 a) the 3 structures can be compared. The expected steeper absorption edge for the high barrier sample, compared to the low and medium barrier component, is not clearly observed. The fewer quantum wells in the high barrier component should reduce the absorption in this component, compared to the others. This could compensate the higher oscillator strength in this component and thereby equalize the absorption to the other components. The red-shift of the high barrier component is expected to be lower than for the low and medium barrier component. This conclusion is difficult to draw from

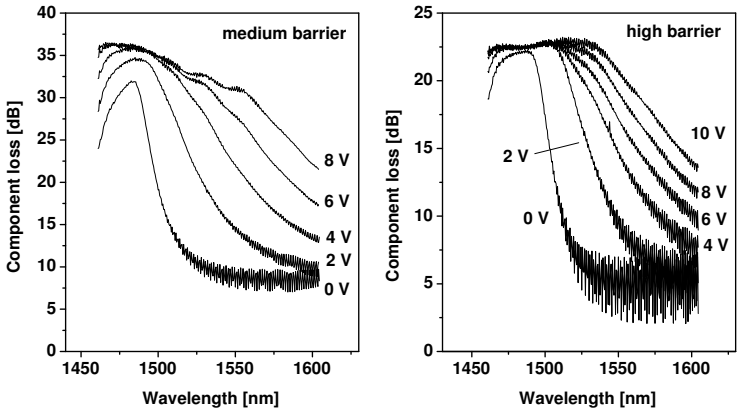

Figure 3.7: Absorption spectra for the medium and high barrier components. The light is TE polarized. Compared to the light and medium barrier components, the high barrier component absorption is clearly limited by scattered light. Except from this, the absorption edge dynamic, is not very different from structure to structure.

the measurements, and the fact that quenching should be lower for the high barrier sample compared to the low and medium barrier component also blurs the picture. However, it can be concluded that the structure have quite the same absorption edge dynamics and size. Assume a 4 V drive voltage. In that case, the extinction, ratio at 1550 nm is 10.7 dB, 13.2 dB and 9.53 for the low, medium and high barrier components, respectively. From this measurement the medium barrier component would be preferable. However, the high barrier component shows the lowest insertion loss of the three. This is primarily due to the better waveguide, not the active material. Chapter 5 looks in more details on the extinction ratio of the low and high barrier components.

In experiments where the EAM absorption was modulated by a high frequency electrical field, it was concluded that the components were all bandwidth limited by the electrical pad capacitance and that any limitations due to carrier escape time from the quantum wells could not be resolved [47]. The high barrier epitaxial structure is difficult to grow due to the high strain, and the structure was abandoned as no clear advantage of this structure compared to the others was seen.

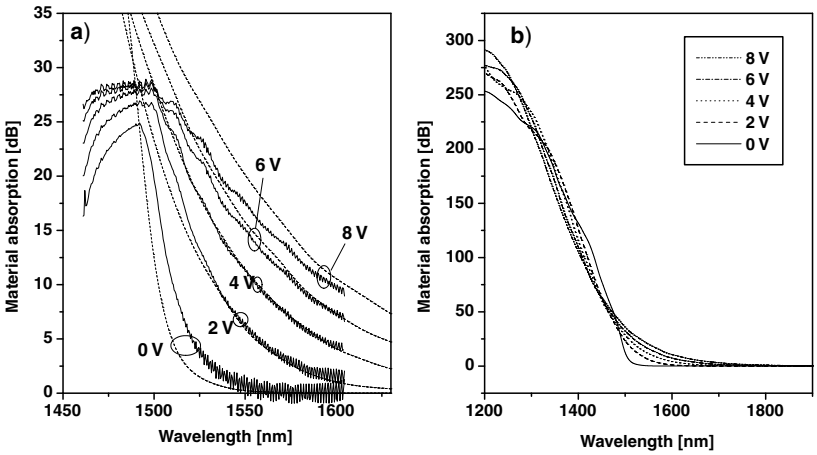

Figure 3.8: a) Calculated and measured TE absorption spectra for the low barrier component as function of the reverse bias. Calculations are performed by S. Højfeldt (SCOOP/COM). A good correspondence is observed. b) The full absorption spectra calculated.

3.5 Absorption spectra calculations

Calculations of the absorption spectra were performed by S. Højfeldt (SCOOP/COM), both as input for his time-dependent simulations and to investigate if there was a good correlation between the measured and calculated results. The absorption spectra calculations take into account the coupling between the wells, which is important due to the shallowness of the wells. Excitonic effects are not included as there are no clear signs of them in the measured spectra. Parabolic bands were used, not taking into account coupling between the valence bands, as in a $\boldsymbol{k} \cdot \boldsymbol{p}$ calculation. Further details on the calculations can be found in the thesis of S. Højfeldt [46]. Figure 3.8 a) shows the calculated and measured TE absorption spectra for the low barrier component. The correspondence is very good. Figure 3.8 shows the fully calculated spectrum. Spectrum calculations for the other components were not as successful, possibly explained by calibration problems of the growth and issues concerning the parabolic approximation of the bands in the calculations [46]. The good correspondence for the low barrier component makes it possible to use the calculated spectra in the calculation of the refractive index change. It will be shown in Chapter 5 that the calculated refractive index change supplements very well the trends observed experimentally.

3.6 Summary

Three EAMs with different InGaAsP quantum well structures have been characterized with respect the absorption spectra and the insertion loss. The quantum well structures differ by the barrier height being low, medium and high and the number of wells. A set-up is built to measure the transmission of the components as function of wavelength (1461 nm to 1605 nm), polarization (TE and TM) and reverse bias applied to the components. From the Fabry-Perot fringe amplitude and the insertion loss at 0 V, the waveguide loss and coupling loss of the component can be calculated. These passive loss terms should not depend on the active region design and differences are attributed to variations accompanying the processing of the components. It is found that the coupling losses are below 1.2 dB per facet and that the waveguide losses are below 2.1 dB/100-μm with 0.2 dB/100-μm as the lowest. The active material contribution to the component transmission shows, as expected, an increasing absorption for an increasing reverse bias applied to the components. Operation close to the absorption edge increases the extinction ratio for a given drive voltage, but also increases the insertion loss. The differences between the three components, due to the different active region designs, are small. The medium barrier component shows a couple of dB higher extinction ratio than the low and high barrier components, at 1550 nm with a 4 V drive voltage and a "on"-state at 0 V. However, a general conclusion on the which structure is best can not be drawn from these measurements. A static extinction ratio of 7 dB or more can be achieved from $\sim$1500 nm to $\sim$1575 nm, with the low barrier component, using a 4 V drive voltage. This shows that a single EAM can easily cover the full C-band.

Measurement of the polarization dependent absorption on the low barrier component showed approximately 2 dB of difference between the TE and TM polarized light, for operation at 1550 nm.

Calculated low barrier TE absorption spectra by S. Højfeldt (SCOOP/COM) have also been shown. Agreement with the experimental measurements is good, showing that excitonic effect are not important in this low barrier structure. Coupling between the shallow wells is important to correctly reproduce the measured spectra.

Chapter 4

The heterodyne measurement technique

Heterodyning (hetero∼different,-dyning∼power) is a word and concept typically encountered when dealing with radio receivers. There, the multi-kHz carrier wave of the radio signal is mixed away, using a local oscillator and a nonlinear diode, leaving only the speech imprinted by amplitude modulation (AM) or frequency modulation (FM). Frequency filters and the heterodyne detection in the radio makes it possible to closely space different radio channels in the frequency domain.

The essence of heterodyning is to measure the beating between two waves. The waves can be acoustic (Hz), as for example the beating between a tuning fork and a "badly tuned music instrument", or it can be radio frequencies as mentioned before. In our case, heterodyning will be done on optical waves, where the carrier frequency is $\approx$ 293 THz. However, as will be shown, the detected heterodyne signal will be at 60 kHz and easily detectable by standard equipment.

The advantages of using a heterodyne detection scheme are multiple when using it for characterizing active waveguide components. Not only is it possible to measure changes of the amplitude transmission of the component, but it is equally possible to measure the phase of the optical field after propagation through the component. As for the radio, it is possible to selectively detect one heterodyne frequency component and disregard all others. This makes it possible to distinguish optical fields with the same optical properties such as polarization, wavelength, direction and position, by shifting the frequency of the optical fields by a few MHz from each other.

When used with short optical pulses, the heterodyne detection becomes very powerful for characterizing waveguide components and enables the mea-

surement of time-resolved transmission and refractive index changes.

The idea of using a heterodyne detection technique together with a pump-probe set-up was first presented by the group of E. Ippen at MIT in the early 1990's [49]. The group presented the first results on gain and index dynamics in semiconductor optical amplifiers on a subpicosecond time scale [50, 51].

In 1996, a similar experimental set-up was built at the Danish Telecom Research facility (TDR). The set-up was used for investigating the coherent effects in semiconductor optical amplifiers, namely four-wave mixing [52]. When TDR was restructured in 1997 the set-up was moved to Mikroelectronik Centret (MIC) at the Technical University of Denmark (DTU). The set-up was rebuilt by P. Borri and W. Langbein in the group of J. Hvam, with an improved detection scheme [53]. The set-up was mainly used for characterizing FWM and gain dynamics in 1.1 μm InAs-InGaAs quantum dot waveguide amplifiers [54, 55].

This chapter will focus on the description of the heterodyne pump-probe set-up and starts with an introduction to the Coherent OPA laser system.

4.1 The laser system

To obtain the required sub-picosecond time resolution, it is necessary to make short optical pulses at the desired wavelength and with the desired pulse energy. For this, a commercial laser system from Coherent Inc is used. The system consists of 4 separate systems

- Coherent Innova 400 ($\sim$24 W of continous wave power).
- Coherent MIRA (Titanium-Sapphire modelocked oscillator).
- Coherent RegA (Titanium-Sapphire regenerative amplifier).
- Coherent OPA (Optical parametric amplifier).

The full system is shown in Figure 4.1 and works as follows. The Innova 400 provides $\sim$8 W of power to pump the Ti:Al_2O_3 (titanium:sapphire) crystal, which acts as the gain medium for the MIRA. The Ti:Al_2O_3 gain peak is at 800 nm. A slit is inserted into the cavity as seen in Figure 4.1. Together with the dispersive prisms (P1 and P2) modelocking of the cavity is possible. The pulsed operation of the cavity decreases the spotsize due to self-focusing in the Ti:Al_2O_3 crystal. Thereby the CW mode experiences higher losses for a reduced slit width than the pulsed mode. The prisms ensure a compensation of the round trip induced dispersion, so as to get a stable operation. The MIRA minimum pulse width is $\approx$ 150 fs with $\approx$ 1.3 W of output power. The repetition rate is $\approx$ 80 MHz.

The components characterized in the previous chapter have an operation wavelength around 1550 nm. To reach this wavelength range with the Ti:Al_2O_3

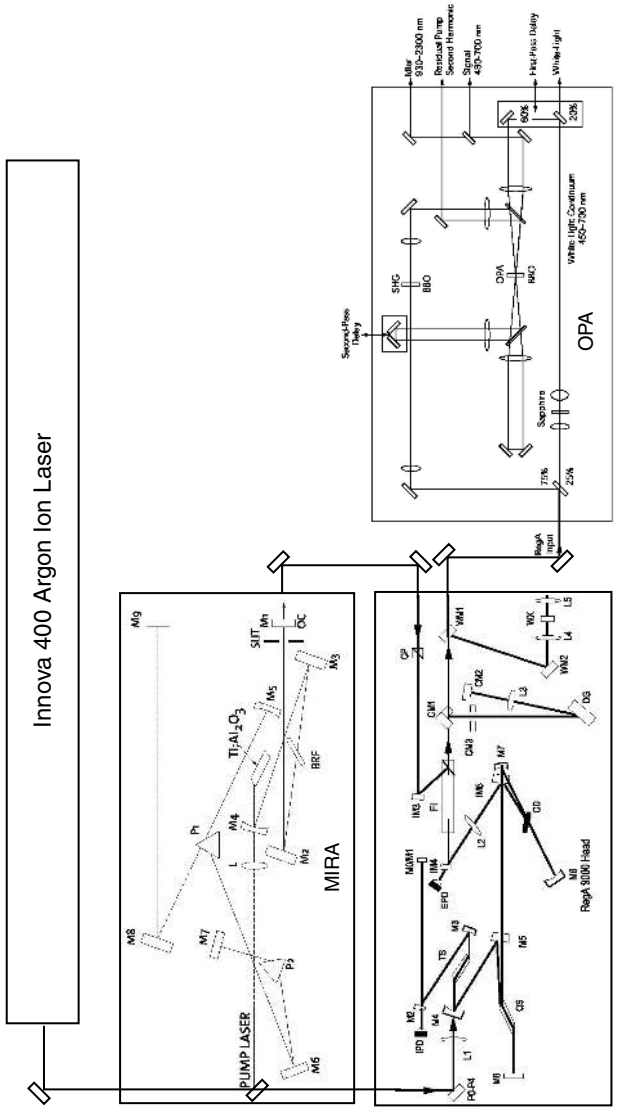

Figure 4.1: Schematic illustration of the Coherent Inc. OPA laser system. The Argon Ion laser pumps the MIRA and the RegA. The output pulses from the MIRA are amplified in the RegA. The 800 nm output pulses of the RegA are converted to 1550 nm pulses by optical parametric amplification in the OPA.

based system, the nonlinear process of optical parametric amplification is used. However, the pulse intensity from the MIRA needs to be amplified for this process. This is done by the regenerative amplifier (RegA).

The RegA is built around a Q-switched laser cavity. A Ti:Al_2O_3 crystal is pumped by ∼16 W of power from the Innova 400 and an intra cavity acousto-optic deflector (Q-switch) induces the externally controllable loss (QS in Figure 4.1). When the acousto optic cell is set to deflect, the inversion in the Ti:Al_2O_3 crystal increases (stimulated emission by the lasing mode of the cavity is prohibited). As the deflection in QS is turned off, a pulse from MIRA is simultaneously coupled into the cavity using an other acousto-optic cell, the cavity dumper (CD in Figure 4.1). The pulse will now experience a maximum gain from the Ti:Al_2O_3 crystal. The pulse travels through the cavity until the gain is depleted and is then ejected using the cavity dumper again. Following the ejection of the pulse, the Q-switch is again turned on as to prohibit lasing in the RegA cavity. When the inversion has again accumulated, a new pulse from the MIRA can be injected. The time to restore the inversion sets the limit of the repetition rate of the RegA output, which becomes 295 kHz. This means, that only every 270th MIRA pulse is injected into the RegA and amplified. The average output power from the RegA is also 1.3 W (same as for the MIRA), but now with 270 times more energy in the pulses. The injected pulse has, with the present alignment, 21 roundtrips in the cavity. The pulse broadening induced by travelling through the Ti:Al_2O_3 crystal and the Q-switch 21 times and the cavity dumper twice, results in a pulse of ≈ 10 ps intensity-FWHM. The linear chirp is compensated by a pulse-shaper before the exit of the RegA, with a resulting pulse intensity-FWHM of 150 fs. At the output of the RegA, the pulse energy is 4.4 μJ compared to 0.016 μJ at the output of the MIRA. The output of the RegA is injected into the optical parametric amplifier, the Coherent OPA.

In the OPA, 25 % of the pulse energy is split off to generate a white light continuum. The ≈ 1 μW pulse energy is focused into a sapphire crystal. The high intensity of the pulse induces a self-focusing of the mode. The temporal shape of the pulse then creates a rapidly changing index with time. The result is a high pulse chirp and therefore a very broad band spectrum around 800 nm. The spectrum extends from the ultra-violet to the infrared. The 75 % of the Rega output is used for second harmonic generation of a 400 nm pulse in a nonlinear crystal (SHG-BBO in Figure 4.1).

Finally, the white light continuum is overlapped with the 400 nm pulse in a second nonlinear crystal (OPA-BBO in Figure 4.1). Inside the nonlinear crystal, the parametric process of frequency difference generation is seeded by the white light continuum. In the photon picture, a 400 nm photon is split into a signal photon and an idler photon. The wavelength of the signal photon and the idler photon depends on the angle of the nonlinear crystal, which can be

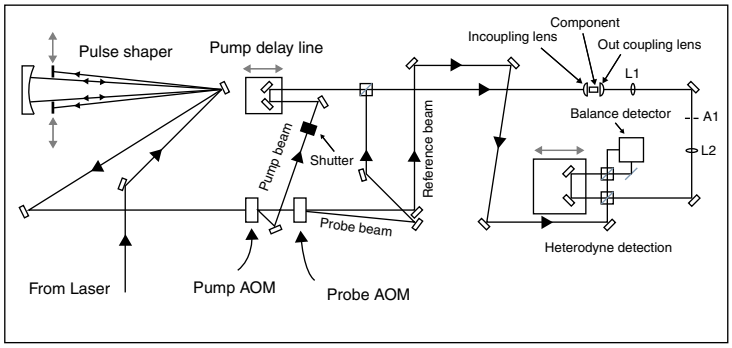

Figure 4.2: Schematic illustration of the heterodyne pump-probe set-up. See text for explanation.

adjusted to get the wavelength of interest. The nonlinear crystal is passed two times to maximize the conversion.

For the following experiments, the idler is used and adjusted for operation in the region around 1550 nm. At this wavelength, the power of the idler is $\approx$ 2 mW, giving $\approx$ 7 nJ per pulse.

4.2 The heterodyne pump-probe set-up

In this section the reader will be guided through the heterodyne pump-probe set-up, schematically shown in Figure 4.2.

Because the short pulse from the OPA travels through the strongly dispersive pump acousto-optic modulator (pump AOM in Figure 4.2), a precompensation of the broadening is done by inserting a folded grating pulse-shaper. The mirror reflecting the dispersed pulse spectrum is adjusted so that the spectrum experiences a linearly varying delay over its spectral component. Thereby the linear pulse chirp can be controlled and the dispersion of the pulse in the pump AOM can be compensated. The pulse shaper adds an extra functionality to the set-up. By inserting an aperture close to the mirror in the shaper, the spectrum of the pulse can be reduced. Accompanying the spectral narrowing is a temporal pulse broadening. The pulse width can thereby be tuned from 150 fs to 11 ps, of course at the expense of power [56].

After the pulse-shaper, the beam enters the pump AOM. The AOM consists of fused silica with a piezoelectric transducer on the one side of the crystal. A radio wave, generated by a driver, hits the silica and generates a travelling acoustic wave in the silica. This generates an index grating on which the optical wave is diffracted. Additionally, the optically diffracted field will be

Doppler shifted by the radio-frequency at which the AOM is driven (40 MHz). The power of the diffracted beam is controlled by the power of the radio wave, which is controllable from the driver.

The pump beam then goes through a shutter and a delay line with a 250 ps span. After the delay line, the pump beam is directed to the in-coupling microscope objective and the light is coupled into the component. The energy of the pump pulses at the microscope objective can be varied over 4 orders of magnitude, with a maximum energy of ∼250pJ.

The part of the beam not deflected in the pump AOM enters the probe AOM. Here the probe beam is deflected and frequency shifted by 39 MHz, 1 MHz less than the pump beam. The diffracted probe beam is overlapped with the pump beam in the 50/50 beam splitter BS1. Hereafter, the probe also hits the in coupling microscope and is coupled into the component. At that point the pump and probe pulses can not be distinguished by the direction, position, optical wavelength or polarization. However, they differ by 1 MHz in frequency.

After propagation through the component the beam is collimated using the out coupling microscope lens. Thereafter, lens L1 images the component output facet onto a small aperture A1, to strip the scattered light from the waveguide mode. The lens L2 recollimates the beam.

The part of the beam from the OPA, which has not been deflected in the pump AOM, nor in the probe AOM is used as the reference with which the probe signal will be down mixed and hereafter detected.

By controlling the pump delay line, the pump can be temporally shifted with respect to the probe. Using the shutter, the probe transmission through the component can be measured with and without the pump as function of the delay. Thereby the pump induced probe transmission change can be measured. The normalized transmission change or normalized probe transmission is defined as the ratio between the probe intensity transmission with and without the pump.

4.2.1 Detection

Figure 4.3 zooms in on the heterodyne detection scheme. The pump and probe beam, and the reference beam are overlapped in the 50/50 beam splitter. Before that, a delay line is included in the reference beam path. Thereby the reference pulse can be overlapped temporally with the probe pulse. Finally the balanced detector measures the two quadratures from the 50/50 beam splitter.

At this point, the reference beam has been overlapped with the 40 MHz frequency shifted pump beam and the 39 MHz frequency shifted probe beam. Before we look at the beating frequencies of the heterodyne signal, an additional important property of the light from the OPA has to be mentioned. Due to the 295 kHz repetition rate of the laser, the spectrum of the pulse-train will have fringes separated by 295 kHz. Therefore, the beating frequency

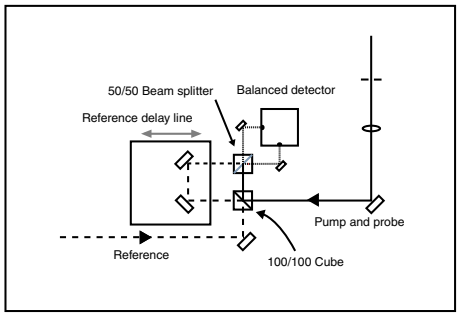

Figure 4.3: Zoom of the heterodyne detection scheme. The reference pulse delay can be adjusted such as to temporally overlap the reference and probe. The probe and reference pulses are spatially overlapped in the 50/50 beam splitter and the two quadratures are detected in the balanced detector.

spectrum of the overlapped pump, probe and reference, generated from the mixing of the 40 MHz and 39 MHz together, and with the nonshifted reference, will contain a multitude of 295 kHz separated beating frequencies. Figure 4.4 shows a schematic illustration the shifted probe and reference spectra. The 39 MHz shifting corresponds to a shift of 132 fringes (132 ·295 kHz) plus 60 kHz. Therefore the lowest beating frequency between the probe and reference will be 60 kHz, being the beating between nearest reference fringe on the right side of the probe fringe. The beating modes will then be spaced from the 60 kHz with a whole multiple of 295 kHz (shown in Figure 4.4). Beating between the nearest reference fringe to the left side of a probe fringe will be at 295 kHz-60 kHz=235 kHz, and then the following beating frequencies will be at 235 kHz + n·295 kHz, where n is a whole positive number.

The two lowest beating frequencies between the pump and reference will be at 120 kHz and 175 kHz. Beating between the pump and probe will be at 115 kHz and 180 kHz.

The 60 kHz beating intensity between the probe and reference in the one arm of the balanced detection scheme, can be written as

$$\begin{aligned} I_1 &= \frac{1}{2}P_{reference} + \frac{1}{2}P_{probe} + \\ &+ \frac{1}{2}\sqrt{P_{reference}P_{probe}}\cos\left[2\pi \cdot 60kHz \cdot t + \phi_{reference} + \phi_{probe}\right] \end{aligned} \quad (4.1)$$

where $P_{reference}$, P_{probe}, $\phi_{reference}$ and ϕ_{probe} are the reference power, probe power, optical phase of the probe and reference, respectively [57]. In the second

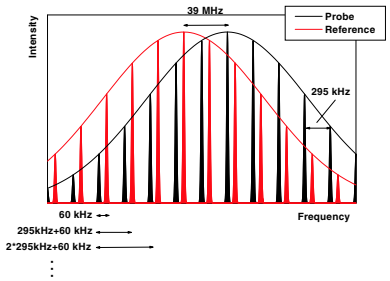

Figure 4.4: Schematic illustration of the reference and probe frequency spectra. The 39 MHz frequency shift of the probe pulse spectrum with respect to the reference pulse spectrum corresponds to 132 times 295 kHz plus 60 kHz. The lowest beating frequency is therefore 60 kHz and all other beating frequencies are spaced from the 60 kHz by at whole multiple of 295 kHz.

arm of the balanced detection, the intensity is

$$I_2 = \frac{1}{2}P_{reference} + \frac{1}{2}P_{probe} + \\ + \frac{1}{2}\sqrt{P_{reference}P_{probe}}\sin\left[2\pi \cdot 60kHz \cdot t + \phi_{reference} + \phi_{probe}\right] \quad (4.2)$$

The detectors in the two arms are balanced with respect to the reference and probe, therefore the current from the balanced detector will be

$$i(t) = \frac{2e\eta}{h\nu}\sqrt{2P_{reference}P_{probe}}\cos\left[2\pi \cdot 60kHz \cdot t + \phi_{reference} + \phi_{probe} + \pi/4\right] \quad (4.3)$$

where e is the elementary particle charge, η the detection efficiency, h Plancks constant and ν the optical carrier frequency. Since the reference beam intensity is constant, equation 4.3 states that, if the beating signal at 60 kHz is detected, any change in the current amplitude will be proportional to the change in probe amplitude. A change in the phase of the 60 kHz signal will be equal to a change in the optical phase of the probe, again because the phase of the reference is constant.

To measure the amplitude and phase of the 60 kHz heterodyne signal, the current from the balanced detector is amplified in a current pre-amplifier and subsequently the voltage output is measured in a dual phase lock-in amplifier. The 60 kHz electrical reference to the lock-in amplifier is generated by down mixing a 39 MHz reference from the probe AOM driver, with the 132th harmonic of the RegA TTL signal.

In conclusion, by selectively detecting at 60 kHz, the lock-in measures the amplitude and phase of the probe. Only the probe signal is detected, even when the pump and probe are temporally overlapped, due to the different beating frequencies between the pump and reference, and probe and reference.

Chapter 5

Electrical modulation of absorption and refractive index

The measurements presented in this chapter contribute to the investigation on using the waveguide electroabsorber as an EAM. A new technique based on the heterodyne detection scheme will be presented and used to measure the amplitude and phase transfer functions of the EAMs as function of the reverse bias and the wavelength. In chapter 3, the transmission as function of reverse bias and wavelength was investigated with respect to extinction ratio and insertion loss. The additional knowledge of the phase transfer function of the EAM, enables the calculation of the pulse chirp generated by electrically modulating the absorption. Optimum operation points with respect to the pulse extinction ratio, pulse chirp and component insertion loss can then be derived from the measurements.

The chapter is composed as follows. First, an introduction and a definition of the terms chirp and α_H-parameter will be given. Thereafter a section will focus on the specific considerations when applying the heterodyne set-up for this kind of experiment. The results will be presented and discussed with respect to optimal points for operation of the EAMs. The strongholds of this new technique will be discussed with respect to techniques reported in the literature. Finally, a simpler, but improved technique for characterizing the component chirp, still based on the heterodyne detection scheme is proposed.

5.1 Pulse chirp

5.1.1 The phase and refractive index

In general terms, the optical field after propagation through the EAM can be expressed as

$$E(t) = A(t)e^{i\phi(t)} \tag{5.1}$$

where A is the field amplitude, ϕ is the phase. The field amplitude is

$$A(t) = A_0 e^{-\alpha(t)l/2} \tag{5.2}$$

where A_0 is the field amplitude before the component, $\alpha(t)$ is the material absorption and l the component length. The time variation comes from the temporally modulated reverse bias applied to the component. All passive losses are omitted from the expression. In a frame travelling with the speed of the optical carrier frequency, the phase can expressed as

$$\phi(t) = -2\pi\nu_0 t + \tilde{\phi}(t) \tag{5.3}$$

where ν_0 is the optical carrier frequency ($\sim$293 THz for 1550 nm) and $\tilde{\phi}(t)$ is the additional phase acquired by propagation through the component. The additional phase depends on the modal refractive index of the component

$$\tilde{\phi}(t) = \frac{2\pi\nu_0 l}{c} n(t) \tag{5.4}$$

where c is the speed of light in vacuum and $n(t)$ is the modal refractive index depending, through the bias modulation, on the time. The frequency of the optical field is given by

$$\nu(t) = -\frac{1}{2\pi}\frac{d\phi(t)}{dt} = \nu_0 + \delta\tilde{\nu}(t) \tag{5.5}$$

where

$$\delta\tilde{\nu}(t) = -\frac{1}{2\pi}\frac{d\tilde{\phi}}{dt} = -\frac{2\pi\nu_0 l}{c}\frac{dn(t)}{dt} \tag{5.6}$$

is defined as the instantaneous frequency deviation from the carrier frequency [57]. A change in the refractive index with time therefore results in a modulation of the frequency. An optical pulse generated by modulating the absorption in the EAM is said to be chirped, if the instantaneous frequency varies with time, that is, $dn/dt \neq 0$.

The magnitude and the sign of the instantaneous frequency deviation are important figures together with the temporal intensity profile, when discussing

the pulse propagation in optical fibers. They determine the width of the pulse spectrum and the temporal distribution of the spectral components, which will be redistributed when propagated in the dispersive fiber. This results in either a broadening or a narrowing of the pulse, depending on the shape of the chirp and the dispersion in the fiber. If the frequency is red-shifted in the leading part of the pulse and blue-shifted in the latter part of the pulse, the pulse is so-called negatively chirped. In the opposite case the pulse is so-called positively chirped. A negatively chirped pulse will initially be temporally compressed in a fiber with anomalous dispersion, such as a standard single mode fiber at 1550 nm. Eventually, the pulse will broaden from the point where group velocity dispersion has completely compensated the initial chirp. For all propagation distances, the positively chirped pulse will broaden. Therefore, the generation of a pulse with as low positive chirp as possible or better, a negatively chirp pulse, is advantageous.

5.1.2 The α_H-parameter

The ability of a transmitter to generate pulses with low positive, or negative chirp is traditionally described by its linewidth enhancement factor, also called the α_H-parameter [16, 58]. The α_H-parameter is defined as the ratio between change in the real (χ_R) and the imaginary part (χ_I) of the susceptibility following an external perturbation

$$\alpha_H = \frac{\Delta\chi_R}{\Delta\chi_I} = \frac{4\pi\nu_0}{c}\frac{\Delta n}{\Delta\alpha} \tag{5.7}$$

The second equality comes from following the derivations in [59] (explicitly derived in Appendix A). Per definition, the α_H-parameter is a small-signal parameter and was used (introduced) by Henry in 1982 in the explanation of the spectral linewidth of semiconductor lasers due to fluctuations in the refractive index [60]. Notice, that the α_H-parameter is independent of the EAM length. Generally, an $\alpha_H \neq 0$, states that a change in the material absorption will be accompanied with a change in the refractive index. In the case of an EAM, the external perturbation providing the refractive index and absorption change is the reverse bias. If the α_H-parameter is nonzero, the pulses generated by the EAM will be chirped. For the application of the EAM as an intensity modulator, it is preferable that α_H is small or even better, negative. The smaller the magnitude, the more narrow the pulse spectrum. A negative α_H-parameter corresponds to an increase in the index for decreasing absorption. Therefore, when a pulse is generated using an intensity modulator with a negative α_H-parameter, the pulse generated will be negatively chirped. For a positive α_H-parameter the pulse chirp becomes positive (see Figure 5.1).

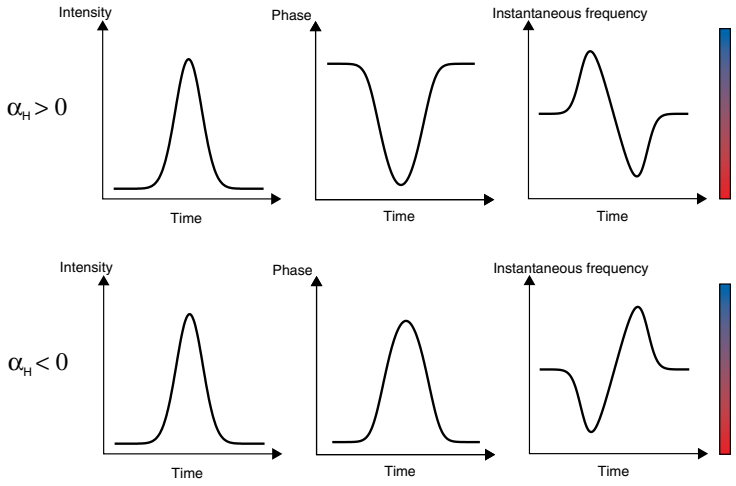

Figure 5.1: Illustration of the correspondence between the sign of the α_H-parameter, the phase and the instantaneous frequency. The chirp is positive for $\alpha_H > 0$ and negative for $\alpha_H < 0$.

The small-signal α_H-parameter, is generally dependent on the bias applied to the EAM [61]. In an effort to describe the chirp on the signal generated in a large signal regime by a single α_H-parameter, so-called effective α_H-parameters have been proposed [62, 63]. Using a single effective α_H-parameter is more convenient and can in many cases provide the customer with adequate information on the chirp generated by using the component. Another reason for the introduction of the effective α_H-parameter is the multiple measurement techniques available. Some of them are large signal techniques, however providing only a single α_H-parameter [64, 65]. The most common techniques will be presented and discussed in relation to the heterodyne technique in section 5.8. The "3 dB" α_H-parameter, α_H^{3dB}, is defined as the α_H-parameter at the bias corresponding to a 3 dB reduction of the intensity in the "on"-state [64]. The α_H^{3dB}-parameter is useful, as the main frequency chirp is typically generated at approximately this point. Another effective α_H is defined as

$$\alpha_H^{on-off} = \frac{4\pi\nu_0}{c}\frac{n_{on} - n_{off}}{\alpha_{on} - \alpha_{off}} \tag{5.8}$$

being the "on"-"off" α_H-parameter [63]. Here, n_{on} and α_{on} are the refractive index and absorption at the "on"-state of the EAM, respectively. The refractive index and absorption at the "off"-state are represented by n_{off} and α_{off}, respectively. Acknowledging the fact that the chirp experienced at the low

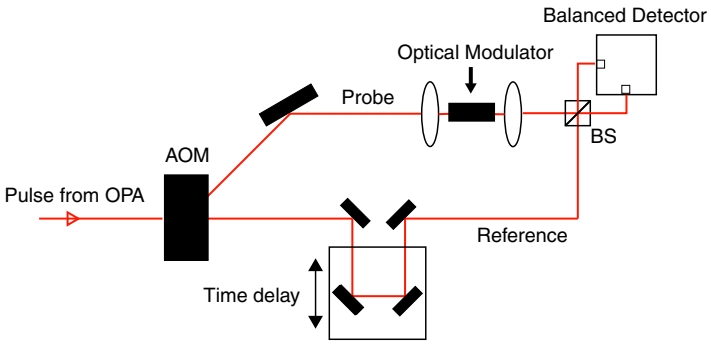

Figure 5.2: Schematic illustration of the set-up for measuring the amplitude and phase transfer function of an optical modulator as function of the bias, using heterodyne detection.

intensity part of the pulse has less importance than the chirp experienced during the strong intensity part of the pulse, Dorgeuille et al. proposed yet another effective α_H-parameter, the α_H^{on-3dB}-parameter

$$\alpha_H^{on-3dB} = \frac{4\pi\nu_0}{c}\frac{n_{on} - n_{3dB}}{\alpha_{on} - \alpha_{3dB}} \tag{5.9}$$

where n_{3dB} and α_{3dB} are the refractive index and absorption, at which the intensity is reduced 3 dB with respect to the "on"-state [61].

From the measurements reported in this chapter the full α_H-parameter dependence on the reverse bias is calculated. Hence, it is possible to evaluate if a single effective α_H-parameter can represent the chirping characteristics of the EAM.

5.2 Experimental set-up

In the previous chapter, a full description of the heterodyne pump-probe set-up was presented. For the measurement of the amplitude and phase transfer functions of the component, the pump pulses are not used. The change of the probe amplitude and phase is only due to changes in the reverse bias applied to the component. Figure 5.2 shows a schematic illustration of the essential part of the set-up. The component is inserted in the one arm of a free-space Mach-Zehnder interferometer. The light deflected and frequency shifted, enters the one arm of the interferometer and is coupled into the component. The non deflected light enters the time delay such as to temporally overlap the pulses from the two arms in the beam splitter (BS) before detection.

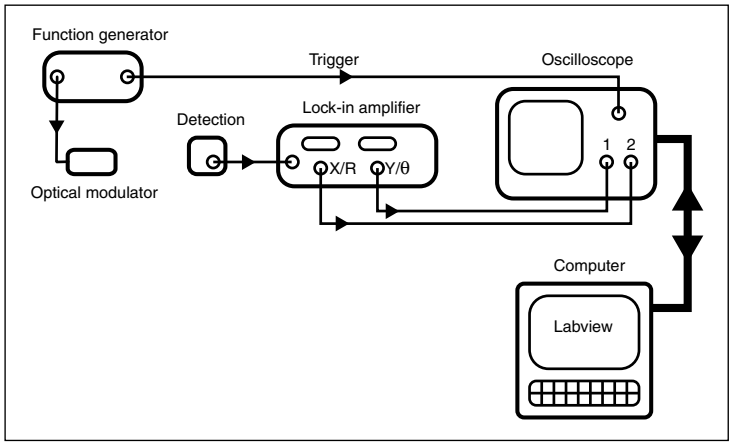

Figure 5.3: Schematic illustration of the acquisition scheme for the measurement of the amplitude and phase transfer function.

To modulate the bias applied to the EAM a function generator is used, see Figure 5.3. The voltage is swept using a saw-tooth shape with a frequency of 60 Hz. The lock-in amplifier, detecting the heterodyne signal, has analog outputs proportional to the amplitude (R) and phase (ϕ) measured. By feeding these into two separate channels in an oscilloscope, triggered by the function generator, the amplitude and phase transfer functions of the EAM can be monitored online. The coupling into and out off the component is then optimized by monitoring both the detected signal magnitude and extinction ratio as function of the reverse bias. The time constant on the lock-in was chosen in the order of a few hundred μs, to ensure an acceptable sampling rate.

Instead of storing the analog signals proportional to the amplitude and the phase on the computer, it is advantageous to store the analog signals proportional to the in-phase (X) and out-of-phase (Y) quadratures. From the X and Y, the phase change can be calculated directly without knowing the conversion factor between the analog signal proportional to the phase and the phase itself.

The relation between the amplitude (A) and phase (ϕ) and the measured X and Y is

$$A = \sqrt{X^2 + Y^2}, \quad \phi = arctan(X/Y) \tag{5.10}$$

The dynamical range of the 8-bit analog to digital converter in the oscilloscope corresponds to a maximum measurable extinction ratio of 24 dB ($10\log(2^8)$). However, since the amplitude, and not the intensity transmission is measured, an actual intensity transmission change of 48 dB is measurable

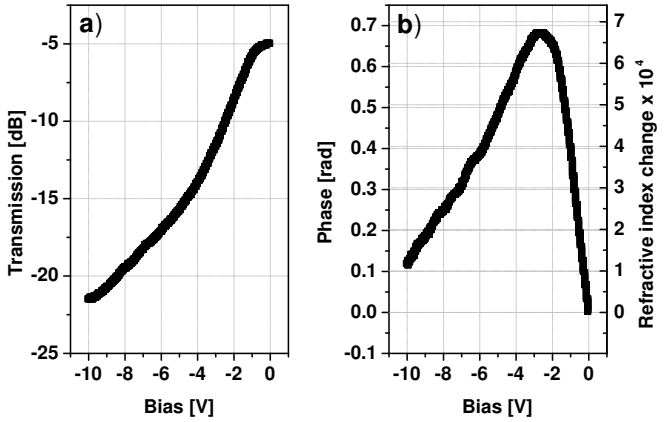

Figure 5.4: a) The measured component intensity transfer curve, b) The measured phase transfer curve, showing an increase in the phase for increasing reverse bias until -2.7 V. Hereafter the phase decreases again. From the phase measurement the index change is calculated and shown as the second axis in the plot.

within one sensitivity scale. The dynamical range of the 16-bit analog-to-digital converter of the lock-in-amplifier is 48 dB which corresponds to a maximally measurable intensity variation using one sensitivity scale of 96 dB. The acquisition of the data is done, using a Labview program on a computer connected to the oscilloscope via a standard GPIB bus.

5.3 Measurement at 1550 nm

In Figure 5.4 is seen the measured transfer function for the component transmission and the phase as function of the reverse bias. The heterodyne detection is not calibrated to give the absolute transmission through the component, only the relative change is measured. The component is the same high barrier EAM on which absorption spectra in chapter 3 were measured. The insertion loss at 0 V is found from the absolute transmission measurements presented in Chapter 3. The center wavelength of the probe pulse was 1550 nm. The probe pulse was shaped in the pulseshaper and had a 1 ps intensity-FWHM. In Figure 5.5 both the measured second harmonic autocorrelation trace of the pulse and the measured spectrum are shown. The narrow spectrum is advantageous because of the increased spectral resolution of the experiment. The probe pulse energy

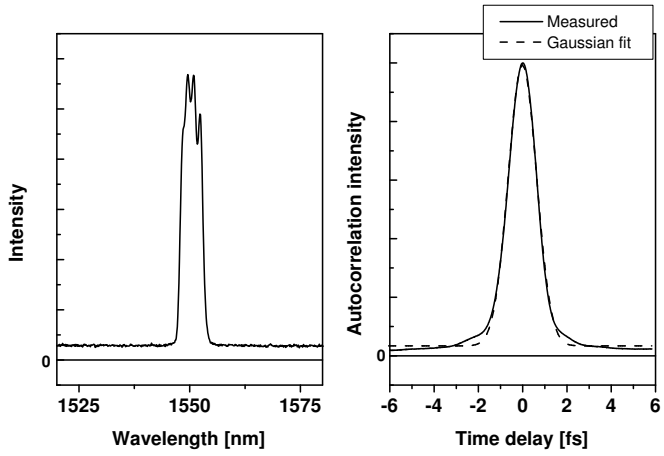

Figure 5.5: Measured probe pulse spectrum (left graph) and pulse autocorrelation (right graph). The spectral width is 5 nm and the pulse intensity FWHM is 1 ps and is well fitted with a Gaussian pulse shape.

was set to 0.3 pJ, which was low enough not to bleach the absorption. The accumulation or averaging time for the measurement was approximately 10 seconds.

As expected, from the measurement presented in Chapter 3, the absorption is increased with the reverse bias. The extinction ratio is more than 20 dB for a 10 V swing. This is more than measured in chapter 3 and probably due to a lower amount of scattered light. The measured phase transfer function in Figure 5.4 b) shows the strength of this technique. The measurement technique provides a high resolution and high sensitivity measurement of the phase change of the probe, induced by changing the reverse bias. In Figure 5.4 b) it is observed, that the phase increases with increasing reverse bias until -2.7 V, from where the phase decreases again. The maximum phase change is 0.7 rad or 40 deg. Knowing the length of the component, the modal refractive index change is calculated, using equation (5.4) on page 42, and is shown on the second axis in Figure 5.4 b) . The maximum refractive index change, observed at -2.7 V is $6.7 \cdot 10^{-4}$.

A simplified picture can be used to understand the behavior of the refractive index as a function of the reverse bias. The absorption spectrum is described, as shown in Figure 5.6, as being zero below the absorption edge and a constant above [66]. The schematic refractive index spectrum is also shown in Figure

5.6. For an increasing reverse bias, the absorption edge is red-shifted and so is the refractive index spectrum. If the wavelength of the probe is on the low energy side of the refractive index resonance, a red-shift of the absorption edge initially increases the refractive index and thereby the phase of the light at the output of the component. This region is indicated by an "a" in Figure 5.6. If the bias is increased further, the refractive index will reach the peak of the resonance and afterwards decrease again, indicated as "b". This explains the initial increase and following decrease in the phase with increased reverse bias. A similar presentation of the refractive index dynamics is also given by Dorgeuille et al. [61]. Asymmetry of the refractive index change around -2.7 V can not be explained by the simple "box"-model. The explanation is likely to include the fact that the refractive index resonance is broadened as the reverse bias is increased. This is because the absorption edge becomes less abrupt with increasing reverse bias. To discuss the magnitude and shape of the phase change in more details the actual absorption spectrum as function of bias has to be known. Section 5.7 reports on the application of the calculated absorption spectra to calculate the refractive index change.

From the index curve, two distinct regimes of operation of the component can be found. Operation of the component between -2.7 V and 0 V will give a positive chirp and operation below -2.7 V will give a negative chirp. It can be concluded that the α_H-parameter is not constant with bias. The α_H-parameter is calculated from the measured data using

$$\alpha_H(V) = -\frac{2d\phi/dV}{d(\ln(I))/dV} \tag{5.11}$$

where I is the intensity at the output of the component. Note, that only the transmission change in necessary for the calculation and not the absolute intensity, see also Appendix A. Taking the derivative of the measured data can not be done directly because of the noise. Therefore a smoothing of both the measured and derived data is necessary. The approximately 1000 measurement points per curve ensures a good smoothing of the data. Figure 5.7 shows the α_H-parameter.

The α_H-parameter is positive above -2.7 V and negative below. From $\sim$1 V to 0 V reverse bias the α_H-parameter increases drastically going from 1.6 to 10. Since the phase transfer function is approximately linear in this regime, the reason for the important increase in the α_H-parameter is the reduced absorption dependence on the bias close to 0 V. Below -4 V of bias the α_H-parameter is approximately constant with an average value of -1.

Reported α_H-parameters measured on EAMs show a great variation. The α_H-parameter depends on the material system [6], the polarization [6], the wavelength [61], the bias [67] and strain [68]. It is therefore very difficult to make a comparative analysis between our results and results from the literature.

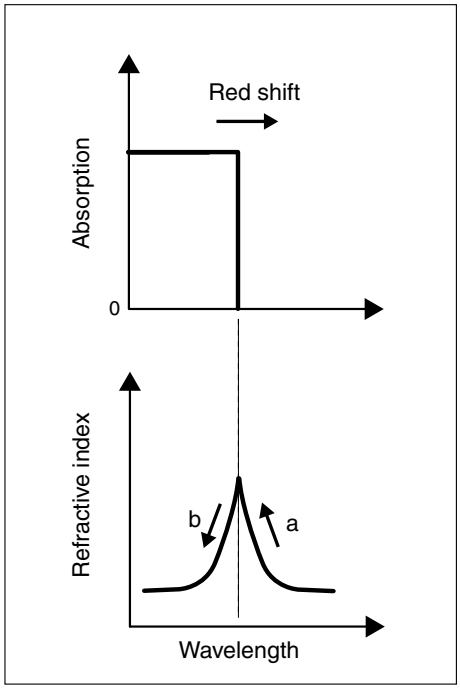

Figure 5.6: Schematic illustration of the physics behind the measured refractive index change. If the operation wavelength is below the absorption edge, an increase in the reverse bias will initially increase the refractive index, indicated by the "a"-arrow. If the reverse bias is increased further, the edge can red-shift enough to enter the "b"-region where the refractive index decreases again. The illustration is inspired by Figure 1 in [66].

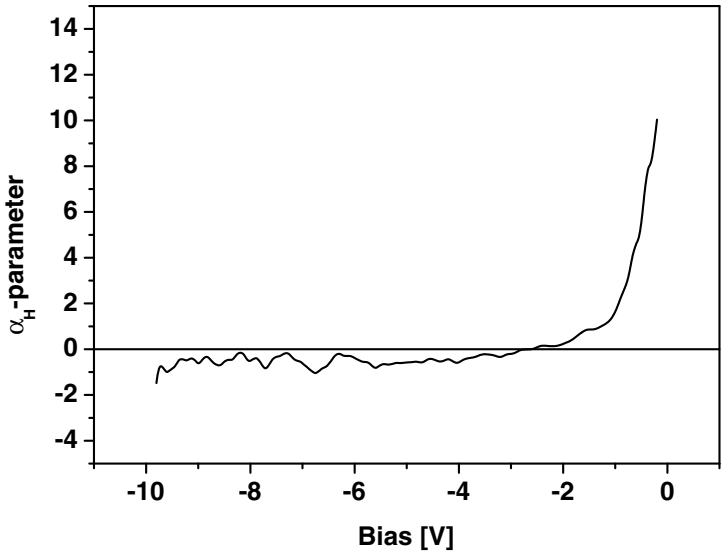

Figure 5.7: The α_H-parameter calculated using equation (5.11) with the measured transmission and phase transfer functions shown in Figure 5.4 as input.

However, in general the α_H-parameter lies between -3 to 3. Devaux et al. report on a bias dependent α_H-parameter ranging from 3 at 0 V to -2.2 at 1.5 V reverse bias, measured by the fiber-response technique [69]. The component is a 13 period, 12 nm-thick InGaAsP/6-nm-thick InGaAsP MQW waveguide electroabsorption modulator. The wavelength of operation was 1540 nm. The change in absorption accompanying the 1.5 V increase in bias was $\sim$25 dB for a 100 μm long component, somewhat higher than for our components. The form of α_H-parameter curve as function of reverse bias is qualitatively the same as reported here, being positive for low reverse biases while crossing zero and going negative for increased reversed biases. The material absorption at which the α_H-parameter crosses zero is 10 dB/100-μm, whereas only 4 dB/100-μm for the component reported on here.

Operation of the component, investigated here, with the "on"-state at 0 V is not advantageous for two reasons. First, the absorption change between 1 and 0 V reverse bias is only 0.8 dB while the highest slope is 2.9 dB/V at -2 V. Therefore, from the point of view of reduction of the drive voltage, operation below 1 V of reverse bias is advantageous. Secondly, the large and positive α_H-parameter close to 0 V will add significantly to the pulse chirp. The α_H-parameter is less than 1.6 below 1 V of reverse bias and therefore operation of the component below 1 V is also advantageous chirp-wise. However, operation

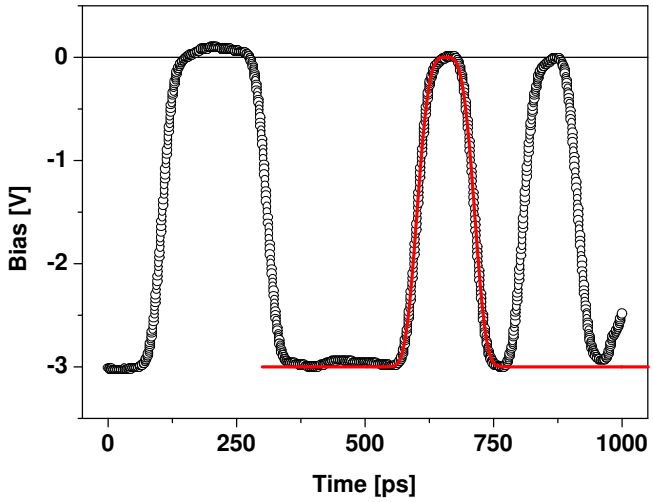

Figure 5.8: Measured electrical 10 Gb/s bit signal with a 3 V_{pp} swing and an offset bias of -1.5 V (circles). A super Gaussian fit of the 010 pattern is also shown (full line). The fit is used in the following calculations of the chirp and intensity waveform of a signal generated by modulating the bias of the EAM.

of the component at increased reverse bias also adds an unwanted increase in the insertion loss.

5.4 Calculation of the chirp

When the full amplitude and phase transfer function is measured, it can be used to calculate the response of the component to a fast modulation of the reverse bias. The calculated intensity waveforms and chirp give a simple and intuitive description of the optimum operation conditions.

The chirp on the optical signal generated by electrically modulating the EAM depends on the waveform of the electrical signal. This is because the rise and fall times of the modulation influence the speed at which the refractive index is changed with time and therefore the chirp. To get the right waveform for the calculation, a 10 Gb/s NRZ, 3 V_{pp} electrical signal from a test-set is measured. The pattern is shown in Figure 5.8. The bit pattern represents the bit series of 011001010. Only the bit pattern 010 is of interest, since the rise

and fall times are the same for all bits. To simplify the calculations, a super Gaussian fit of the 010 pattern was used instead of the measured data, see Figure 5.8. The fitted super Gaussian function is defined as

$$V(t) = A\exp[(-t^2/\tau^2)^c] - A_0 \tag{5.12}$$

where A=3 V, τ=70 ps, c=1.8 and A_0=3.

The transfer curves presented in Figure 5.4 represent the static response of the component to an applied reverse bias. To be able to use these transfer curves when calculating the response of the component to a bias modulation with a 10 Gbit/s NRZ signal, the modulation bandwidth of the component has to be larger than 5 GHz. If the bandwidth is strongly decreased with frequency, due to for example carrier pileup, the extrapolation from the static to the dynamic regime is not possible. Figure 5.9 shows the small-signal optical response of a packaged EAM, similar to the one investigated here, as function of the electrical modulation frequency. At –0.5 V the 3 dB bandwidth is approximately 26 GHz while for –2 V and up to –4 V the 3 dB bandwidth is approximately constant with a value of 33 GHz. The fact that the bandwidth initially increases with reverse bias states that the component might be limited by carrier sweep-out at low biases, where the escape time from the quantum wells is long. The constant bandwidth at higher reverse bias indicates that, either the carrier sweep out time is constant or that the optical response of the component speed is limited otherwise. The 3 dB bandwidth, beyond 30 GHz for a reverse bias above 2 V is well above the 5 GHz necessary to use the static measurements to calculate the 10 Gb/s response of the component.

The intensity transmission response is calculated from the fitted time dependent bias, $V(t)$, and the measured bias dependent transmission in dB, $T(V)$

$$I(t) = I_0 10^{[T(V(t))/10]} \tag{5.13}$$

where the I_0 is the intensity at the input of the component. The instantaneous frequency deviation, $\delta\tilde{\nu}(t)$, is calculated from the fitted time dependent bias, $V(t)$, and the measured bias dependent phase, $\phi(V)$

$$\delta\tilde{\nu}(t) = -\frac{1}{2\pi}\frac{d\phi(V(t))}{dt} \tag{5.14}$$

In Figure 5.10 the response of the device is shown for three different bias offsets. The peak-peak bias swing is 3 V and the bias offsets are -1.5 V, -2.5 V and -4.5 V. Modulation with a 3 V_{pp} and a -1.5 V bias offset gives -3 V as the "off"-state and 0 V as the "on"-state.

If the attention is initially set on the pulse shape, it is observed that the width of the pulse depends on the bias offset. At -1.5 V of bias offset, the intensity-FWHM is 122 ps compared to 98 ps and 108 ps at -2.5 V and -4.5

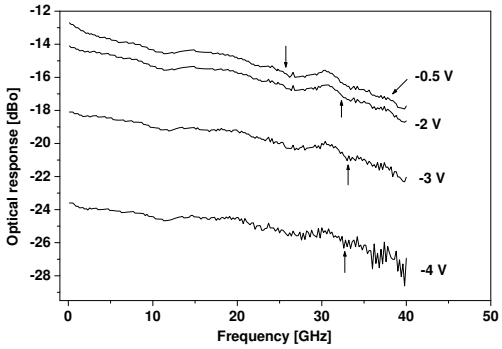

Figure 5.9: Measured small-signal response of a packaged EAM. The arrows indicate the point at which the optical response is reduced by 3 dB. Data kindly provided by L. Oxenløwe (SCOOP/COM).

V, respectively. The FWHM of the electrical signal is 112 ps. It is of course advantageous to have pulses generated with as narrow widths as possible with the applied modulation signal, since the following dispersion in the fiber will add to the pulse width, which will eventually broaden into the neighboring bit slots. As function of the applied offset bias the extinction ratio of the pulses also varies. The extinction ratio of the pulses are 6.5 dB, 8.2 dB and 5.5 dB for the offset bias of -1.5 V, -2.5 V and -4.5 V, respectively. The specification the extinction ratio to be higher than 7 dB, mentioned in Chapter 3, states that for the three cases shown in Figure 5.10, only the -2.5 V offset bias is acceptable. Both the low pulse width and the high extinction ratio are explained by the high slope of the transmission as function of bias in this bias region. Operation with the "on"-state bias below 0 V adds to the insertion loss of the component. The increased absorption loss of 0.8 dB should be acceptable compared to the above mentioned advantages gained by operating the component at -2.5 V compared to -1.5 V of offset bias.

By exclusively looking at the pulse chirp in Figure 5.10, the optimal operation point of the component would be at -4.5 V of offset bias. At this point the pulse is negatively chirped. The anomalous dispersion in a standard single mode fiber will initially compress the pulse. The maximum instantaneous frequency deviation in the leading edge is $\sim$1 GHz and ~ -1 GHz in the trailing edge. The symmetry of the electrical modulation around zero time results in an equally sized, but oppositely signed instantaneous frequency deviation in the leading and trailing edge. The maximum instantaneous frequency deviation is

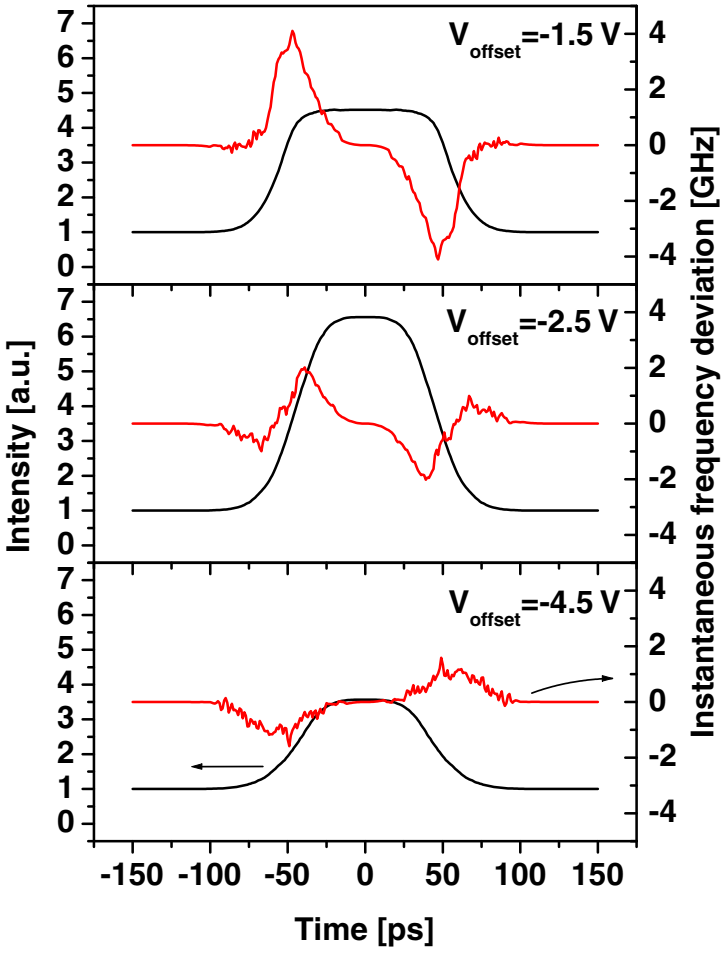

Figure 5.10: The calculated response of the high barrier EAM to a 10 Gb/s NRZ modulation. The amplitude of the electrical modulation is 3 V_{pp}. Depending on the offset bias, the chirp and waveform changes. The highest pulse extinction ratio and the narrowest pulse are observed with an offset bias of -2.5 V. The best pulse chirp, being negative, is observed for an offset bias of -4.5 V.

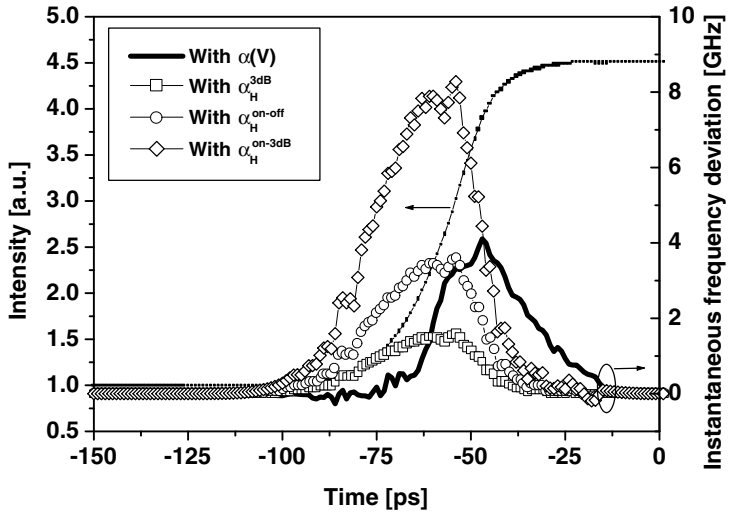

Figure 5.11: Comparison between the calculated chirp from α_H^{3dB}=0.42, α_H^{on-off} = 0.96, α_H^{on-3dB} = 2.2 and the measured $\alpha_H(V)$. The bias swing is 3 V_{pp} and the bias offset is -1.5 V. It is clearly observed that none of the effective α_H-parameters parameterize the chirp well.

therefore adequately described by a single value, namely ∼1 GHz.

Operation at -2.5 V of bias offset with a bias swing of 3 V results in an α_H-parameter varying from negative to positive. This is observed as an initial red-shift of the frequency of 0.7 GHz followed by a blue-shift of 2 GHz in the leading edge of the pulse. The blue-shift of the leading edge and the following red-shift of the trailing edge will broaden the pulse in a fiber standard single mode fiber, therefore operation at -4.5 V of offset bias is advantageous, chirp-wise, compared to operating at -2.5.

At -1.5 V of offset bias the α_H-parameter is mainly positive. The large α_H-parameters, accompanying an operation close to 0 V results in a positively chirped pulse with a maximum instantaneous frequency deviation of ∼4 GHz.

The curves presented in Figure 5.10 clearly shows the importance of being able to characterize the full amplitude and phase transfer functions. To describe the component by one single effective α_H-parameter seems difficult. Even in the case where it is possible, it is still necessary to know either the phase transfer function or the transmission transfer function to understand, if the signal degradation after a fiber transmission is due to an initially broad pulse, low pulse extinction ratio, pulse chirp or all of the above mentioned. The chirp of the pulse generated with -2.5 V of offset bias can not be described by a

single effective α_H-parameter, since it has to be both positive and negative at the same time, and $\alpha_H = 0$ will not describe the chirp well either. At -4.5 V of bias offset, the α_H-parameter is not varying much and could, to a certain extent be represented by a constant α_H-parameter. Especially interesting is the operation at -1.5 V of offset bias. During the voltage swing the α_H-parameter varies from -0.2 to 10, as described in the previous section. Figure 5.11 shows the calculated chirp generated for the different effective α_H-parameters defined in section 5.1.2.

There are no effective α_H-parameters representing the actual chirp well. The α_H^{3dB}-parameter is equal to 0.42. Using that as the effective α_H-parameter underestimates the instantaneous frequency deviation. The α_H^{on-off}-parameter is equal to 0.96 and fits quite well the size of the actual instantaneous frequency deviation. The α_H^{on-3dB}-parameter is equal to 2.2 and strongly overestimates the real instantaneous frequency deviation. In all cases the shape of the instantaneous frequency deviation can not be represented by the effective α_H-parameters. It can be concluded that one has to be very cautious when describing the chirping properties of this component by a single effective α_H-parameter. This applies to EAMs in general because of their strongly bias dependent α_H-parameter.

5.5 Measurements at different wavelengths

The α_H-parameter depends both on the bias and the wavelength [69]. Figure 5.12 shows the dependence of the insertion loss and phase transfer functions for three wavelengths, namely 1535 nm, 1550 nm and 1580 nm. At first it is observed, as expected from the discussion in Chapter 3, that the steepest insertion loss slope is found at the lowest wavelength (1535 nm). Operation at this wavelength is therefore advantageous with respect to a reduction of the drive voltage and the pulse width. However, operation with for example 1 V as the "on"-state, advantageous for operation of the component at 1550 nm, will give an insertion loss of 8 dB at 1535 dB compared to 6 dB and 5.1 dB at 1550 nm and 1580 nm, respectively.

From the measured phase transfer function it is observed, that the bias at which the maximum phase change is attained, depends on the wavelength. The bias points are -1.9 V, -2.6 V and -3.6 V for 1535 nm, 1550 nm and 1580 nm, respectively. The increase of the reverse bias to attain the maximum phase change is explained by the increased red-shift of the band edge necessary to move the refractive index peak (as function of the wavelength) past the probe wavelength, see Figure 5.6. This will inevitably increase the bias offset necessary to reduce the positive chirp. The maximum refractive index change attainable is increased with the wavelength. This is propably because the refractive index is lowered as the wavelength is moved away from the absorption

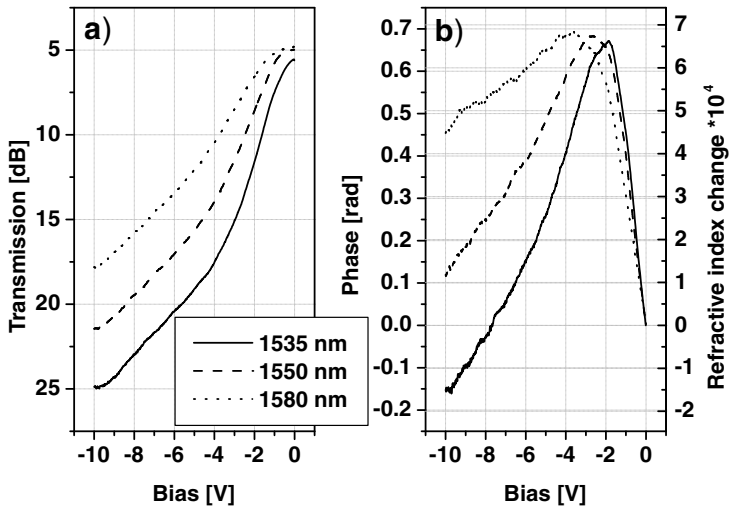

Figure 5.12: a) The measured component transmission and b) phase transfer functions for the three wavelengths 1535 nm, 1550 nm and 1580 nm. The component has the high barrier epitaxial structure. See text for discussion.

edge (see Figure 5.6). A higher increase in the refractive index is then possible when the reverse bias is increased. However, the broadening of the refractive index resonance with reverse bias also comes into play. It is therefore difficult to give a intuitive explanation of the observed refractive index change with reverse bias. However, it will be shown later in this chapter, the refractive index change calculated from the calculated absorption spectra can reproduce the trends observed experimentally.

In Figure 5.13 the calculated α_H-parameters from the measured data for the three wavelengths are shown. Because of the low dependence of the transmission with the reverse bias ($dT/dV \sim 0$), the α_H-parameter for the wavelength of 1580 nm is not well defined between -0.5 V and 0 V. The α_H-parameter at 1535 nm is lower than for 1550 nm and 1580 nm in the 0 to -4 V region and is thereby proclaiming an improved performance of the component at this wavelength. Actually the slope of the phase change is steeper in the positive α_H-parameter region at 1535 nm than at 1550 nm and 1580 nm. However, the increased slope of the insertion loss in this region ensures a lower α_H-parameter. The noise on the α_H-parameter inhibits an exact determination of the value above 4 V of reverse bias. However, the α_H-parameters lie all between approximately 0 and -2.

The results are, trend-wise, in agreement with the α_H-parameters measured

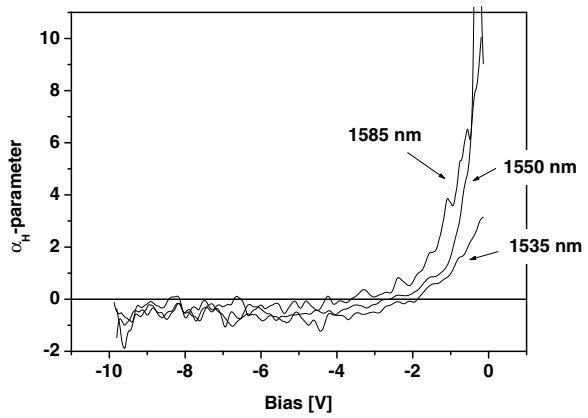

Figure 5.13: The α_H-parameter calculated from the measurements for the wavelengths 1535 nm, 1550 nm and 1580 nm. As expected, the shorter the wavelength the lower the α_H-parameter, as observed below 4 V of reverse bias. Above 4 V of reverse bias a precise determination of the α_H-parameter is difficult due to the noise.

by Dorgeuille et al. in an InGaAsP MQW EAM [61]. The α_H-parameter is reported to increase at zero bias with increasing wavelength, and the reverse bias point at which the α_H-parameter changes sign increases with the wavelength.

As in the previous section, the intensity waveform and the chirp can be directly calculated from the measured transfer functions. Figure 5.14 shows the intensity waveform and chirp for the wavelengths 1535 nm, 1550 nm and 1580 nm. The electrical signal is the 10 Gb/s NRZ signal used previously. The bias offset is -2.5 V. The bias offset for the calculation is chosen because it produced the best pulse, intensity-wise, at 1550 nm. The maximum positive instantaneous frequency deviation generated at the leading edge is in all three cases equal to $\sim$2 GHz. The maximum negative instantaneous frequency deviation generated at the leading edge is 1.8 GHz, 1 GHz and 0.2 GHz at 1535 nm, 1550 nm and 1580 nm, respectively. The negative chirp will initially compress the pulse, and since the positive chirp is the same in all three cases, the optimum operation wavelength, chirp-wise, is 1535 nm. The intensity waveform of the signal is also best at 1535 nm, explained by the steep insertion loss transfer curve. The extinction ratio at 1535 nm is 10 dB, while 8.2 dB and only 5.3 dB at 1550 nm and 1580 nm, respectively. It can therefore be concluded from the measurements that, operation of this component close to the absorption edge is advantageous, not only with respect to the extinction ratio, but also the chirp. The penalty is however an increased insertion loss of 2 dB going from 1550 nm to 1535 nm.

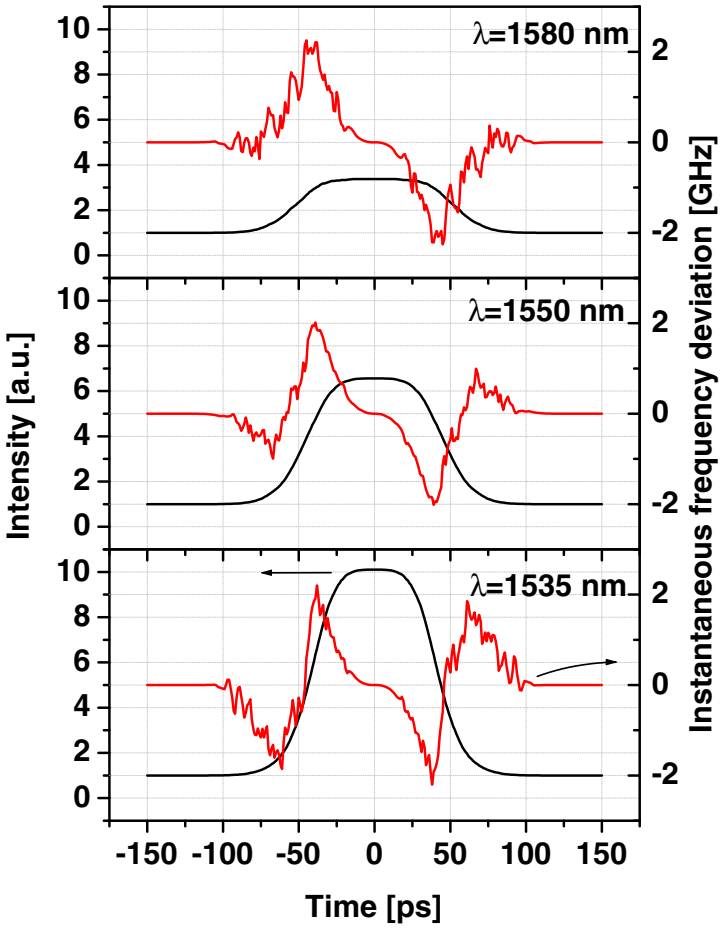

Figure 5.14: The calculated response of the high barrier EAM to a 10 Gb/s NRZ modulation. The calculation is based on the measured transmission and phase transfer curves. The amplitude of the electrical modulation is 3 V_{pp} and the offset bias is -2.5 V. Depending on the wavelength, the chirp and waveform changes. Of the three wavelengths, the highest pulse extinction ratio is found at 1535 nm. See the text for the discussion of the chirp.

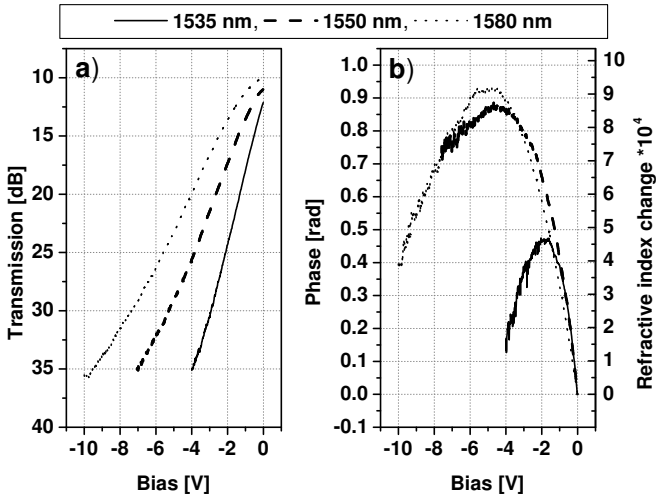

Figure 5.15: a) The measured component transmission and b) phase transfer functions for the three wavelengths 1535 nm, 1550 nm and 1580 nm. The component has the low barrier epitaxial structure. See text for discussion.

5.6 Comparison between the low barrier and high barrier components

Until now, the intensity and phase transfer function have been measured as function of the bias and the wavelength on a high barrier component. In this section the measurement on a low barrier component will be compared to the measurement presented on the high barrier component. The comparison will not only be between the bias dependent absorption as in Chapter 3, but now also between the refractive index change and the α_H-parameter. The component with low barriers is the same on which the measurements in Chapter 3 were performed.

Figure 5.15 shows the transmission and phase transfer curves for the low barrier component, at 1535 nm, 1550 nm and 1580 nm. When Figure 5.12 a) and Figure 5.15 a) is compared it can be concluded that the slopes of the transmission transfer function are steeper for the low barrier component than for the high barrier component. For example, a 10 dB of extinction ratio at 1535 nm can be generated by 1.6 V bias swing for the low barrier component ("on"-state at 0 V bias, optimum for this component), while 2.8 V is necessary for the

high barrier component ("on"-state at -1 V bias, optimum for this component). However, the insertion loss is higher for the low barrier component than for the high barrier component. The insertion loss is for example 12.1 dB at 1535 nm, when operating the low barrier component with the "on"-state at 0 V. This should be compared to 7.5 dB when operating the high barrier component with the "on"-state at -1 V. The component with low barriers is over all better than the high barrier component, with respect to the extinction ratio for a given drive voltage. The high barrier component is preferable compared to low barrier component, when considering the insertion loss. In chapter 3 the passive insertion loss of high barrier component was found to be 4.8 dB while 10.5 dB for the low barrier component. Therefore the insertion loss difference between the low barrier and the high barrier components is mainly due to the waveguide quality and not to the active material. An improved processing of the low barrier component should be able to reduce the passive losses down to the 4.8 dB measured for the high barrier component. At 1535 nm the insertion loss would then be 6.6 dB. For an anti-reflection coated component the insertion loss would be reduced to 3.6 dB. This shows, that the low barrier component can potentially also be better than the high barrier component with respect to the insertion loss.

In Figure 5.15 b) the phase transfer functions of the low barrier component is shown together with the refractive index change. As for the high barrier component, an initial increased in the phase with increased reverse bias is observed and followed by a decrease. The bias point at which the phase begins to decrease again also increases with wavelength.

Figure 5.16 shows the α_H-parameter for the component with low barriers. The α_H-parameter is generally smaller than for the high barrier component. The reduced α_H-parameter at 0 V is primarily caused by the steeper insertion loss slope. The lower α_H-parameter states that the low barrier component is preferable chirp-wise.

Compared to the absorption spectra measurements presented in Chapter 3, the measurements presented in this chapter show that properties of the high and low barrier components differ quite a lot. The steeper transfer curve for the low barrier component compared to the high barrier component, could agree with the larger red-shift per unit field, expected for the low barrier component. Why this is not observed from the absorption spectra measurements presented in the previous chapter is not understood.

From calculation examples of the chirp and intensity waveform it is difficult to give a general picture of the optimal operation points of the two components. The points to include in such a discussion are the insertion loss, the drive voltage, the bias offset, the wavelength and the optical system in which the signal is transmitted. Therefore, an analysis of the performances of the components with respect to optimum operation conditions should be done with a simulation

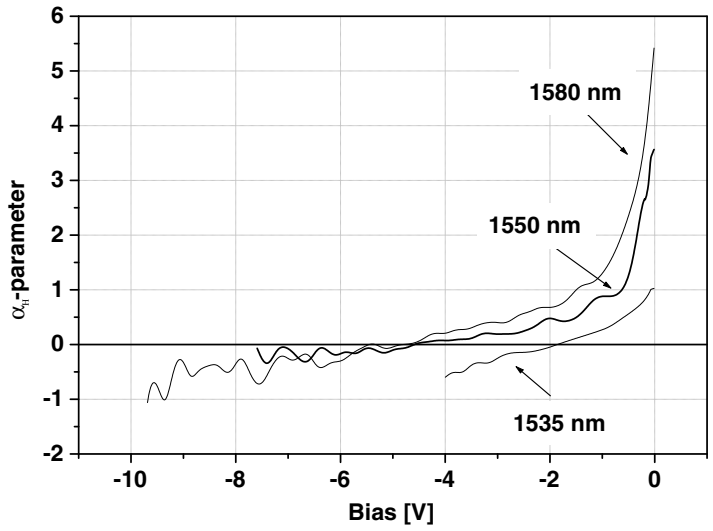

Figure 5.16: The α_H-parameter calculated from the measurements for the wavelengths 1535 nm, 1550 nm and 1580 nm. See text for discussion.

of the component in a full transmission system.

5.7 Calculation of the refractive index change for the low barrier component

In Chapter 3 it was shown, that the calculated absorption spectra fitted the measured spectra quite well for the low barrier component. It is therefore interesting to investigate if the refractive index change, calculated from the spectra, also shows the dynamics described in the previous sections. Figure 5.17 shows the calculated absorption changes in the 1500 to 1600 nm range together with calculated refractive index changes. The refractive index change is calculated by making a Kramers-Kroenig transformation of the absorption change spectra,

$$\Delta n(\omega) = \frac{c}{\pi}\ PV \int_0^\infty \frac{\Delta\alpha(\overline{\omega})}{\overline{\omega}^2 - \omega^2} d\overline{\omega} \tag{5.15}$$

where PV means that the principal value of the integral is taken [5]. Both calculated and measured absorption spectra have been used to calculate the refractive index change in EAMs [68, 70, 71, 72]. However, it is questionable

how wide an absorption change spectrum is needed in order to calculate the refractive index change at a specific wavelength. The weight function $1/(\overline{\omega}^2 - \omega^2)$ reduces the contribution of the absorption change at frequencies away from ω to the refractive index change at ω. This, together with the fact that the absorption change for energy states high in the band is limited, enables a truncation of the integration.

The refractive index change is calculated from the wavelength dependent absorption, using the Kramers-Kroenig transformation as function of wavelength

$$\Delta n(\lambda) = \frac{\lambda^2}{2\pi^2}\left(\int_{\lambda_1}^{\lambda-\delta\lambda}\frac{\Delta\alpha(\overline{\lambda})}{\overline{\lambda}^2-\lambda^2}d\overline{\lambda} + \int_{\lambda+\delta\lambda}^{\lambda_2}\frac{\Delta\alpha(\overline{\lambda})}{\overline{\lambda}^2-\lambda^2}d\overline{\lambda}\right) \tag{5.16}$$

where λ_1 and λ_2 are the start wavelength and end wavelength of the spectrum, respectively. The spectra presented in Chapter 3 have λ_1=1200 nm and λ_2=2210 nm. The singularity point at $\overline{\lambda} = \lambda$ is omitted from the integration by splitting the integration into two integrals, one from λ_1 to $\lambda - \delta\lambda$ and one from $\lambda + \delta\lambda$ to λ_2, where $\delta\lambda$ is chosen to be 10^{-5} nm. A further decrease in the size of the $\delta\lambda$ does not change the value of the integration, because the absorption change within $2\delta\lambda$ is small. However, a small decrease of 250 nm of the 1010 nm wide absorption spectrum does influence the calculated refractive index change in the 1500–1600 nm range. The effect is a reduction of the overall refractive index change of $3 \cdot 10^{-4}$. This is a non-negligible change of the refractive index and does question the refractive index change measurements reported in the literature based on the Kramers-Kroenig transformation of even narrower absorption spectra [71]. However, the same trends observed experimentally can be reproduced via the calculated absorption spectra.

Figure 5.17 shows that the refractive index change, for a given bias, depends on the wavelength. It is observed that below 1525 nm, the refractive index is decreased with increasing reverse bias. Operation of the EAM below 1525 nm is therefore advantageous chirp-wise, since the α_H-parameter is negative for all reverse biases. Above 1575 nm the refractive index changes are all positive and increase with the bias, giving a positive α_H-parameter for all reverse biases. In the intermediate region, between 1525 nm and 1575 nm, the maximum index change is found at 4 V of reverse bias, at which point the α_H-parameter will go from positive to negative. The experimental data showed that operation at a short wavelength (1535 nm) was advantageous, both extinction ratio and chirp-wise. The optimal operation wavelength of the component is according to the calculations at 1510 nm. At this wavelength there is a maximal extinction ratio per volt and the refractive index change with reverse bias is negative. This observation is important for the EAM, stating that the shape of the absorption change spectra ensures that the wavelength at which the extinction ratio per volt is the highest, is also a wavelength where the α_H-parameter is negative.

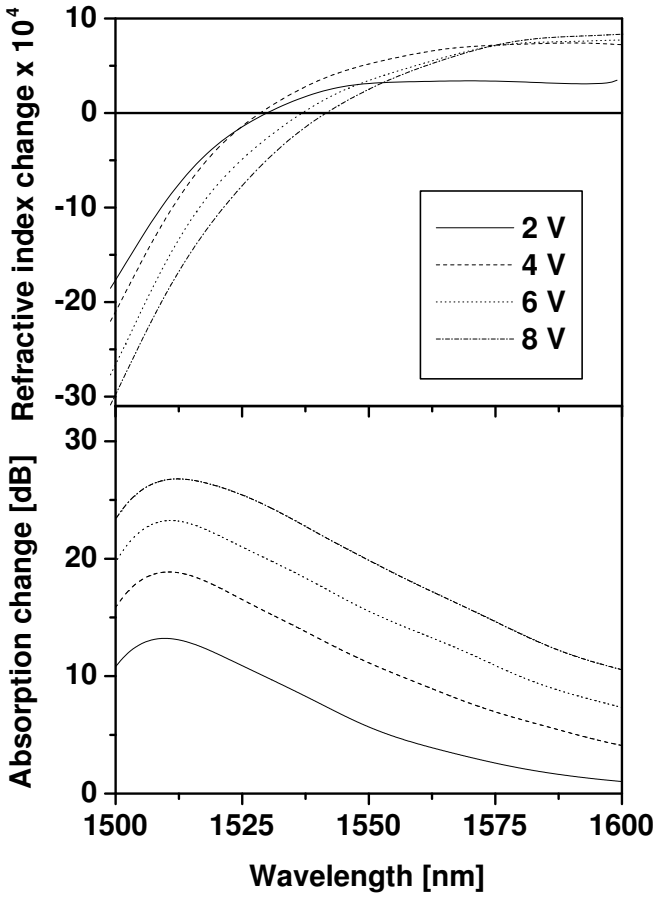

Figure 5.17: Lower graph: Calculated change in the absorption spectra with respect to 0 V (Calculations by S. Højfeldt (SCOOP/COM)). Upper graph: The accompanying refractive index change spectra. Note that the wavelength where the absorption change is highest ($\sim$1510nm) the α_H-parameter is negative due to the reduction in refractive index following the increase in reverers bias. This shows that the EAMs can be optimized for both chirp and extinction ratio at the same time.

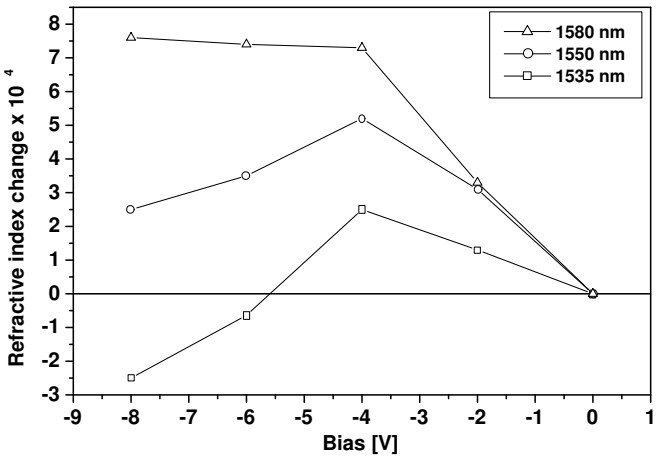

Figure 5.18: The refractive index change as function of the bias derived from the calculated absorption spectra for the wavelengths 1535 nm, 1550 nm and 1580 nm. The trends of the measured refractive index change are recognized.

Therefore, both high pulse extinction ratio and negative chirp is possible in EAMs. The price is however an increase insertion loss, estimated from the calculated absorption curve at 0 V to be ∼5 dB more than at 1550 nm.

To compare the measured and calculated refractive index changes directly, the calculated refractive index changes at 1535 nm, 1550 nm and 1580 nm as function of the bias is shown in Figure 5.18. Even though the calculated absorption spectra fitted the measured well, the calculated refractive index change does not fit the measured refractive index change. The reason for the discrepancy is not well understood, but differences between the actual absorption change and the calculated, higher in the band is likely to be the explanation. Due to the limited wavelength range of the measured absorption spectra, this has not been investigated further. However, the magnitude of the refractive index change is comparable to the measured and some of the trends observed from the measured data can be recognized. The refractive index increases initially with increasing reverse bias, but decreases again as the reverse bias is increased further. A higher refractive index change is possible for a longer wavelength. The refractive index change is reduced less after the peak as the wavelength is increased. The shift of the refractive index change peak is not observed. However, the very few points on the curves could mask this effect.

5.8 Discussion of available measurement techniques

During the last 20 years many techniques have surfaced for measuring the chirp, the phase or directly the α_H-parameter of external modulators. One of the simplest techniques, conceptually, is a technique where the chirp is measured on a bit pattern by inserting a monochromator between the component and the detector [73]. The bit patterns are stored as function of the wavelength of the monochromator and the full chirp and waveform can afterwards be reconstructed. The α_H-parameter can then be calculated from the chirp and the waveform. A high resolution monochromator is necessary to resolve low chirp.

Instead of using a monochromator as the frequency discriminating device, a passive Mach-Zehnder interferometer can be used. The technique is presented in the article by Saunders et al. [64]. The Mach-Zehnder interferometer has a sinusoidal wavelength transfer function. The period of the transfer function is known as the free spectral range and is determined by the path difference between the two arms. Only two measurement are needed to determine the chirp and the waveform of the bit pattern. The waveform is measured on the left and right flank of the transfer function. By left and right flank is meant the position on the transfer function where an increase in frequency increases or decreases the intensity transmission equally. From the two waveforms the intensity and the chirp can be calculated. The technique is limited by the fact that the width of the pulse spectrum must be less than half of the free spectral range. For short pulses a small chirp is therefore not easily resolved.

The advantages of these two techniques are that they measure the chirp at the bit-rate at which the component will be operated, when installed in a transmission system. The technique used by Saunders [64] was also tested using a fiber Mach-Zehnder interferometer with a free spectral range of 125 GHz. The interferometer was originally built for measuring the chirp from directly modulated semiconductor lasers, which is significantly larger than that for an EAM. It was therefore not possible to resolve the few GHz of chirp from the EAM using the interferometer. In collaboration with GiGA-An Intel Company, a commercial product based on this technique was tested. However, the system was too unstable with respect to alignment and polarization and the results were therefore not reproducible. Secondly, because the α_H-parameter is inversely proportional to the derivative of the intensity of the waveform with time, it is only well defined on the slopes of the waveform.

The most popular alternative to the frequency discriminating technique, is the fiber response technique by Devaux et al. [69]. The technique is based on the fact that the optical field, generated by modulating the intensity at the output of a laser or an external modulator, contains not only the fundamental harmonic of the modulation but also higher harmonics. Therefore, when the optical field is coupled into a standard single mode fiber, the intensity after propagation will beat as function of the modulations frequency, because the

harmonics travel at different speeds, due to the dispersion. Since the phase of the harmonics will depend on the α_H-parameter, the α_H-parameter can be extracted from the data acquired by modulating the component with a small-signal and detecting the beating as function of modulation frequency after propagation through the fiber. The small-signal modulation and detection is done using a network analyzer. The bias dependent α_H-parameter can be measured by consecutive small-signal measurements for different bias settings. The advantage of the technique is that it uses standard equipment. However, only the α_H-parameter is measured and therefore a calculation of the actual chirp on a bit pattern generated by the component needs a separate static measurement of the intensity transfer function. Together with the intensity transfer function, the phase transfer function can be calculated and thereafter the chirp. The advantage of this technique over the frequency discriminating techniques is that the α_H-parameter is directly measured. The technique is more reliable. However, many measurements are required to fully trace out the α_H-parameter as a function of reverse bias.

The most reliable commercially available technique is called the "Optical Analyzer" from the French company Apex. The technique is based on measuring the spectrum of the bit pattern. The amplitude and phase sensitive detection scheme in the Optical Analyzer enables a full characterization of the light in the spectral domain. By a Fourier transformation to the temporal domain, the waveform intensity and chirp can be calculated. The instrument was tested by the author and was found very reliable. However, the technique only works with a periodic bit-pattern due to the Fourier-transformation. As for the spectral discriminating techniques, the α_H-parameter is only well determined within the slopes of the intensity waveform.

The heterodyne technique presented in this chapter is a large-signal technique compared to the fiber response technique, and the full transfer function of the component is characterized at realtime in one single experiment. Calculation of the α_H-parameter as a function of the bias is very simple compared to the fiber-response technique. Techniques based on frequency discrimination are not able to give an α_H-parameter as function of the bias and usually an effective α_H-parameter is calculated from the frequency chirp and intensity measured at the half intensity on the pattern, the α_H^{3dB}-parameter. The heterodyne technique has the disadvantage of performing a static measurement of the insertion loss, phase and the α_H-parameter. The response of the component when modulated at 10 Gb/s or 40 Gb/s cannot, without assumption, be predicted. However, the same problem is present for the fiber response technique.

The heterodyne measurement technique presented in this thesis is technically difficult, primarily because of the use of the pulsed laser source. However, the pulsed operation of the probe and reference is not necessary for the

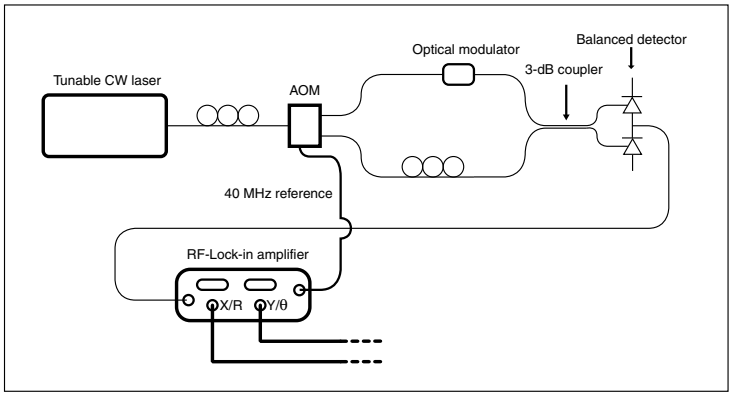

Figure 5.19: Schematic illustration of the proposed heterodyne set-up for detection of the amplitude and phase transfer function using a CW tunable laser source and fibers. The set-up should enable high sensitivity and simple measurements of the wavelength dependency of the component transfer functions.

measurement of the amplitude and phase transfer function in the heterodyne scheme. In Figure 5.19 is shown a proposed set-up, where the laser source is a tunable laser and the optical part of the set-up is fully integrated in fibers. The time delay in the reference arm is not necessary when the CW light is used. However, polarization controllers are necessary to optimize the polarization. An RF lock-in amplifier is necessary for the detection of the heterodyne signal since only the 40 MHz beating is present. The rest of the detection is equivalent to the pulsed heterodyne scheme. The CW operation of the heterodyne scheme increases the duty cycle of the measurement compared to the 300 kHz repetition rate system and thereby increases the signal to noise ratio. The modulation speed of the component can be increased and is only limited by the 40 MHz. The tunable laser source enables an easy measurement of the wavelength dependence of the transfer curves. The CW scheme has multiple advantages and will hopefully be realized in near future.

5.9 Summary

A new technique for measuring the amplitude and phase transfer functions of an optical modulator as function of the bias has been presented. The technique is based on a heterodyne detection scheme and is used to characterize EAMs in a large signal regime.

The amplitude and phase transfer functions of an EAM with high quantum

well barriers has been measured for a reverse bias ranging from 0 V to 10 V. The measurements were done at 1535 nm, 1550 nm and 1580 nm. The results showed that by increasing the reverse bias, the component α_H-parameter goes from positive to negative. The cross-over reverse bias increases with the wavelength, explainable with a simple "box"-description of the absorption edge. For a given wavelength, operation above the cross-over reverse bias results in negatively chirped pulses. Operation below the cross-over reverse bias results in positively chirped pulses. Operation at close to the absorption edge is shown to be advantageous both with respect to the extinction ratio and the chirp. The α_H-parameter ranges from -2 to 10.

From the measured amplitude and phase transfer functions, the intensity waveform and chirp was calculated for a 10 Gb/s NRZ modulation of the bias applied to the EAM. The electrical signal has a 3 V_{pp} amplitude. The component performance at 1550 nm for an offset bias of -1.5 V, -2.5 V and -4.5 V was investigated. The optimal offset bias, with respect to extinction ratio was found to be -2.5 V, resulting in a 8.2 dB extinction ratio. Chirp-wise, the optimal operation offset bias is -4.5 V, where the pulse is negatively chirped with a maximum instantaneous frequency deviation of $\sim$1 GHz. The high extinction ratio and negative chirp comes however at the expense of an increased insertion loss. The intensity waveform and chirp calculated for an offset bias of -2.5 V at 1535 nm, 1550 nm and 1580 nm shows, that both with respect to the extinction ratio and chirp, operation at 1535 nm is advantageous. The extinction ratio is 10 dB and the leading edge of the pulse experiences first a red-shift of -1.8 GHz and then a 2 GHz blue-shift. The trailing edge experiences the opposite chirp, due to the symmetry of the electrical signal. Operation closer to the absorption edge increases the insertion loss.

It is demonstrated that effective α_H-parameters should be used with great caution. The strong dependence of the α_H-parameter on the reverse bias makes it difficult to describe the EAM chirping properties by a single effective α_H-parameter.

A comparison between a high barrier component and a low barrier component shows that with respect to extinction ratio and chirp, the low barrier component is performing best. However, the insertion loss of the low barrier component is higher than for the high barrier component. The insertion loss difference is primarily due to higher passive losses in the low barrier component. A better processing of the components could solve this problem.

The refractive index change has been calculated from the calculated absorption change spectra. The calculated index change does not fit the measured refractive index change well. However, some of the trends observed experimentally can also be observed from the calculated refractive index change. It is shown that the wavelength at which the extinction ratio per volt is highest is accompanied with a negative α_H-parameter. The measurements and calcu-

lations show, that EAMs generate high quality pulses for fiber transmission, given the right operation wavelength, drive voltage and offset bias.

Chapter 6

Optical modulation of absorption and refractive index

Optical bleaching of the absorption in electroabsorbers has been shown to be applicable for all optical signal processing in telecommunication. As mentioned in Chapter 2, several record experiments have been realized within all-optical wavelength conversion and all-optical demultiplexing using cross-absorption modulation in semiconductor electroabsorbers. In both cases, a high absorption bleaching and a fast recovery are important and dependent on the reverse bias applied to the electroabsorber and the optical power injected into the component.

This chapter reports the measurement of the absorption bleaching and the recovery dynamics of an InGaAsP MQW waveguide electroabsorber in a large-signal experiment. The optically induced absorption change is comparable to the extinction ratio necessary for wavelength conversion and demultiplexing in optical telecommunication systems.

Secondly the time resolved index dynamics accompanying the absorption bleaching is reported. A simple explanation for the observed dynamics will be given. From these measurements, the chirp of wavelength converted pulses can be discussed and operation points for high extinction ratio and preferable chirp can be found. The measurements are done using the heterodyne measurement technique in the pump-probe configuration.

6.1 The field enhanced saturable absorber

In the previous chapter, the transmission in the waveguide electroabsorber was modulated by changing the reverse bias applied to the component. Due to the operation principle this component is called an electroabsorption modulator. The physical process behind the all-optical modulation of the transmission in an electroabsorber is the saturation of the absorption by optical carrier generation. In the all-optical operation scheme the component is therefore denoted a saturable absorber.

There are many types of semiconductor saturable absorbers; the proton bombarded [74], ion implanted [75] low temperature grown [76] and the field enhanced [77]. In the proton bombarded, ion implanted and low temperature grown saturable absorbers the carrier lifetime is reduced by creating recombination centers in the semiconductor material speeding up the absorption recovery. These types of saturable absorbers are typically used as the nonlinear element in passively mode locked laser cavities, see for example [22]. In the field enhanced saturable absorber the carrier lifetime is reduced by externally applying a field across the absorptive region, thereby sweeping the charged carriers out of the device.

There are two possible geometries of operation of the saturable absorber. In one, the optical field propagates along the normal to the quantum wells [78]. In the other the light propagates along the plane of the quantum wells in a waveguide. The latter scheme is preferable for all-optical signal processing, since the increased interaction length ensures an efficient absorption of the optical field and therefore an increased absorption change.

Instead of addressing the component as the field enhanced multi quantum well semiconductor waveguide saturable absorber it will simply be the saturable absorber.

In principle the temporal dynamics of the saturable absorber should be simple. The carriers generated by the optical field bleach the absorption. As the carriers are swept out of the active region the absorption recovers. However, the picture is more complicated:

1. The component is reverse biased. The increased field over the active region of the component red-shifts the absorption edge compared to the unbiased saturable absorber.

2. When the optical field is absorbed in the component, the electron and hole states are excited. The exclusion principle prohibits further absorption in the filled states. The absorption has therefore been reduced by the so-called band filling effect [79].

3. The photo-generated carriers thermalize by carrier-carrier scattering and

phonon-carrier scattering to a Fermi distribution with the lattice temperature [80].

4. The force exerted by the field on the carriers will pull the electrons and the holes towards the n-doped and the p-doped side of the heterostructure, respectively. Initially, the carriers will be confined to the quantum wells, but with time the carriers will escape due to tunneling through or thermionic escape over the barriers [81, 82]. As the carriers are swept out of the quantum wells, the absorption recovers. Due to the different masses, localization potential and mobility of the electrons and the holes, the escape times are not necessarily equal [83, 84].

5. As the electrons and holes travel through the intrinsic region of the saturable absorber they represent a space-charge. The externally applied field is screened by the spatially distributed electrons and holes. The reduced field results in a blue-shift of the absorption edge, explained by the quantum-confined Stark effect [83, 85]. A second effect of the reduced field over the intrinsic region is, to reduce the sweep-out time of the carriers, since the force exerted by the external field is reduced.

6. Finally, after the drift and diffusion of the electrons and the holes out of the intrinsic region, through the separate confinement potential step to the doped regions, the component has recovered completely. However, carrier pile-up at the separate heterostructure confinement layer has been reported and shown to increase the component recovery time [86, 87, 88].

The band filling, the thermalization and the field screening effect act together to give a complicated absorption bleaching and recovery dynamics. They all contribute differently to the dynamics, depending on the material system, the heterostructure design, the wavelength, the photo-generated carrier density and the externally applied reverse bias. It is therefore difficult to directly compare our component measurements with results reported in the literature. However, the trends seen in our measurments agree with the trends in the literature and more importantly it will be shown that the components optimized for operation as EAMs can be operated as fast saturable absorbers and be used for wavelength conversion and demultiplexing at high bit-rates.

6.2 Experimental considerations for the pump-probe measurements

6.2.1 Pump and probe wavelength

Based on the measurements presented in Chapter 3 of the field induced absorption change and the insertion loss, the investigations of the electroabsorbers as

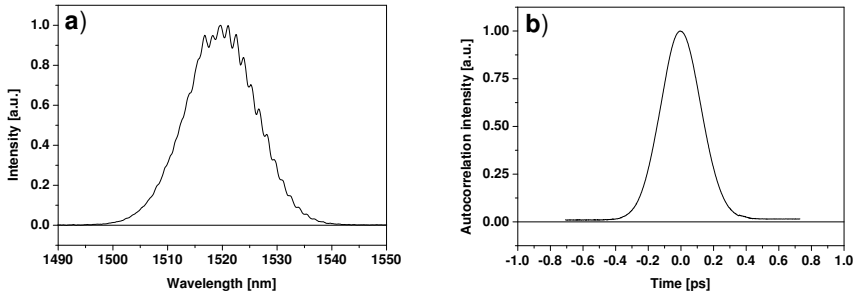

Figure 6.1: a) Pulse spectrum measured using a monochromator. The intensity-FWHM is measured to be ∼15 nm, b) Measured pulse auto-correlation. The pulse intensity-FWHM is approximately 200 fs, assuming a Gaussian pulse shape. The measurement was done using a second-harmonics generation autocorrelator.

saturable absorbers were chosen to be performed at 1520 nm. At this wavelength, the increase in absorption with the reverse bias is high, and therefore the magnitude of the absorption bleaching as function of reverse bias can be easily measured. Measurements at 1550 nm showed only a small amount of absorption bleaching for high reverse biases and high pump powers. This is explained by the lower absorption at this wavelength. Figure 6.1 a) shows the measured pulse spectrum. The intensity-FWHM of the spectrum is ∼15 nm. Figure 6.1 b) shows the measured pulse intensity autocorrelation, from which the pulse intensity-FWHM was found to be approximately 200 fs (assuming a Gaussian pulse shape). Both pump and probe pulses are TE polarized.

6.2.2 Probe pulse energy

The appropriate probe pulse energy for the pump-probe experiment is an important issue. Because the probe should only measure the pump induced absorption change and not itself affect the measured absorption, the energy of the probe pulse must be small. However, the reverse bias applied to the component is as high as 10 V, in some cases resulting in more than 35 dB of insertion loss at 1520 nm. Therefore the probe signal at the output of the component can be very small. For measurement of the absolute absorption change, the transmission of the probe without the pump has to be measured. The intrinsic laser intensity noise will if the probe energy is too small, result in an unacceptably high noise on the measured absorption change. Figure 6.2 shows a measurement of the absorption change in a saturable absorber with the probe being

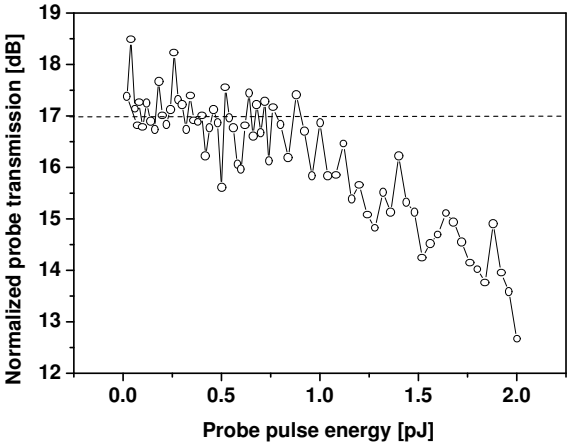

Figure 6.2: Example of a measurement of the probe pulse effect on the pump-probe measurement on a saturable absorber. The probe was delayed by 1 ps with respect to the pump. The probe pulse should not affect the measurement, which is also the case for probe pulse energies below 1 pJ. Above 1 pJ the pulse energy is high enough to induce a self-bleaching and the probe transmission change is decreased.

delayed 1 ps with respect to the pump. The parameter varied is the probe pulse energy. The probe pulse has a negligible effect on the measurement up to 1 pJ, where the pump induced increase of the probe transmission is ∼17 dB. From 1 pJ to 2 pJ the absorption change is reduced by ∼3 dB. This is caused by the self-bleaching of the absorption by the probe. Therefore, the probe pulse energy was generally chosen to be in the 0.5 to 1 pJ range.

6.3 Measurement of the absorption bleaching and recovery

The measurements of the absorption dynamics was performed on the 250 μm long electroabsorber with high barriers, which has also been used for the measurements reported in the previous chapters.

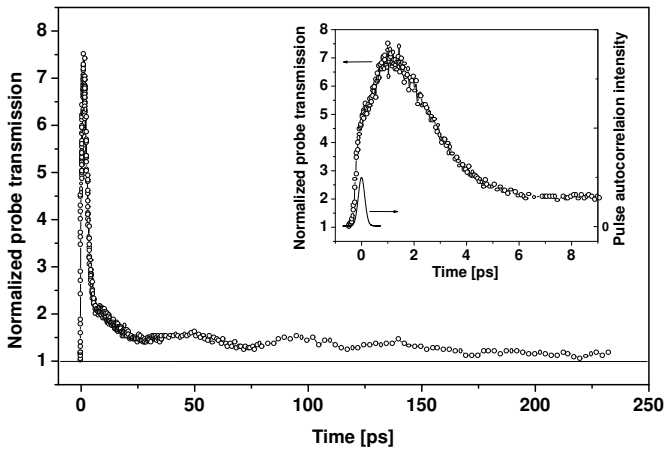

Figure 6.3: Pump induced probe transmission change, normalized to the probe transmission without the pump. The time on the x-axis is relative to the pump pulse arrival. The pump energy is 3 pJ at the facet of the component and the component is reverse biased with 10 V. The pump-probe delay is scanned from -500 fs to 230 ps. The inset shows the probe transmission within the first 9 ps after the pump pulse arrival. The measured pulse autocorrelation, from Figure 6.1 is also shown.

6.3.1 General trends

Figure 6.3 shows the characteristic dynamics of the saturable absorber on a long and short time scale. The time on the x-axis is relative to the pump pulse arrival. The component was reverse biased with 10 V and the pump pulse energy was 3 pJ at the facet of the component. The coupling loss is 2–3 dB, including the reflection. The confinement factor is approximately 0.075 for this 5 quantum well structure. The inset shows the fast dynamics. When the pump pulse enters the component, the probe transmission is increased instantaneously. After the pump-probe pulse overlap the transmission continues to increase. However, after a couple of picoseconds the transmission decreases again with a time constant on the order of a few picoseconds. This is followed by a long recovery time of more than 100 ps. The following sections will present and discuss the measured dependency of the absorption dynamics on the reverse bias, the pump pulse energy and the quantum well structure.

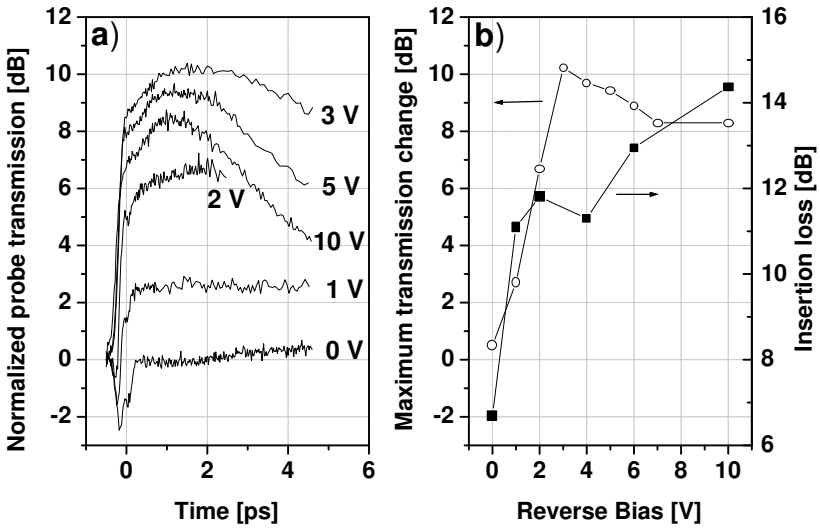

Figure 6.4: a) The normalized pump induced probe transmission change shown on a dB scale for the first 6 ps after the pump pulse arrival. b) The size of the maximum absorption bleaching, which increases with reverse bias until 3 V and decreases again when the reverse bias is increased further up to 10 V. The insertion loss of the component is also shown as function of the reverse bias.

6.3.2 Bias dependent absorption dynamics

Magnitude of the absorption bleaching

Figure 6.4 a) shows the measurement of the absorption bleaching taking place in the first couple of picoseconds. The pump pulse energy is 3 pJ at the facet of the component. The reverse bias is varied from 0 V to 10 V. First of all, it is observed that the pump induced probe transmission change depends strongly on the bias applied. At 0 V of reverse bias a negligible change is observed, while the absorption is reduced by more than 10 dB at 3 V of reverse bias. The maximum bleaching of the absorption, deduced directly from the measured data, is shown in Figure 6.4 b). It is observed that increasing the reverse bias from 0 V to 3 V increases the maximum absorption bleaching. Increasing the bias from 5 to 10 V, reduces the overall bleaching again. The trend is understood from a combination of the absorption edge red-shift and the decreased carrier sweep-out time. Figure 3.7 in chapter 3 shows an increase in the absorption

at 1520 nm for an increased reverse bias. When the absorption increases, the pump is more efficiently absorbed and as a consequence the amount of carriers being excited is increased. Therefore the band filling becomes more important and the pump induced probe transmission change is increased [85]. Secondly, as the reverse bias is increased, the sweep-out time of the carriers from the intrinsic part of the structure is decreased. The absorption recovers more quickly, which results in a reduced probe transmission.

The interplay between the increased insertion loss accompanying an increased bias, and the bias dependent absorption bleaching can be elucidated by coupling the measurement shown in Figure 6.4 a) with the component loss measured in Chapter 3. Figure 6.4 b) shows the maximum absorption bleaching as well as the saturable absorber insertion loss. The insertion loss is defined as the static component loss (at the bias of interest) minus the bleaching induced by the pump. The component insertion loss increases with the reverse bias, being ~ 7 dB at 0 V and ~ 14 dB at 10 V of reverse bias. Operation at 0 V bias is accompanied by less than 1 dB of absorption bleaching and can, even though the component insertion loss is low, not be used for switching or wavelength conversion. For the highest absorption bleaching of 10 dB, attained at 3 V of reverse bias, the component insertion loss is ~ 12 dB. At this point the absorption bleaching or extinction ratio is for some cases enough for demultiplexing. The extinction ratio necessary for demultiplexing varies from 5 dB to 15 dB, depending on factors such as the bit-rate and the detector bandwidth [89, 90]. The recovery time of the absorption bleaching is also important and the recovery time might not be fast enough at 3 V of reverse bias for switching signals at the bit-rate of interest. Operation at higher reverse biases will indeed decrease the recovery time, however the extinction ratio also decreases and the component insertion loss increases. Operation at 10 V of reverse bias shows a fast absorption recovery, however the component insertion loss also becomes ~ 14 dB and the extinction ratio decreases to 9 dB. The decreased extinction ratio and insertion loss can be compensated by increasing the pump energy and thereby bleach the absorption more effectively. This is however, at the expense of a longer recovery time, because of the increased amount of carriers to be swept out of the active region.

It can be concluded, that the optimum operation bias of the saturable absorber for signal processing can not be deduced from a discussion of the extinction ratio and insertion loss alone. Recovery of the absorption bleaching, both as function of the pump energy and component reverse bias is also important. Before entering into this discussion, the processes behind the absorption bleaching will be discussed.

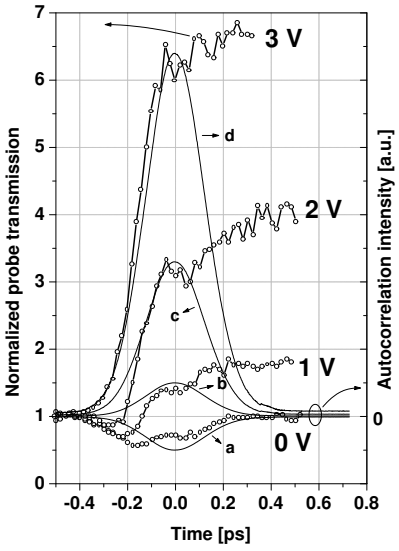

Figure 6.5: Response of the saturable absorber within the first picosecond. The pump energy is 3 pJ and the saturable absorber is reverse biased by 0, 1, 2 and 3 V. The measured data is represented by the line-symbol curves. The curves "a", "b", "c" and "d" are the measured pulse autocorrelation with different amplitudes. For increasing reverse bias the absorption bleaching becomes well represented by spectral hole burning, rising with the shape of the pulse autocorrelation function. A decrease during the pump and probe pulse overlap is also also observed, and an explanation is likely to include two-photon absorption, the coherent artifact and the spectral artifact.

Dynamics of the absorption bleaching

As seen from Figure 6.4 a) the absorption bleaching comprises multiple effects, all dependent on the bias applied to the component. The measured fast sub-picosecond response[1] is shown in Figure 6.5. For 0 V bias, the transmission is decreased within the pulse overlap between pump and the probe. This is opposite to the response expected from an absorption bleaching. The probe transmission decrease is primarily attributed to two-photon absorption. The

[1]The curves shown in Figure 6.5 are "zoomed" versions of the curves shown in Figure 6.4 a). The delay step size can be varied during a pump-probe trace and is therefore chosen to be small to resolve the initial fast dynamics while increased when measuring the slow recovery dynamics. This ensures that in a single pump-probe scan both the fast and the slow dynamics is well resolved.

two-photon absorption involves one photon from the pump and one photon from the probe pulse, which together excite a carrier at the sum energy. The two-photon absorption between the pump and probe is well documented in pump-probe measurements in semiconductor optical amplifiers [51]. The signature is a decrease in the probe transmission having the same shape as the cross-correlation of the pump and probe pulse. In Figure 6.5 is also shown the measured autocorrelation shape of the laser pulse for different amplitudes (solid lines). Curve "a" shows the expected shape of the two-photon absorption response of the component. The shape of the measured data is not well represented by this curve, which is explained by the fact that a multitude of other effects come into play within the pump and probe pulse overlap.

The coherent interaction between the pump and the probe, called the coherent artifact, is known to contribute to the pump-probe signal when pump and probe are temporally overlapped. The process is analogous to four-wave mixing, where two optical fields generate a polarization grating in the material on which a third field is diffracted. In a pump-probe measurement, part of the pump will be diffracted on the polarization grating generated by the pump and the probe and be superposed to the measured incoherent probe signal [91].

The spectral artifact is an effect shown to influence the nonlinear response of semiconductor amplifiers [92]. It arises from the coupling between the wavelength-dependent gain and the refractive index changes and appears within the optical pulse envelope. The index change correspond to change of the instantaneous wavelength during the pulse, which will therefore feel a variable gain due to the wavelength-dependent gain. The refractive index change generated within the pulse envelope is explained by the optical Stark effect [93]. As will be shown later in this chapter, a large refractive index change is experienced during the pump and probe pulse overlap in the saturable absorber. During the leading edge of the pump, the probe will therefore be blue-shifted by ~ 10 nm. It thereby experiences an increased absorption. During the trailing edge of the pump, the probe is red-shifted and experiences therefore a reduced absorption. This prediction seems to agree trend-wise with the measured dynamics at 0 , 1 and 2 V, where the leading part, within the pump-probe overlap experiences an increased absorption, while the trailing edge is absorbed less. The spectral artifact contribution to the pump-probe dynamics has not been investigated in saturable absorber, but could be an important contribution to the ultra-fast dynamics, due to the steep absorption edge.

As the reverse bias is increased, the absorption bleaching increases as observed for the 1, 2 and 3 V curves in Figure 6.5. The carriers are excited within the narrow spectral band of the pulse spectrum, which "burns" a hole in the absorption spectrum [94]. The process is therefore named spectral hole burning. Both measurements and modelling on saturable absorbers have reported the effect of spectral hole burning [79]. The signature of the spectral hole

burning in the saturable absorber is an absorption bleaching, rising with the cross-correlation shape of the pump and the probe. For 3 V of reverse bias and beyond (not shown), the rise of the absorption bleaching is well represented by the shape of the laser pulse autocorrelation. In the intermediate bias points the transmission reduction, present mainly at 0 V, and the spectral hole burning are competing.

After band filling through spectral hole burning, the probe transmission is seen to continue increasing. In Figure 6.4 a) an additional absorption bleaching of more than 1 dB is following the spectral hole burning for biases above 2 V. At 0 V and 1 V, the additional rise is negligible. Carrier generation from optical absorption of the pump can not be the reason for the additional bleaching of the absorption, since the transmission continues to increase during more than 1 ps after the arrival of the 200 fs pump. In bulk GaAs/AlGaAs saturable absorbers, the absorption bleaching is seen to recover almost completely after the spectral hole burning and during the following $\sim$5 ps it increases again, before a slow recovery finally sets in [77]. The effect of the fast recovery after the spectral hole burning is explained and modelled by a carrier heating process governed by the carrier-carrier scattering. The fast carrier-carrier scattering time, decreases the carrier density within the energy band probed by the spectrally narrow probe. As the carriers thermalize to the lattice, via phonon-carrier scattering, the density of carriers at the probe wavelength increases again. The thermalization of the quasi-fermi distribution to the lattice temperature explains the second component of the increase of the probe transmission in the bulk saturable absorber. In a single GaAs/AlGaAs quantum well saturable absorber the signatures attributed to carrier heating and cooling were not as pronounced as in the bulk [77]. The explanation was based on the fact that the carrier heating process in the bulk was partially due to field heating of the carriers. In the single QW sample the more energetic carriers are sweept out of the quantum well and therefore contribute less to the carrier heating compared to case of the bulk saturable absorber.

The effect of field screening is also contributing to the transmission increase after the pump pulse arrival. The space charge represented by the escaped electrons and holes from the quantum wells reduces the field over the quantum wells. As measured and modelled by Cavailles et al. the field screening contribution to the magnitude and sign of the absorption change depends on the wavelength and bias [83]. From the measurements presented in both Chapter 3 and Chapter 5 the absorption is seen to be reduced when the field is reduced. This is in accordance with the increased probe transmission observed after the pump pulse. A simulation performed by S. Højfeldt (SCOOP/COM) on similar InGaAsP MQW components also shows that the delayed increase in the absorption bleaching can be explained by the field screening, without including thermalization processes [46]. The simulation results relevant for the

experimental result presented in this chapter are all shown in Figure 6.8 on page 87. Concerning this discussion, Figure 6.8 a) is relevant. Here the absorption bleaching due to band filling and field screening are shown separately, together with the pump pulse. Spectral hole burning was not included in the model and therefore the absorption bleaching due to band filling does not increase instantaneously. It is clearly seen that the field screening contribution to the absorption bleaching is delayed with respect to the band filling induced absorption bleaching.

The time delay at which the absorption bleaching peaks, decreases from $\sim$ 2 ps at 3 V of reverse bias to $\sim$1 ps at 10 V of reverse bias. Miller et al. have reported the same observations, concluding that the increased escape-rate from the quantum wells also speeds up the field induced absorption bleaching [85].

Absorption recovery

Figure 6.6 shows the measurement results of 5 pump-probe scans with a reverse bias applied to the component ranging from 0 V to 10 V. The pump energy is, as before 3 pJ. As previously discussed, the transmission change induced at 0 V is negligible due to the low material absorption. For 1 V, the absorption recovery is described well by a single exponential decay. As the reverse bias is increased further, the recovery can only be described by two time constants. Both the fast and the slow decay time decrease for increasing reverse bias, which is in agreement with the fact that the carrier sweep-out rate from the intrinsic region increases with the reverse bias. Figure 6.7 a) shows the same pump-probe curve for 10 V of reverse bias as shown in Figure 6.6, but on a linear scale. Superposed is a fitted double exponential function. The measured data are generally well represented by this function and Figure 6.7 b) shows the two time constants as function of the reverse bias for 1 V to 10 V of reverse bias. The 0 V transmission curve is too noisy for fitting the double exponential function. The decay time of the fast component shows a strong dependence on the reverse bias and decreases from 200 ps to 2.5 ps when going from 1 V to 10 V of reverse bias. The slow component is less dependent on the reverse bias and decreases from 200 ps at 1 V to 93 ps at 10 V of reverse bias. The amplitude of the fast and slow component of the double exponential function is shown Figure 6.7 c). The recovery is mainly dominated by the fast component when the reverse bias is 3 V or higher.

The escape rate from the quantum wells through thermionic escape and tunneling depends on both the confinement potential and the carrier mass [95]. It was demonstrated that the hole escape from quantum wells was faster than the electron escape by a factor of 2.5 in certain InGaAs/GaAs unstrained quantum well structures [84]. The difference in escape times was explained by the lower confinement potential of the hole compared to the electron. The

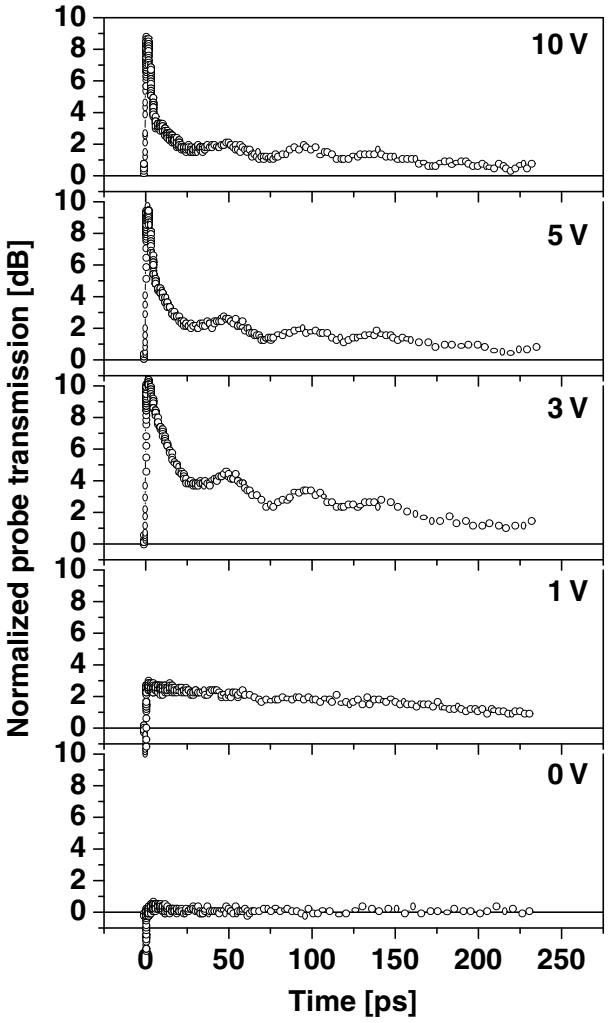

Figure 6.6: Normalized pump induced transmission change of the probe shown on a dB scale. The reverse bias is 0 V, 1 V, 3 V, 5 V and 10 V and the pump pulse energy is 3 pJ. The overall absorption recovery is faster for increasing reverse bias. The absorption recovery is best described by two time constants when the reverse bias is between 3 V and 10 V. A short time constant on the order of a few picoseconds and a long time constant on the order of 100 ps. The oscillations observed on the long recovery tail have not been explained, but are discussed in the text.

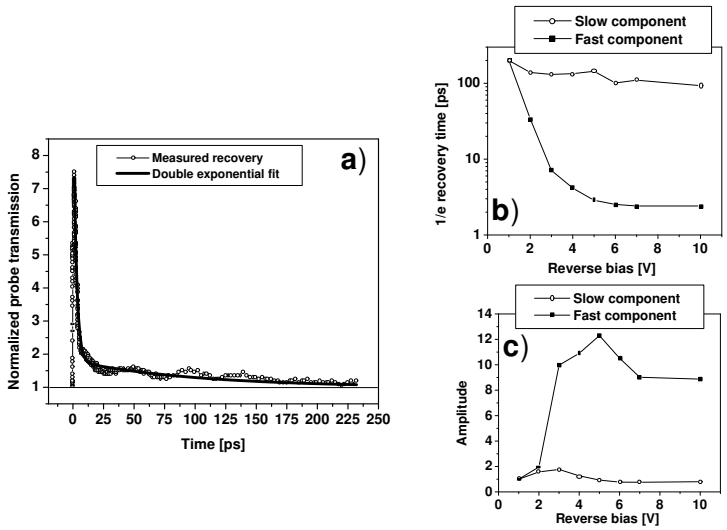

Figure 6.7: a) Normalized probe transmission on a linear scale as function time delay between the pump and the probe pulse. The pump pulse energy is 3 pJ and the reverse bias applied to the component is 10 V. The full line is a double exponential fit to the data. b) Time constants for the slow and the fast component of the exponential fit versus reverse bias. c) shows the amplitude of the slow and the fast components in the exponential fit.

conduction and valence band offsets in the component reported on here, were designed with an effort put into compensating for the difference in the electron and hole masses, and thereby the premature delocalization of the electrons [45]. However, if this is successfully done is difficult to say. Therefore part of the double exponential behavior could be due to different escape times for the electrons and holes.

Measurement and calculations performed by Brovelli et al. concluded that the carrier escape from a quantum well is generally too fast to explain the slow absorption recovery in saturable absorbers [95]. In agreement with the results of Yoshida et al., carrier induced field screening is shown to lengthen the carrier escape from the active region [86]. Simulations performed by S. Højfeldt (SCOOP/COM) on similar InGaAsP MQW components are shown in Figure 6.8. Figure 6.8 c) shows two active region designs, differing only by the separate confinement heterostructure having either one or two steps. Graph d) shows that the two step structure is faster than the single step structure.

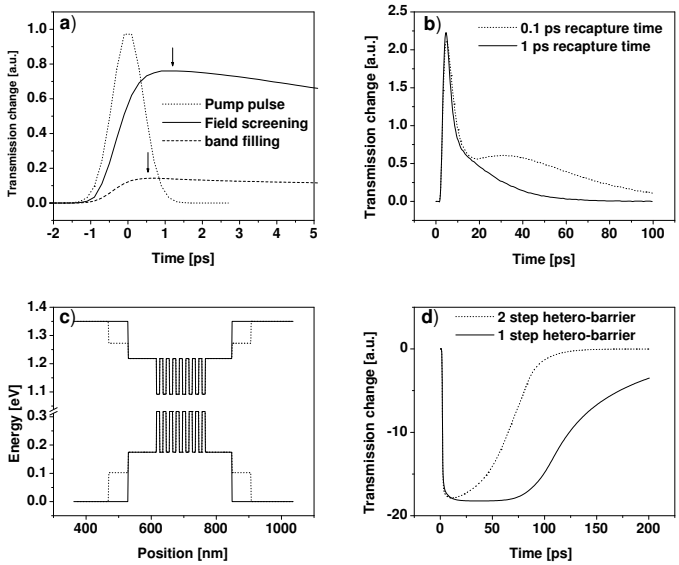

Figure 6.8: Simulation results on InGaAsP MQW components, provided by from S. Højfeldt (SCOOP/COM). a) Band filling and field screening contributions to the absorption dynamics following excitation by a 1 pJ and 1 ps intensity-FWHM pulse. Spectral hole burning is not included. The arrows indicate the delay at which the band filling and the field screening induced absorption bleaching peaks. It is observed that the field screening contributes to delaying the peak of the absorption bleaching. b) Illustration of the effect of carrier recapture in a 8 QW structure. A high recapture rate increases the decay time by adding a slowly recovering tail, similar to the measured results. c) Band diagram for two structures, one with a single step for the separate confinement heterostructure, and the other with two steps. d) Absorption change induced by the field screening alone, for the one and two step separate confinement heterostructure shown in c). For the single step structure the carrier pile-up is more important and the recovery becomes slower than in the two step structure.

This is due to the lowered probability of thermionic escape of the carriers in the single step structure [46]. This is in good agreement with the calculations of Yoshida et al. [86] and shows that the carrier pile-up at the edges of the separate heterostructure confinement layer does contribute to the absorption recovery. Figure 6.8 b) shows the effect of recapture. When the recapture time is decreased, the absorption shows a long recovery tail, which could explain the long recovery tail seen in the measured absorption dynamics.

The measured oscillations on the long tail of the recovery could not be explained. The period is approximately 50 ps (20 GHz). The oscillation frequency is independent of the pump pulse energy, the component reverse bias and the component length. The oscillations were also observed using a non-degenerate pump-probe set-up and it is therefore not an experimental artifact from the heterodyne pump-probe set-up. Experiments with and without a bonding wire to the component showed no difference on the size or period of the oscillations. Components with different metal contact size showed also the same period of the oscillations. It is, however, speculated that electrical reflections in the component or some resonance in the external circuit can be an explanation.

From an application point of view, the short initial recovery time of the absorption is promising for all-optical demultiplexing and sampling. However, the long recovery tail could be problematic when using the component as a wavelength converter, even at 10 Gb/s.

6.3.3 Dependence of the absorption dynamics on the pump pulse energy

From the bias dependence of the absorption dynamics it has been shown that for a 3 pJ pulse the highest absorption bleaching is reached with 3 V of reverse bias. The measurements have also shown that the recovery time can be reduced substantially by increasing the reverse bias beyond 3 V. However, when the reverse bias is increased beyond 3 V, the maximum absorption bleaching is seen to decrease again. To compensate this decrease, the pump pulse energy can be further increased, thereby generating more carriers, which will bleach the absorption more effectively. Figure 6.9 shows the normalized probe transmission on a dB scale for different pump pulse energies. The reverse bias applied to the component is 6 V. It is indeed observed that the absorption bleaching can be increased by increasing the pump pulse energy, being $\sim$2 dB at 1 pJ and 13 dB at 10 pJ. The maximum absorption bleaching induced by the pump is approximately proportional to the pump pulse energy. This is observed as a 3 dB increase in the absorption bleaching for a doubling of the pump power. This implies that the saturable absorber is operated in a linear regime where the absorption bleaching due to band filling increases linearly with the pump pulse energy and nonlinearities such as two-photon absorption are not important.

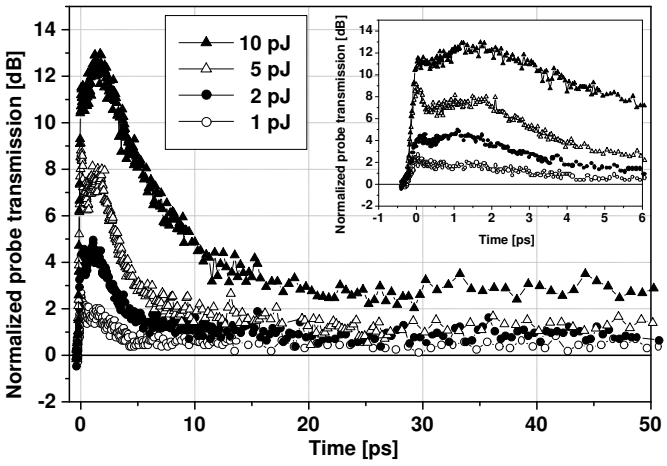

Figure 6.9: Measured probe transmission for different pump pulse energies. The component is reverse bias by 6 V. The increase in the absorption bleaching is approximately linear with the pump pulse energy which implies that the component is operated in a linear regime. The fast initial recovery time is almost independent of the pump pulse energy. The inset shows the response within the first 6 ps.

To cross-check this observation, a single pulse absorption measurement on the same component was performed. In this experiment, the material absorption as function of the energy of the pulse is measured. The result is shown in Figure 6.10. The experimental details are similar to the ones presented in [56]. The component was reversed biased with 6 V. The signature of the two-photon absorption is first present for pulse energies higher than 10 pJ (indicated by two-photon absorption in the figure). This is observed as an increase of the absorption for an increasing pulse energy [96]. For low pulse energies, the material absorption is independent of the pulse energy, indicated by small signal in the figure. As the energy is increased, the leading edge of the pulse starts to bleach the absorption. The remaining part of the pulse is then less absorbed and the component absorption is effectively lowered (indicated by absorption bleaching in the figure).

The inset of Figure 6.9 shows the first 6 ps of probe transmission as function of the pump pulse energy. As seen previously in Figure 6.4 the initial fast bleaching due to the spectral hole burning is followed by a further transmission increase, or in some cases only a shoulder. The bleaching peaks at increasing

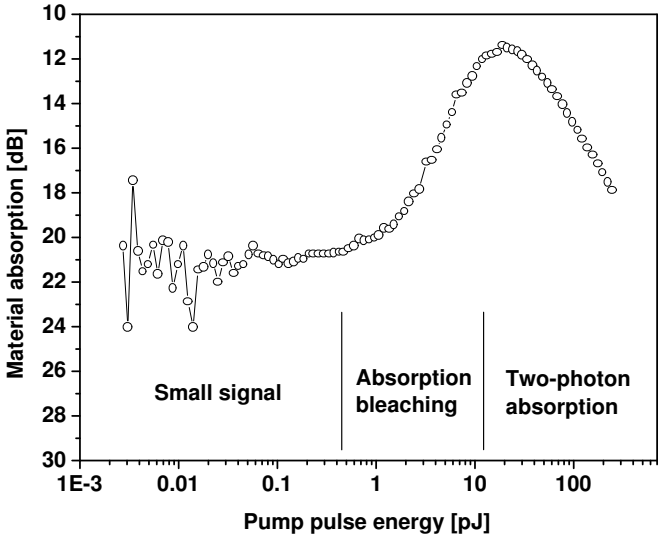

Figure 6.10: Measurement of the material absorption (modal) as function of the pulse energy for a 200 fs pulse at 1520 nm. The saturable absorber is reverse biased with 6 V. Three regimes are indicated, "Small signal": The regime where the absorption is independent of the pulse energy. "Absorption bleaching": The front edge of the pulse bleaches the absorption, reducing effectively the pulse absorption, and "Two-photon absorption": The pulse intensity is high enough that two-photon absorption becomes dominant.

delays for increasing pulse energies. This can be explained both by carrier heating relaxation and by absorption bleaching through field screening as discussed previously. Both effects are expected to take longer time as the carrier density is increased. At 5 pJ of pump pulse energy a decrease of the transmission is observed after the spectral hole burning. This agrees very well with the thermalization of the carrier distribution by carrier-carrier scattering after the spectral hole burning, as suggested by [80]. It is not understood presently why the spectral hole burning spike is only present at 5 pJ.

The fast absorption recovery takes place within the first 20 ps is almost independent of the pump pulse energy. After approximately 5 ps the transmission is reduced by 3 dB for all pulse energies (not measurable for 1 pJ). On the longer time scale the absorption is seen to recover to approximately the same level within 20 to 30 ps for pump pulse energies below 5 pJ. The long tail does not recover within the first 100 ps (not shown) but stays at approximately 1

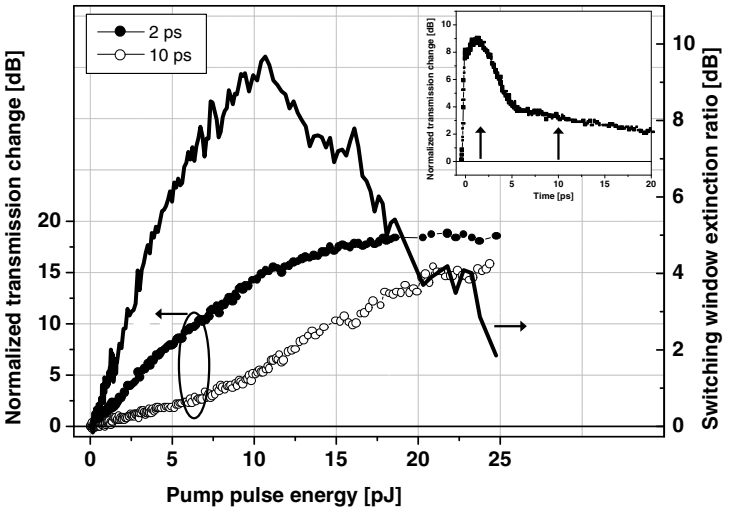

Figure 6.11: Measured probe transmission as function of the pump pulse energy for 6 V of reverse bias. The transmission is probed at 2 ps and 10 ps after the pump, as shown in the inset. The difference between the "2 ps"- and "10 ps"-curve, shown as the full curve, gives the extinction ratio possible for a 10 ps switching window as function of the input pulse energy. Up to 9.6 dB of extinction ratio is possible for 10.6 pJ of pump pulse energy.

dB. For 10 pJ of pump pulse energy the absorption does not recover to 1 dB of probe transmission change after 30 ps but stabilizes at approximately 3 dB which decays slowly to 1 dB within the following 200 ps. The long tail is of course worrisome with respect to applying the saturable absorber as a fast all optical modulator for high bit-rate signal processing. The comparable investigations by Karin et al. showed a full recovery of the absorption bleaching within 15 to 30 ps, depending on the pump pulse energy. The component was a single GaAs/AlGaAs quantum well waveguide saturable absorber [77]. The pump pulse energy in their experiment ranged from 4 pJ to 20 pJ coupled into the component, similar to our experiments. The recovery is faster than observed here (for comparable electrical fields), however only the probe transmission change ($\Delta T = T_{with-pump} - T_{without-pump}$, where $T_{with-pump}$ and $T_{without-pump}$ are the probe transmission with and without the pump, respectively) was reported and not the normalized probe transmission. Therefore the size of the absorption change is not known and could be small compared to the results presented here, which can explain the faster decay.

When applying the saturable absorber for all-optical demultiplexing or optical sampling, the absorption bleaching has to be large and the recovery time

has to be short. As seen from Figure 6.9, the increased absorption bleaching or extinction ratio accompanying an increased pump pulse energy, comes at the expense of a longer recovery time. The pump-probe set-up can be used to find the optimum pulse energy at which the extinction ratio is maximized while keeping the switching window short. This is done by measuring the normalized probe transmission as function of the pump pulse energy for a fixed pump-probe delay. Figure 6.11 (left axis) the absorption bleaching at 2 ps and 10 ps after the arrival of the pump pulse. In the inset, the arrows indicate the delay position of the probe with respect to the pump. The 2 ps delay is chosen to probe the maximum absorption bleaching possible. The "2 ps"-curve shows a clear saturation of the absorption bleaching with increasing pump pulse energy. The maximal absorption bleaching is 19 dB, reached at approximately 20 pJ. The material absorption is approximately 22 dB at -6 V, which shows that the absorption can almost be bleached completely. The inability to bleach the absorption completely is explained by the important two-photon absorption of the pump pulse for high energies, effectively reducing the pump pulse energy. The "10 ps"-curve is at all pump pulse energies below the "2 ps"-curve, as expected due to the absorption recovery.

The difference between the absorption bleaching curve at 2 ps and at 10 ps will be equal to the extinction ratio of a 10 ps switching window. This curve is also shown in Figure 6.11. The curve shows that the highest switching window extinction ratio is 9.6 dB and is attained by exciting the saturable absorber with 10.6 pJ of pump pulse energy. Both for increasing and decreasing pulse energies, the extinction ratio decreases. The optimum point is found where the bleaching at 2 ps is high while the recovery time is still short.

Using a similar component, it was shown that a 10 Gb/s channel could be demultiplexed from a 40 Gb/s OTDM signal, bit error free [3]. The switching window has to be approximately 25 ps. It was also shown that a 10 Gb/s channel could be demultiplexed from a 80 Gb/s channel, showing open eyes, however it was not possible to get the signal bit-error free. The switching window width has to be 12.5 ps in this case. This agrees well with the pump-probe measurement presented here, showing that the component can generate short switching windows. As mentioned previously, the extinction ratio required for the switching window is very dependent on the detection bandwidth and base rate. It is therefore difficult to conclude if the 9.6 dB measured here is sufficient to, for example switch a 10 Gb/s signal from a 100 Gb/s OTDM signal, which would need a 10 ps switching window. The long recovery tail at 10 pJ, showing a remanent 2 dB of absorption bleaching at 100 ps is worrisome, because the component should recover completely within 100 ps for demultiplexing to 10 Gb/s. However, it can be concluded that fast switching windows can be obtained using a saturable absorber by applying sufficiently high reverse bias and pump power.

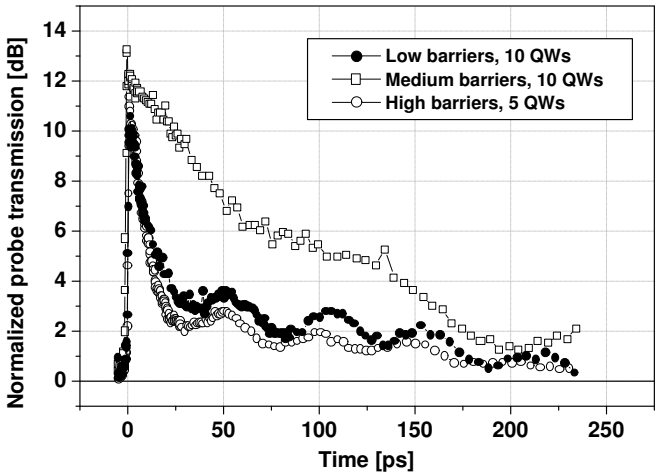

Figure 6.12: Normalized probe transmission measured on low barrier, medium barrier and high barrier components. The pump pulse energy was 4 pJ and the reverse bias was 3 V. The maximum level of absorption bleaching is approximately the same for all components, however the recovery of the medium barrier component is slower than for the low and high barrier component.

6.4 Sweep-out dynamics for different heterostructures

In Chapter 3, three different heterostructure were presented, having either low, medium or high barriers. The low and medium barrier samples have 10 quantum wells, while the high barrier sample has 5 quantum wells. Figure 6.12 shows a pump-probe measurement of the absorption bleaching and recovery for components from the three wafers. The component lengths were the same, namely 250 μm. The reverse bias applied to the components were in all cases 3 V and the pump energy was 4 pJ. The absorption bleaching is for all components approximately equal, varying from 10 dB to approximately 12 dB. This ensures that the recovery dynamics can be compared between the different components. The recovery dynamics of the low barrier sample and high barrier sample are approximately the same. In both cases, the 20 GHz oscillation component on the recovery is observed. The medium barrier sample does not show, compared to the two others, a fast initial decay of the absorption bleaching. However, the component "catches up" at 200 ps. The 20 GHz oscillations are not observed on the absorption recovery of this component.

The only difference between the low barrier sample and the medium barrier sample is the barrier heights. The longer recovery time of the medium barrier sample indicate that the well depth is important. The absorption recovery of the low barrier component and the high barrier component are not expected to be equal, since the escape from the quantum wells of the high barrier sample should be slower. However, the higher escape times in the high barrier sample might be compensated by a lower recapture rate due to the fewer quantum wells. This explanation is very simplified and a more detailed discussion can only be reached from simulations of the various processes contributing to the absorption bleaching and recovery, or measurements on a range of devices with varying designs.

It can, however, be concluded, that from the three wafers, the low barrier, 10 quantum well and the high barrier, 5 quantum well components are best for all-optical signal processing.

6.5 Measurement of the refractive index dynamics

6.5.1 General trends

Figure 6.13 shows the pump induced probe phase change for 0, 1, 3, 5 and 10 V of reverse bias, on a long time scale. The pump pulse energy is 3 pJ. The curves are measured simultaneously with the transmission change curves shown in Figure 6.6, using the heterodyne pump-probe technique. The refractive index change shown in the graph is the modal refractive index change, calculated using equation (5.4) on page 42.

Figure 6.13 focuses on the refractive index dynamics on a long time scale compared to the temporal pulse width. Therefore, the decrease of the refractive index during the pump and probe pulse overlap can not be resolved, but will be looked at in section 6.5.2. Note, that the full excursion of the refractive index change during the pump and probe pulse overlap is not shown in Figure 6.13.

After the pump pulse, the refractive index can either decrease or increase depending on the reverse bias. For biases below 3 V the refractive index is decreased for all time delays. For 10 V of reverse bias the refractive index is increased for all time delays. For biases in-between, both a decrease and an increase is observed as function of time.

As for the transmission change measurements, the dynamics of the refractive index change can also be described by two time-domains, a fast recovery within the first 10–30 ps and a slow recovery, lasting on the order of hundred picoseconds. Actual time constants are however difficult to extract due to the particular shape of the curves.

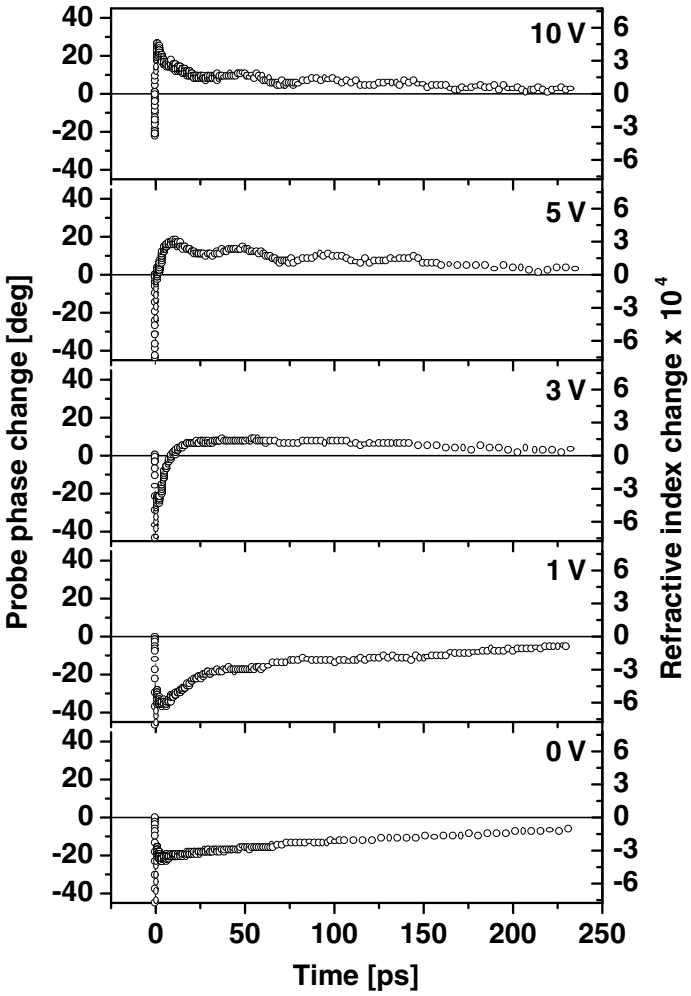

Figure 6.13: Measured probe phase change and refractive index change induced optically by the pump for 0 V, 1 V, 3 V, 5 V, and 10 V on a long time scale. The pump pulse energy is 3 pJ. The data have been cut to fit the frame. The data are shown with higher temporal resolution in the -0.5–0.8 ps range in Figure 6.17 (page 101). The refractive index change shows, as did the absorption recovery, a fast recovery within the first 10–30 ps. This is followed by slow recovery on the order of 100 ps. The sign of the refractive index change depends both on the reverse bias and on the time delay.

6.5.2 Physics of the refractive index dynamics

Compared to the thorough investigation of the refractive index dynamics in waveguide semiconductor optical amplifiers, there are, to the author's knowledge, no measurements reported on the time-resolved refractive index dynamics in saturable absorbers.

In semiconductor optical amplifiers the refractive index change, induced by an optical pump, changes sign depending on the operation conditions. When operated in the gain regime, the carrier density reduction, by stimulated emission, increases the refractive index after the thermalization of the carrier distributions. In the absorption regime the carrier generation, by absorption, decreases the refractive index. In both cases the refractive index change induced by the carrier density change recovers with the carrier injection or recombination time [49].

The saturable absorber is, no matter the magnitude of the reverse bias, operated in the absorption domain. However, from Figure 6.13 it is observed that the refractive index change can change sign, depending on the reverse bias. The explanation for the observed refractive index dynamics is found from a combination of band filling and field screening. Both these effects alter the absorption edge of the electroabsorber and thereby the refractive index.

Field screening contribution to the refractive index change

Figure 6.14 shows a schematic illustration of the coupling between the absorption change and the refractive index change for both band filling and field screening [66]. The Kramers-Kroenig transformation couples the absorption domain and the refractive index domain. The field screening blue-shifts the absorption edge. Depending on the wavelength at which the refractive index is probed, the blue-shift can either increase or decrease the refractive index. In this simple description of the field screening, the reverse bias can be substituted for the wavelength. By this is meant, that changing the wavelength with respect to the absorption edge is the same as shifting the absorption edge with respect to the wavelength. Therefore, the sign of the refractive index change induced by field screening depends on the reverse bias. The measured field-induced refractive index change was discussed in Chapter 5 with respect to chirp generation when electrically modulating the absorption.

In Figure 6.15, the measured phase and refractive index transfer curve as function of bias is shown. The curve is the same as the one shown in Figure 5.15 for the wavelength of 1535 nm. The curve is separated in two regimes, "a" and "b". In region "a", a reduction of the field, $\Delta F < 0$, results in an increase of the refractive index, $\Delta n > 0$. In region "b" a reduction of the field, $\Delta F < 0$, results in a decrease of the refractive index, $\Delta n < 0$. For time delays longer than $\sim$ 20 ps the index change can be well explained by

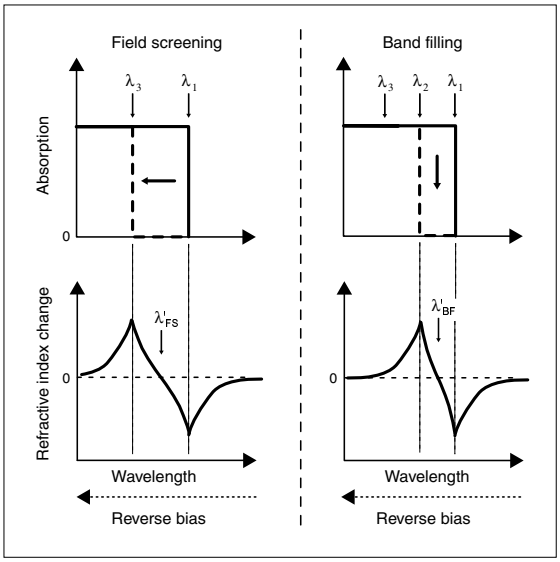

Figure 6.14: Schematic illustration of the refractive index change accompanying field screening (left column) and band filling (right column) . The field screening is assumed to blue-shift the absorption edge from λ_1 to λ_3 and thereby changes the refractive index. Depending on the probe wavelength, the refractive index change can be either positive or negative. The band filling is assumed to reduce the absorption between λ_1 and λ_2. Also in that case the refractive index change depends on the wavelength. In this simple model, an increase of the wavelength corresponds to a decrease of the reverse bias. This is because an increase of the reverse bias shifts the whole absorption edge with respect to the wavelength, without distorting the edge. For the specific wavelengths λ'_{FS} and λ'_{BF} the refractive index change is zero even though the absorption edge has been altered by field screening or band filling, respectively. Increasing the wavelength (or decreasing the reverse bias) with respect to λ' results in a refractive index change becoming negative while decreasing the wavelength (or increasing the reverse bias) results in a refractive index change becoming positive. Notice that λ'_{FS} and λ'_{BF} are not necessarily equal, due to the different processes responsible for the refractive index change. The figure is inspired by [66].

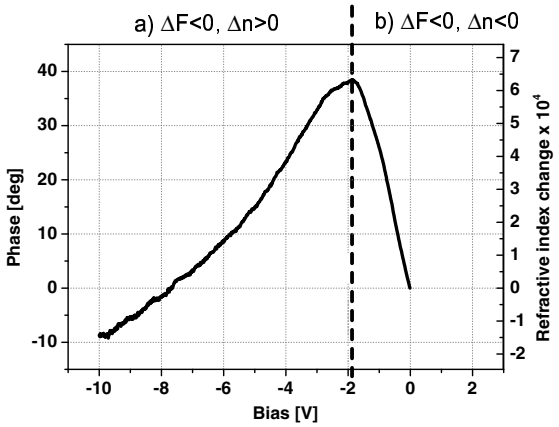

Figure 6.15: Measured phase and refractive index change as function of the bias applied to the electroabsorber. The probe wavelength is 1535 nm. When the saturable absorber is operated in the region "a)" a field screening ($\Delta F < 0$) results in a increased refractive index, while operation in the "b)" region a field screening results in a reduced refractive index. The change of sign of the refractive index change at ∼2 V of reverse bias is in good agreement with the measured optically induced refractive index change at long delays.

the field screening. For 0 and 1 V of reverse bias, the refractive index change is negative as expected from Figure 6.15, where 0 V and 1 V are in the "b"-region. At 3 V of reverse bias and beyond, the component is operated in the "a"-region and the refractive index change is positive. The change of sign of the refractive index component between 1 V and 3 V fits well with the transition between the "a" and "b"-region being at ∼2 V of reverse bias. It should be noted that the refractive index transfer curve was measured at 1535 nm while the pump-probe measurements were performed at 1520 nm. The peak of the refractive index change, being at ∼2 V of reverse bias at 1535 nm is shifted to lower reverse bias at 1520 nm, following the discussion from Chapter 3. However, the shift is, by looking at Figure 5.15, expected to be small. From the observations and this simple description the change of sign of the refractive index change for long delays can be understood. It can also be concluded that the absorption bleaching at long delay is mainly induced by field screening. This is in accordance with the fact that as the carriers have escaped from the quantum wells, they can only contribute to the absorption change trough field screening.

Band filling contribution to the refractive index change

The photogenerated carriers in the active region affect the shape of the absorption edge. A simplified illustration is shown in Figure 6.14. The carriers generated bleach the absorption at the low energy end of the absorption spectrum. Here, the reduction is described by a simple rectangular reduction of the absorption. The refractive index change accompanying the absorption change is also schematically shown. The overall shape is the same as the refractive index change accompanying the field screening. This is expected, since a bleaching of the absorption from λ_1 and λ_3 due to carrier generation would be indistinguishable from a blue-shift of the absorption edge from λ_1 to λ_3, due to field screening. Therefore, in this simplified model, the sign of the refractive index change due to band filling will also depend on the wavelength, or the reverse bias, in a similar fashion as the field screening induce refractive index change.

The spectral width of the absorption change due to the band filling or the field screening is not necessarily equal. It is here arbitrarily chosen to be smaller in the case of band filling than in the case of field screening. The effect of this on the refractive index change is that the bias/wavelength at which the change of sign appears (λ' in Figure 6.14), depends on the physical process causing the absorption change.

Figure 6.16 shows the measurements from Figure 6.13 on a 26 ps time scale. Immediately after the pump and probe pulse overlap the refractive index is changed. The refractive index change is primarily caused by the band filling, due the fact that field screening is delayed by the escape time of the carriers from the quantum wells. The initial reduction of the refractive index fits well with the simple model presented. Assume that the pump and probe wavelength are below the absorption edge ($\lambda > \lambda_1$) in Figure 6.14, for 0 V of bias. By optical saturation of the absorption, the refractive index change will be negative. When the reverse bias is increased, the refractive index, induced by the band filling, will decrease more than at 0 V. This is observed when going from 0 V to 2 V of reverse bias in Figure 6.16. As the reverse bias is increased further, the negative refractive index change is reduced again. At $\sim$5 V the index change due to band filling is approximately zero. This corresponds to a reverse bias at which the wavelength of the probe is at λ'_{BF} with respect to the bandedge. A further increase of the reverse bias will, according to the model, result in a positive refractive index change, which is also observed at 10 V of reverse bias. This simplified description accounts qualitatively for the dynamics shortly after the pump pulse.

The refractive index dynamics for the 3 V reverse bias curve in Figure 6.16 is particularly illustrative of the band filling and field screening contributions to the dynamics. Initially, the band filling reduces the refractive index. Ascribing band filling as the only contribution to the refractive index dynamics, the recovery would not "overshoot" at 10 ps, but would simply recover with

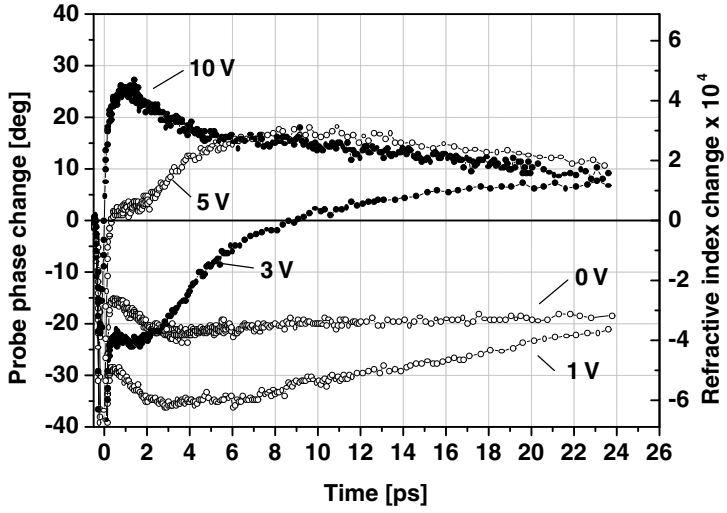

Figure 6.16: Measured pump induced probe phase-change and material refractive index change for 0 V, 1 V, 3 V, 5 V and 10 V reverse bias. The pump input power is 3 pJ. See text for discussion.

the carrier sweep-out time. By adding the field screening contribution to the refractive index, the positive refractive index excursion at longer delays can be understood. In the intermediate regime a superposition of the two oppositely signed contributions to the refractive index exists.

A thorough discussion of both the size of the refractive index change due to the band filling and the field screening demands a detailed knowledge on the actual spectral shape of the absorption edge. It is clear that a "box" presentation of the absorption edge and the band filling and field screening effects is too simple when discussing the quantitative nature of the refractive index change. First of all the absorption edge is not abrupt, as also measured in chapter 3, secondly the field screening does not only blue-shift the absorption edge but increases also the absorption for higher energies due to the increased electron and hole wavefunction overlap. Just after the pump pulse the hot carrier distribution contribution to the reduction of the absorption is not well described by a "box". The Fermi-distribution of the thermalized carriers will together with the real absorption edge also differ from the "box"-representation. It is therefore clear that only a model incorporating the actual shape of the absorption spectrum as function of the field and the carrier density and distribution, can provide a full understanding of the size and the precise dynamics of the time evolution of the refractive index after an optical excitation.

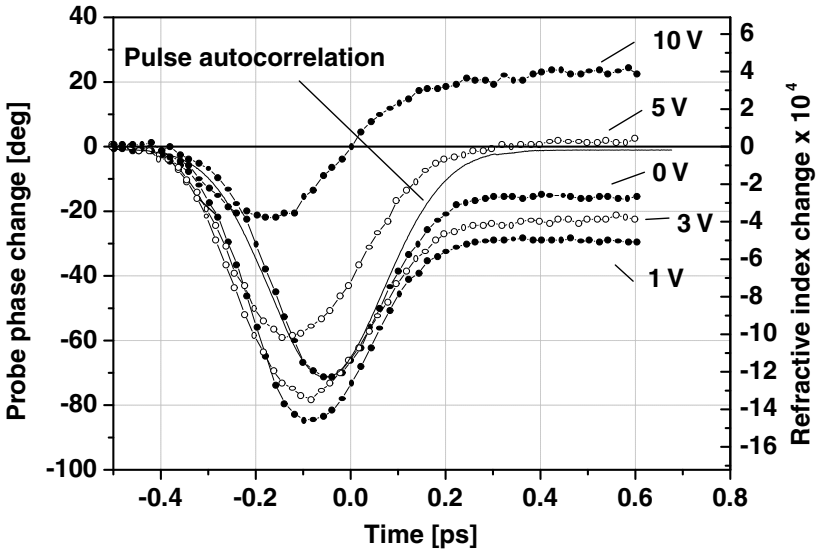

Figure 6.17: Pump induced probe phase change and refractive index change on a 1 ps time scale. The reverse bias applied to the component is 0, 1, 3, 5 and 10 V and the pump pulse energy is 3 pJ. The refractive index change during the pump and probe pulse overlap follows the pulse autocorrelation and is explained by the optical Stark effect.

Refractive index change during the pump and probe pulse overlap

Finally, the focus is put on the special case of refractive index dynamics during the pump and probe pulse overlap. In Figure 6.17 the phase and refractive index change during the pump and probe overlap is well resolved. The same instantaneous decrease of the refractive index is observed in semiconductor optical amplifiers and is attributed to the optical Stark effect [93]. The quadratic optical Stark effect gives a reduction of the refractive index proportional to the intensity. It will therefore appear in the pump-probe measurement as a reduction of the refractive index following the shape of the cross-correlation between the pump and the probe. The shape of the measured laser pulse autocorrelation is superposed to the refractive index dynamics at 0 V. The autocorrelation is shifted by approximately 50 fs to fit the peak of the index response (the temporal shift is not well understood). The autocorrelation is seen to fit well with the instantaneous response of the refractive index. For increasing reverse biases, it

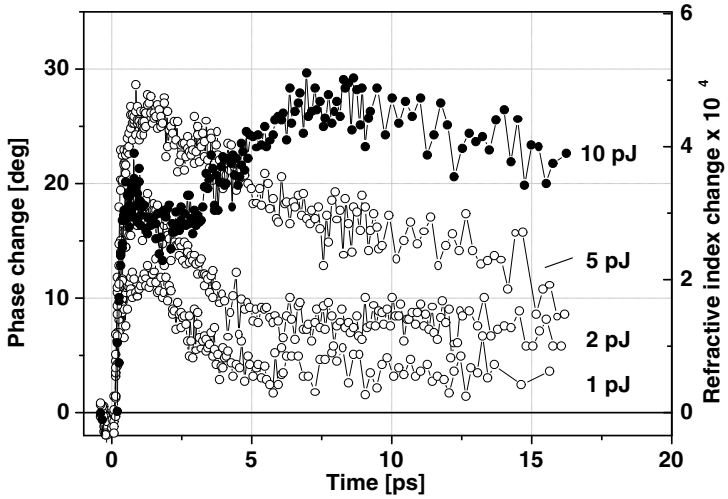

Figure 6.18: Pump induced probe phase change and refractive index change for 1 pJ, 2 pJ, 5 pJ and 10 pJ of pump energy. The reverse bias is 6 V. An expected increase of the refractive index change is observed for pulse energies increasing from 1 to 5 pJ. The dynamics following excitation by a 10 pJ pump pulse is not easily explained. See text for discussion.

is observed that the peak of the refractive index change moves further towards negative delays. A simple explanation is not expected, since many effects are present during the pump and probe overlap.

The large index change during the short pump pulse will induce a large chirp on the probe pulse, as mentioned previously. The reduction of the refractive index with the intensity gives a positively chirped pulse with a blue-shifted leading edge and a red-shifted trailing edge. The maximum instantaneous frequency excursion, calculated from a 200 fs pulse experiencing a maximum of 80 deg of phase change during the pulse, is ∼10 nm. This should contribute significantly to the absorption dynamics during the pump and probe pulse overlap, as discussed previously.

6.5.3 Pump pulse energy dependence of the refractive index dynamics

It was seen previously that the absorption bleaching can be increased by increasing the pump pulse energy. Figure 6.18 shows the refractive index dynamics of the saturable absorber for four different pump pulse energies, ranging from 1 pJ to 10 pJ. The component was reverse biased with 6 V. It is observed

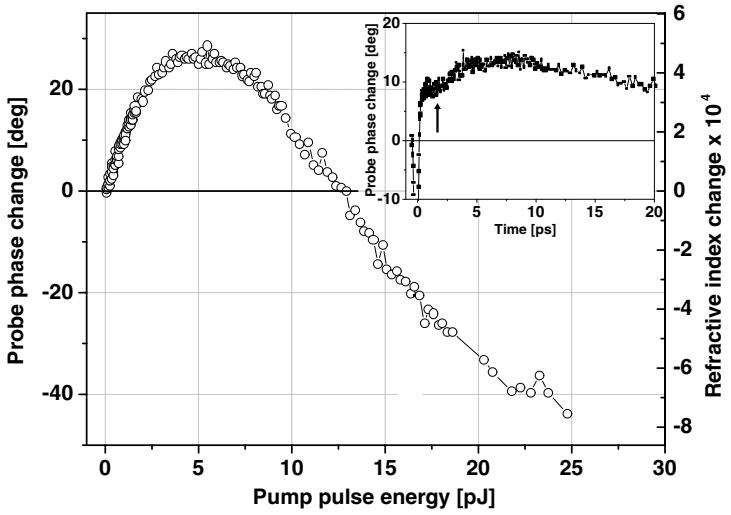

Figure 6.19: Measured refractive index change as function of the pump pulse energy. The refractive index change is measured 2 ps after the pump pulse arrival, as indicated in the inset. The component is reverse biased with 6 V. The initial increase of the refractive index change, also observed in Figure 6.18 is well resolved together with the peaking and following decrease for increasing pump pulse energy. The linear decrease of the refractive index change with pulse energy for high pulse energies indicates that another process than the band filling contributes to the refractive index change, since the absorption is saturated at the same pulse energies (see Figure 6.11 page 91).

that the refractive index change increases with pump pulse energy from 1 pJ to 5 pJ. This is expected from the fact that as the band filling increases the absorption change also increases, resulting in a higher refractive index change. The refractive index change following the 10 pJ pump pulse energy shows initially a reduced refractive index change compared to the "5 pJ"-curve. After the initial unexpected dynamics, the refractive index change increases again and becomes, as expected, larger than the "5 pJ"-curve. The reduction of the refractive index change can partially be explained by a larger absorption bleaching effectively moving the absorption edge to higher energies. From Figure 6.14 an increase of the width of the absorption bleaching will, for operation at λ_3 decrease the refractive index change. Figure 6.19 shows the measured refractive index change at 2 ps of delay as function of the pump pulse energy. The arrow on the inset indicates the 2 ps delay. It is clearly observed that initially the refractive index change increases with the pulse energy. However, at $\sim$5 pJ the refractive index change peaks and starts to decrease again. At

12.5 pJ the refractive index change crosses 0 and becomes negative. The same trend is also observed for longer delays (not shown). The saturation of the absorption bleaching as function of the pulse energy observed in Figure 6.9 is not reflected in a saturated refractive index change. Instead an almost linear decrease in the refractive index is observed from 10 pJ to 20 pJ. It is therefore not likely that an increased carrier density is the only reason for the refractive index dynamics for pump pulses with energies higher than 10 pJ. Figure 6.10 shows that two-photon absorption is important for these pulse energies and might contribute to the refractive index dynamics either directly or through carrier heating.

6.5.4 Optimum operation points for all-optical wavelength conversion in saturable absorbers

In chapter 3 the electroabsorber was discussed with respect to optimum operation conditions when applied for intensity modulation by electrically changing the absorption. It was shown that if the reverse bias is high enough and the wavelength close to the absorption edge, the refractive index accompanying an increase in the transmission is also increased. This results in the negative pulse chirp advantageous for compensating the pulse broadening induced by the fiber dispersion. According to the measurements presented in this chapter a saturable absorber also shows this capability. For a reverse bias equal to or above 5 V, the refractive index is also increased as the transmission through saturable absorber increases (for a 3 pJ pump pulse energy). However, below 3 V the refractive index decreases when the transmission increases. Operation conditions for the saturable absorber as a wavelength converter is therefore not only determined by the absorption dynamics, since the transmission distance also depends on the chirp on the wavelength converted signal. All-optical wavelength conversion in Mach-Zehnder semiconductor structures with semiconductor optical amplifiers as the phase-shifters has been investigated with respect to the chirping characteristics [97]. It was shown, that the absolute magnitude of the small-signal α_H-parameter measured by all-optical modulation of the Mach-Zehnder interferometer was 2 ± 0.5. The result was measured using the main mode-to-side mode measurement technique not providing the sign of the α_H-parameter [98]. However, in the non-inverting scheme used by [97] it is known that the α_H-parameter is negative [99]. Other operation conditions of the Mach-Zehnder showed an α_H-parameter equal to 0. It is well known that depending on the phase delays in the two arms of the Mach-Zehnder the α_H-parameter can be either negative, zero or positive [16]. The absorption change ($\Delta\alpha$) and refractive index change (Δn) measurements presented in this chapter do not directly provide the α_H-parameter of the saturable absorber. The best illustration of this is the pump-probe scans for 3 V of reverse bias

shown in Figure 6.6 and Figure 6.13. Here, the α_H-parameter calculated from the measured $\Delta\alpha$ and Δn using equation (A.5) (Appendix A) is initially positive while for longer delays it becomes negative. Hence, the α_H-parameter from this calculation does not directly provide any information on the chirp on the wavelength converted pulse. However, the sign of the α_H-parameter can, for some special cases, be determined from the pump-probe measurements. If the reverse bias is increased, the α_H-parameter representing the field screening contribution to the absorption and refractive index dynamics changes sign between 1 and 3 V of reverse bias. Secondly, the α_H-parameter representing the absorption and refractive index dynamics for the band filling, changes sign at 5 V. Therefore it can be concluded, that by applying enough reverse bias (5 V for 3 pJ of pump pulse energy) the wavelength converted pulses will be negatively chirped. This shows that the simple saturable absorber can indeed compete with the much more advanced Mach-Zehnder modulators typically used for wavelength conversion.

6.6 Summary

The large-signal response of semiconductor saturable absorbers has been characterized in the temporal domain both with respect to the transmission change and the refractive index change. The shape of the absorption bleaching is explained by a combination of spectral hole burning, carrier heating/cooling and field screening, as it has previously been reported in the literature. The absorption bleaching depends both on the reverse bias and on the pump power and is shown to be well described by a double exponential recovery for the high barrier component. For 3 pJ of pump pulse energy, the short time constant decreases from $\sim$ 200 ps to $\sim$2.5 ps for a reverse bias going from 1 V to 10 V. The long time constant is less dependent on the bias and is of the order of 100 ps. The physical reason for the double exponential recovery is not well understood, but includes carrier escape from the quantum wells, field screening, carrier pile-up and possibly carrier recapture. By increasing the pump pulse energy, the magnitude of the absorption bleaching increases. Pump-probe traces for pump pulse energies up to 10 pJ showed no increase in the fast recovery time component. However, the long recovery tail is increased by $\sim$1 dB when increasing the pump pulse energy from 5 pJ to 10 pJ. Below 5 pJ, no pulse energy dependence of the long recovery tail is observed.

A comparison between three components with different barrier height and number of quantum wells was reported. The high barrier, five quantum well structure and the low barrier, ten quantum well structure showed similar recovery times. The medium barrier, ten quantum well component showed a longer recovery time. An explanation based on a combination of carrier escape time and recapture is proposed.

For 10.6 pJ of pump pulse energy and 6 V of reverse bias applied to the high barrier saturable absorber a 10 ps switching window with 9.6 dB of extinction ratio is realized. This shows that the saturable absorbers made in the SCOOP-programme can indeed be used for fast switching. The long recovery tail, on the order of 100 ps might limit the base-rate. However, successful wavelength conversion at 40 Gb/s has been realized using these components. This shows that the long recovery tail might not be a limitation to the component speed.

Pump-probe measurements showed that the optically induced refractive index change depends on the pump pulse energy and the reverse bias applied to the saturable absorber. The optical Stark effect explains the instantaneous decrease of the refractive index during the pump and probe overlap. Band filling effects explain the dynamics of the refractive index during the first few picoseconds. For longer delays the field screening is shown to account well for the measured refractive index dynamics. Using a simple description, the observed sign of the refractive index change can be explained qualitatively. For the specific component investigated and for a 3 pJ pump pulse, the refractive index change, attributed to the band filling, goes from negative to positive when the reverse bias is increased past 5 V. The refractive index change, due to the field screening is seen to go from negative to positive between 1 V and 3 V. This agrees well with the measurements reported in Chapter 5 on the refractive index changes following a reverse bias change.

For 6 V of reverse bias, the refractive index initially increases with the pump pulse energy. However, for pump energies higher than 5 pJ, the refractive index change 2 ps after the pump pulse is reduced with pump power. Continuing to increase the pump energy results in a reduced refractive index. The dynamics is not well understood, but two-photon absorption is shown to be important at these pulse energies and is likely to contribute to the dynamics.

It is argued that for the right bias and pump pulse energy, it is possible to wavelength convert to a negatively chirped pulse. This shows that the saturable absorber can indeed compete with other more complex components, such as the monolithic Mach-Zehnder semiconductor wavelength converter.

Chapter 7

Conclusion

The absorption and refractive index dynamics in InGaAsP waveguide semiconductor electroabsorbers with a MQW active region have been investigated experimentally. The components were made within the SCOOP-programme in collaboration with the company GiGA-An Intel Company. The experimental characterization included basic characterization such as insertion loss, coupling loss on components with different designs. Hereafter, the characteristics of the electroabsorbers, when operated electrically as an electroabsorption modulator, have been investigated with respect to pulse chirp and extinction ratio. Finally, the fast absorption and refractive index dynamics following an optical generation of carriers in the electroabsorber has been characterized.

Coupling losses as low as 0.7 dB per faced have been measured. The waveguide losses have been found to vary from component to component. Values ranging from 5.2 dB/100-μm down to 0.6 dB/100-μm are reported and the large differences are explained by variations in the device processing. The absorption spectra of three components with different quantum well barrier heights have been measured as a function of reverse bias. However, no clear effect of the dependency of the absorption spectra on the barrier height was seen. Operation close to the absorption edge is shown to be advantageous with respect to the extinction ratio. However, the component insertion loss is also increased at this operation point. It is demonstrated that over 7 dB of static extinction ratio is possible from $\sim$1500 nm to $\sim$1575 nm, using a 4 V drive voltage. A low polarization dependent absorption is also demonstrated.

Absorption spectra, calculated by S. Højfeldt (SCOOP/COM), on a shallow well component, are compared to the measured absorption spectra. A good

correspondence is observed and it is concluded that excitonic effects are not important for this structure. The calculations also demonstrate that coupling between quantum wells is important.

A new technique is applied to investigate the ability of the optical modulators to generate pulses of good quality for optical fiber transmission. The technique is based on a heterodyne detection scheme where the amplitude and phase transfer functions of the optical modulator are measured as function of the reverse bias and wavelength. From the measured transfer curves, the full bias dependency of the α_H-parameter can easily be calculated. The technique is shown to be very effective and can easily compete with the traditional techniques reported in other literature.

From the amplitude and phase transfer functions, the response of the EAM to a modulation of the reverse bias can be calculated. An example of a fast modulation is a 10 Gb/s NRZ signal measured from a test-set. The calculations provide both the pulse intensity waveform and the pulse chirp and optimum conditions of operation with respect to extinction ratio, insertion loss and chirp. It is concluded, that operation close to the absorption edge is not only advantageous with respect to high extinction ratio, but also with respect to generating low or negatively chirped pulses. Increasing the offset reverse bias also decreases the chirp for a given drive voltage. However, both the operation close to the absorption edge and the increased reverse bias come at the expense of an increased insertion loss. It is demonstrated that describing EAMs with effective α_H-parameters is difficult because of the strong dependence of the α_H-parameter on the reverse bias. A comparison between a component with 10 shallow wells and a component with 5 deep quantum wells concludes, that the first mentioned is better in terms of extinction ratio and chirp.

From the absorption spectra calculated by S. Højfeldt (SCOOP/COM) the refractive index change is calculated as a function of the reverse bias and wavelength, using the Kramers-Kroenig transformation. The results support the measurements in concluding that the EAMs can generate pulses with high extinction ratio and low or negative chirp, given the right wavelength and reverse bias.

The large signal absorption- and refractive index dynamics in electroabsorbers, operated as saturable absorbers have been investigated. For these investigations a heterodyne pump-probe set-up has been used. The temporal resolution of the measurements were limited by the pump and probe pulse intensity-FWHM equal to 200 fs. The measurements show, that the absorption bleaching and following recovery depend strongly on the input pulse energy and the reverse bias applied to the saturable absorber. For a pulse energy of 3 pJ at the facet, a clear signature of spectral hole burning is observed above 2 V

at 1520 nm, close to the absorption edge at 0 V. Below 2 V, the absorption is observed to increase during the pump and probe temporal overlap. It is argued, that the explanation for the increase in absorption includes a combination of two-photon absorption, the coherent artifact and the spectral artifact.

The absorption bleaching peaks a few picoseconds after the pump and probe pulse overlap. This continued absorption bleaching corresponds well to reported carrier heating and cooling effects. Simulations performed within the SCOOP-programme by S. Højfeldt on similar structures also indicate that field screening by carriers escaped from the quantum wells can result in a delayed peak in the absorption bleaching.

The absorption recovery is observed to be double exponential with two characteristic time constants. The short time constant decreases strongly with reverse bias while the long time constant is less dependent on the reverse bias. The details of the recovery dynamics are not well understood, but include electron and hole escape from the quantum wells, carrier induced field screening, carrier pile-up at the edges of the separate hetero-confinement layer and possibly recapture of carriers into the quantum wells. A 10 ps switching window with a maximum of 9.6 dB is realized using a pulse with 10.6 pJ of energy and reverse biasing the saturable absorber with 6 V. This shows, that saturable absorbers manufactured within the SCOOP-programme can indeed generate very short switching windows for high bit-rate OTDM signal demultiplexing.

Three components with different barrier heights and number of quantum wells are investigated with respect to the absorption recovery. A high barrier, five quantum well saturable absorber shows similar recovery times as a low barrier, ten quantum well device. A medium barrier component with ten quantum wells is shown to have a slower recovery than the low and high barrier components. A proposed explanation based on the carrier escape from the quantum wells and carrier recapture seems reasonable.

The time-resolved refractive index dynamics in the saturable, absorber accompanying optical carrier generation, is also investigated. During the pump and probe pulse overlap, the refractive index is decreased, explained by the optical Stark effect. After the pump and probe pulse overlap, the refractive index dynamics is explained by a combination of band filling and field screening. The band filling is shown to dominate at short delays, while the field screening dominates for longer delays. A simple model explains the observed change of sign of the refractive index change with reverse bias.

The time-resolved refractive index dynamics as a function of pump pulse energy is not well understood. For low pulse energies the refractive index change is proportional to the pulse energy. However, for increased pulse energies the dynamics is nonlinear. For 6 V of reverse bias, the refractive index at 2 ps delay increases initially with pump energy, explained by an increased band filling.

As the pump energy is increased further, the refractive index change decreases again and eventually becomes negative. No saturation of the decrease of the refractive index for high pump energies is observed, even though the absorption change is strongly saturated. Two-photon absorption is shown to be important at these pulse energies and is likely to contribute to the dynamics.

From the refractive index measurements it is demonstrated that wavelength conversion to a negatively chirped pulse is possible, given the right reverse bias and pump energy. This shows, that the electroabsorber can in the all-optical operation scheme, generate negatively chirped pulses, advantageous for optical fiber transmission.

The results presented in this thesis, together with the results reported in other literature show that the electroabsorber is a simple and compact multi-purpose component. The stand-alone characterization of the components reported in this thesis only hints the performance of the electroabsorbers in a full telecommunication system. It would therefore be interesting to investigate how the chirp acquired in wavelength conversion affects the propagation distance. Pump-probe measurements on the saturable absorber at different wavelengths is also of interest. Direct excitation of states energetically above the quantum well could provide more information on the band filling and the field screening contribution to the absorption dynamics. The polarization sensitivity of the electroabsorbers, operated as EAMs or saturable absorbers, is also of interest when applying these components for inline signal processing. The characterization of the polarization dependence of the absorption and phase dynamics in the electroabsorbers can easily be investigated using the heterodyne measurement setup.

Hopefully, some of these investigations will be continued within the SCOOP-programme and thereby provide more insight into the physics of electroabsorbers and the application possibilities of these components within all-optical signal processing.

Appendix A

Different expressions for the α_H-parameter

This appendix shortly runs through the calculations resulting in the expression of the α_H-parameter as function of the refractive index change and the absorption, or the phase change and intensity change. The main part of the derivations can also be found in Chapter 2 in [59].

The α_H-parameter is by definition given as

$$\alpha_H = \frac{\Delta\chi_R}{\Delta\chi_I} \tag{A.1}$$

where $\Delta\chi_R$ and $\Delta\chi_I$ are the change in the real and imaginary part of the medium susceptibility following an external perturbation, respectively [60]. To express the α_H-parameter as function of the refractive index (n) and material absorption (α) the following definitions are used

$$n = \sqrt{\epsilon} = \sqrt{\epsilon_b + \chi_R} \tag{A.2}$$

$$\alpha = \frac{2\pi\nu_0}{cn_b}\chi_I \tag{A.3}$$

where ϵ_b is the background dielectric constant, ν_0 is the optical carrier frequency, c the speed of light in vacuum and ν_b is the background refractive index. Since the refractive index change induced by the voltage change is small compared to the background refractive index the following approximation is valid

$$\Delta n \cong \frac{\Delta\chi_R}{2n_b} \tag{A.4}$$

By substitution of equation (A.3) and (A.4) into equation (A.1) the α_H-parameter can be expressed as function of the absorption change (equal to the material absorption change) and the refractive index change

$$\alpha_H = \frac{4\pi\nu_0}{c}\frac{\Delta n}{\Delta\alpha} \tag{A.5}$$

The α_H-parameter can also be expressed directly from the transmission (ΔI) and phase change ($\Delta\phi$) experienced by the optical field travelling through the material. From equation (A.4) the change in the real part of the susceptibility expressed as function of the phase change

$$\Delta\chi_R = \frac{2cn_b\Delta\phi}{2\pi\nu_0 l} \tag{A.6}$$

with the phase change being defined as

$$\Delta\phi(t) = \frac{2\pi\nu_0 l}{c}\Delta n(t) \tag{A.7}$$

where l is the propagation length. Using the following equality for the intensity transmission change and the absorption change

$$I = I_0 e^{-\alpha l} \rightarrow \Delta\alpha = -\Delta(\ln(I/I_0))/l = -\Delta(\ln(I))/l \tag{A.8}$$

where I_0 is the input intensity and I_0 is the output intensity after transmission through the material, the imaginary part of the susceptibility can be written as

$$\Delta\chi_I = -\frac{cn_b\Delta(\ln(I/I_0))}{2\pi\nu_0 l} \tag{A.9}$$

Finally, the α_H-parameter can be expressed from equation (A.1), (A.6) and (A.9) as

$$\alpha_H = -\frac{2\Delta\phi}{\Delta(\ln(I))} \tag{A.10}$$

Bibliography

[1] J. Mork, K. Yvind, L. Oxenlowe, P. Skovgaard, F. Romstad, S. Bischoff, S. Hojfeldt, A. Tersigni, L. Christiansen, A. Nik, F. Ohman, J. Hvam, J. Hanberg, K. Hoppe, and M. Lobel, "SCOOP-semiconductor components for optical signal processing," DOPS-NYT, vol. 16, no. 2, pp. 25–9, 2001.

[2] T. Otani, T. Miyzaki, and S. Yamamoto, "40 Gbit/s signal transmission using optical 3R regenerator based on electroabsorption modulators," Optical Fiber Communication Conference, 2000, vol. 3, pp. 226–228, 2000.

[3] L. K. Oxenløwe, E. Hilliger, A. Tersigni, A. M. Nik, S. Højfeldt, F. Romstad, K. Yvind, P. M. W. Skovgaard, K. Hoppe, and J. Hanberg, "All-optical Demultiplexing and Wavelength Conversion in an Electroabsorption Modulator," Proceedings of ECOC 2001, Amsterdam, The Netherlands, vol. paper Th.B.2.5, 2001.

[4] B. Mikkelsen, G. Raybon, and R.-J. Essiambre, "160 Gb/s TDM Transmission Systems," Proceedings of ECOC 2001, Amsterdam, The Netherlands, vol. paper 6.1.1, 2000.

[5] N. Peyghambarian, S. Koch, and A. Mysyrowicz, Introduction to semiconductor optics. Englewood Cliffs, New Jersey 07632: Prentice Hall, 2 ed., 1993.

[6] F. Devaux, S. Chelles, A. Ougazzaden, A. Mircea, and J. Harmand, "Electroabsorption modulators for high-bit-rate optical communications: a comparison of strained InGaAs/InAIAs and InGaAsP/InGaAsP MQW," Semicond. Sci. Technol., vol. 10, no. 7, pp. 887–901, 1995.

[7] B. Gomatam and N. Anderson, "Electroabsorption Enhancement in Tensile Strained Quantum Wells Via Absorption Edge Merging," IEEE J. Quantum Electron., vol. 28, no. 6, pp. 1496 –1507, 1992.

[8] T. Aizawa, K. Ravikumar, S. Suzaki, T. Watanabe, and R. Yamauchi, "Polarization-Independent Quantum-Confined Stark Effect in an InGaAs/InP Tensile-Strained Quantum Well," IEEE J. Quantum Electron., vol. 30, no. 2, pp. 585 –592, 1994.

[9] S. Chelles, R. Ferreira, and P. Voisin, "On the design of polarization-insensitive optoelectronic devices," Semicond. Sci. Technol., vol. 10, no. 1, pp. 105–9, 1995.

[10] D. Mathoorasing, C. Kazmierski, M. Blez, Y. Sorel, J. Kerdiles, M. Henry, and C. Thebault, "109km transmission experiment at 20 Gbit/s with directly modulated DFB V-on-U groove (VUG) laser," Electron. Lett., vol. 30, no. 6, pp. 507–508, 1994.

[11] J. White, H. Kim, C. Blaauw, and A. Feceks, "20 Gbit/s directly modulated 1310 nm ridge laser," OFC 2001. Optical Fiber Communication Conference and Exhibit. Technical Digest Postconference Edition (IEEE Cat. 01CH37171), pp. WDD71–1–3 vol.3, 2001.

[12] E. Wooten, K. Kissa, A. Yi-Yan, E. Murphy, D. Lafaw, P. Hallemeier, D. Maack, D. Attanasio, D. Fritz, G. McBrien, and D. Bossi, "A review of lithium niobate modulators for fiber-optic communications systems," IEEE J. Sel. Top. Quantum Electron., vol. 6, no. 1, pp. 69–82, 2000.

[13] J. R. Burie, F. Dumont, O. le Gouezigou, S. Lamy, D. Cornec, and P. André, "50 Gb/s capability of a new zero loss integrated SOA/EA modulator," Proceedings of ECOC 2000, vol. paper 1.3.3, 2000.

[14] H. Kawanishi, Y. Yamauchi, N. Mineo, Y. Shibuya, H. Murai, K. Yamada, and H. Wada, "Over-40-GHz modulation bandwidth of EAM-integrated DFB laser modules," Optical Fiber Communication Conference and Exhibit, 2001. OFC 2001, vol. 1, 17-22 March 2001.

[15] O. Mitomi, S. Nojima, I. Kotaka, K. Wakita, K. Kawano, and M. Naganuma, "Chirping characteristic and frequency response of MQW optical intensity modulator," J. Lightwave Technol., vol. 10, no. 1, pp. 71 –77, 1992.

[16] F. Koyama and K. Oga, "Frequency chirping in external modulators," J. Lightwave Technol., vol. 6, no. 1, pp. 87 –93, 1988.

[17] J. C. Cartledge and B. Christensen, "Optimum Operating Points for Electroabsorption Modulators in 10 Gb/S Transmission Systems Using Nondispersion Shifted Fiber," IEEE J. Lightwave Technol., vol. 16, no. 3, pp. 349–357, 1998.

[18] A. Gnauck, S. Korotky, J. Veselka, J. Nagel, C. Kemmerer, W. Minford, and D. Moser, "Dispersion Penalty Reduction Using an Optical Modulator with Adjustable Chirp," IEEE J. Photon. Technol. Lett., vol. 3, no. 10, pp. 916 –918, 1991.

[19] K. Wakita, K. Yoshino, A. Hirano, S. Kondo, and Y. Noguchi, "4-5 ps optical pulse generation with 40 GHz train from low driving-voltage modulator modules," Conference Proceedings. 1998 International Conference on Indium Phosphide and Related Materials (Cat. No.98CH36129), pp. 679–82, 1998.

[20] D. Moodie, A. Ellis, A. Thurlow, M. Harlow, I. Lealman, S. Perrin, L. Rivers, and M. Robertson, "Multiquantum well electroabsorption modulators for 80 Gbit/s OTDM systems," Electron. Lett., vol. 31, no. 16, pp. 1370 –1371, 1995.

[21] M. Guy, V. Chernikov, J. Taylor, Moodie, and R. Kashyap, "200 fs soliton pulse generation at 10 GHz through nonlinear compression of transform-limited pulses from an electroabsorption modulator," Electron. Lett., vol. 31, no. 9, pp. 740 –741, 1995.

[22] R. Ludwig and A. Ehrhardt, "Turn-key-ready wavelength-, repetition rate- and pulsewidth-tunable femtosecond hybrid modelocked semiconductor laser," Electron. Lett., vol. 31, no. 14, pp. 1165 –1167, 1995.

[23] I. Ogura, H. Kurita, T. Sasaki, and H. Yokoyama, "Precise operation-frequency control of monolithic mode-locked laser diodes for high-speed optical communication and all-optical signal processing," Optical and Quantum Electronics, vol. 33, no. 7, 2001.

[24] E. Avrutin, J. Marsh, and E. Portnoi, "Monolithic and multi-gigahertz mode-locked semiconductor lasers: constructions, experiments, models and applications," Optoelectronics, IEE Proceedings-, vol. 147, no. 4, pp. 251 –278, 2000.

[25] G. Vareille, B. Julien, F. Pitel, and J. Marcerou, "3.65 Tbit/s (365 x 11.6 Gbit/s) transmission experiment over 6850 km using 22.2 GHz channel spacing in NRZ format," Proceedings of ECOC 2001, vol. Th.M.4., 2001.

[26] P. Le Roux, F. Boubal, E. Brandon, N. Buet, L. Darbois, V. Havard, L. Labrunie, L. Piriou, A. Tran, and J.-P. Blondel, "25 GHz spaced DWDM 160x10.66 Gbit/s (1.6 Tbit/s) unrepeatered transmission over 380 km," Proceedings of ECOC 2001, vol. Th.M.4., 2001.

[27] K. Inoue and H. Toba, "Wavelength Conversion Experiment Using Fiber Four-Wave Mixing," IEEE J. Photon. Technol. Lett., vol. 4, no. 1, pp. 69 –72, 1992.

[28] M. Tatham, G. Sherlock, and L. Westbrook, "20-Nm Optical Wavelength Conversion Using Nondegenerate Four-Wave Mixing," IEEE J. Photon. Technol. Lett., vol. 5, no. 11, pp. 1303 –1306, 1993.

[29] H. Furukawa, H. Takakura, and K. Kuroda, "A novel optical device with wide-bandwidth wavelength conversion and an optical sampling experiment at 200 Gbit/s," IEEE Transactions on Instrumentation and Measurement, vol. 50, no. 3, pp. 801–807, 2001.

[30] A. Ellis, A. Kelly, D. Nesset, D. Pitcher, D. Moodie, and R. Kashyap, "Error free 100 Gbit/s wavelength conversion using grating assisted cross-gain modulation in 2 mm long semiconductor amplifier," Electron. Lett., vol. 34, no. 20, pp. 1958 –1959, 1998.

[31] A. Kelly, I. Phillips, R. Manning, A. Ellis, D. Nesset, D. Moodie, and R. Kashyap, "80 Gbit/s all-optical regenerative wavelength conversion using semiconductor optical amplifier based interferometer," Electron. Lett., vol. 35, no. 17, pp. 1477–1478, 1999.

[32] S. Nakamura, Y. Ueno, and K. Tajima, "168-Gb/s All-Optical Wavelength Conversion with a Symmetric-Mach-Zehnder-Type Switch," IEEE J. Photon. Technol. Lett., vol. 13, no. 10, pp. 1091–3, 2001.

[33] R. Hess, M. Dulk, W. Vogt, E. Gamper, E. Gini, P. Besse, H. Melchior, B. Mikkelsen, K. Jepsen, M. Vaa, H. Poulsen, K. Stubkjaer, S. Bouchoule, and F. Devaux, "Novel technique for all-optical wavelength conversion of RZ pulses: penalty-free operation at 40 Gbit/s over the entire EDFA window using a monolithically integrated Mach-Zehnder interferometer with semiconductor optical amplifiers," Optical Amplifiers and Their Applications. Topical Meeting. OSA Trends in Optics and Photonics Series. Vol.16, pp. 270–3, 1997.

[34] O. Leclerc, P. Brindel, D. Rouvillain, B. Dany, R. Brenot, A. Labrousse, A. Coquelin, and B. Dagens, "Regenerated 40G bit/s long-haul transmission using all-optical SOA-MZI as loss-free synchronous modulator," Conference on Optical Fiber Communication, Technical Digest Series, vol. 54, no. 3, pp. WF6/1–WF6/3, 03/17-22/01.

[35] P. Cho, P. Sinha, D. Mahgerefteh, and G. Carter, "All-optical 2R-regeneration of 10 Gbit/s RZ data transmitted over 30000 km in a dispersion-managed system using an electroabsorption modulator," Optical Fiber Communication Conference, 2000, vol. 2, 7-10 March 2000.

[36] T. Yamamoto, E. Yoshida, and M. Nakazawa, "Ultrafast nonlinear optical loop mirror for demultiplexing 640 Gbit/s TDM signals," Electron. Lett., vol. 34, no. 10, pp. 1013 –1014, 1998.

[37] T. Morioka, H. Takara, S. Kawanishi, T. Kitoh, and M. Saruwatari, "Error-free 500 Gbit/s all-optical demultiplexing using low-noise, low-jitter supercontinuum short pulses," Electron. Lett., vol. 32, no. 9, pp. 833 –834, 1996.

[38] T. Morioka, H. Takara, S. Kawanishi, K. Uchiyama, and M. Saruwatari, "Polarization-independent all-optical demultiplexing up to 200 Gbit/s using four-wave mixing in a semiconductor laser amplifier," Electron. Lett., vol. 32, 1996.

[39] T. Tekin, M. Schlak, B. J. Brinker, W., C. Schubert, B. Maul, and R. Molt, "Ultrafast all-optical demultiplexing performance of monolithically intergrated band gap shifted Mach-Zehnder interferometer," Proceedings of ECOC 2001, Amsterdam, The Netherlands, vol. paper Th.F.1, 2001.

[40] M. Heid, S. Spalter, G. Mohs, A. Farbert, W. Vogt, and H. Melchior, "160-Gbis/s demultiplexing based on a monolithially integrated Mach-Zehnder interferometer," ECOC 2001. European Conference on Optical Communication, p. Th.B.4., 2001.

[41] C. Schubert, S. Diez, J. Berger, R. Ludwig, U. Feiste, H. Weber, G. Toptchiyski, K. Petermann, and V. Krajinovic, "160-Gb/S All-Optical Demultiplexing Using a Gain-Transparent Ultrafast-Nonlinear Interferometer (GT-UNI)," IEEE J. Photon. Technol. Lett., vol. 13, no. 5, pp. 475 –477, 2001.

[42] M. Eiselt, W. Pieper, and H. Weber, "SLALOM: Semiconductor Laser Amplifier in a Loop Mirror," IEEE J. Lightwave Technol., vol. 13, no. 10, pp. 2099 –2112, 1995.

[43] L. Oxenlowe, F. Romstad, A. Tersigni, S. Hojfeldt, K. Yvind, P. Skovgaard, K. Hoppe, and J. Hanberg, "Characterisation of a MQW electroabsorption modulator as an all-optical demultiplexer," Lasers and Electro-Optics Society, 2001. LEOS 2001. The 14th Annual Meeting of the IEEE, vol. 1, 12-13 November 2001.

[44] R. Y.-F. Yip, A. Ait-Ouali, A. Bensaada, P. Desjardins, M. Beaudoin, L. Isnard, J. L. Brebner, J. F. Currie, and R. A. Masut, "Strain and Relaxation Effects in InAsP/InP Multiple Quantum Well Optical Modulator Devices Grown by Metal-Organic Vapor Phase Epitaxy," J. Appl. Phys., vol. 81, no. 4, pp. 1905–1915, 1997.

[45] R.-F. Yip, P. Desjardins, L. Isnard, A. Ait-Ouali, H. Marchand, J. Brebner, J. Currie, and R. Masut, "Band Alignment Engineering for High Speed, Low Drive Field Quantum-Confined Stark Effect Devices," J. Appl. Phys., vol. 83, no. 3, pp. 1758–69, 1998.

[46] S. Højfeldt, Ph.D. Thesis, working title: Modeling of dynamical properties of electroabsorption modulators. Kongens Lyngby, DK-2800 Denmark: To be published, Technical University of Denmark, COM, 2002.

[47] L. Oxenløwe, Ph.D. Thesis, Optical signal processing with semiconductor components. Kgs. Lyngby, DK-2800 Denmark: To be published, Technical University of Denmark, COM, 2002.

[48] P. Andrekson, N. Olsson, T. Tanbun-Ek, R. Logan, D. Coblentz, and H. Temkin, "Novel technique for determining internal loss of individual semiconductor lasers," Electron. Lett., vol. 28, no. 2, pp. 171–2, 1992.

[49] K. Hall, G. Lenz, E. Ippen, and G. Raybon, "Heterodyne pump-probe technique for time-domain studies of optical nonlinearities in waveguides," Opt. Lett., vol. 17, no. 12, pp. 874–6, 1992.

[50] K. Hall, A. Darwish, E. Ippen, U. Koren, and G. Raybon, "Femtosecond index nonlinearities in InGaAsP optical amplifiers," Appl. Phys. Lett., vol. 62, no. 12, pp. 1320–2, 1993.

[51] K. Hall, G. Lenz, A. Darwish, and E. Ippen, "Subpicosecond gain and index nonlinearities in InGaAsP diode lasers," Opt. Commun., vol. 111, no. 67, pp. 589–612, 1994.

[52] M. Hofmann, S. Brorson, J. Mork, P. Skovgaard, J. McInerney, and A. Mecozzi, "Subpicosecond heterodyne four-wave mixing experiments on InGaAsP semiconductor laser amplifiers," Opt. Commun., vol. 139, no. 18, pp. 117–124, 1997.

[53] P. Borri, W. Langbein, J. Mork, and J. Hvam, "Heterodyne pump-probe and four-wave mixing in semiconductor optical amplifiers using balanced lock-in detection," Opt. Commun., vol. 169, no. 1-6, pp. 317–24, 1999.

[54] P. Borri, W. Langbein, J. Mork, J. Hvam, F. Heinrichsdorff, M.-H. Mao, and D. Bimberg, "Dephasing in InAs/GaAs quantum dots," Phys. Rev. B, vol. 60, no. 11, pp. 7784–7, 1999.

[55] P. Borri, W. Langbein, J. Hvam, F. Heinrichsdorff, M.-H. Mao, and D. Bimberg, "Ultrafast Gain Dynamics in InAs-InGaAs Quantum-Dot Amplifiers," IEEE J. Photon. Technol. Lett., vol. 12, no. 6, pp. 594 –596, 2000.

[56] P. Borri, S. Scaffetti, J. Mork, W. Langbein, J. Hvam, A. Mecozzi, and F. Martelli, "Measurement and calculation of the critical pulsewidth for gain saturation in semiconductor optical amplifiers," Opt. Commun., vol. 164, 1999.

[57] G. Agrawal, Fiber-optic communication systems. John Wiley and Sons, inc. New York, 2 ed., 1997.

[58] T. Wood, "Multiple Quantum Well (MQW) Waveguide Modulators," IEEE J. Lightwave Technol., vol. 6, no. 6, pp. 743 –757, 1988.

[59] G. Agrawal and N. Dutta, Long-wavelength semiconductor lasers. Van Nostrand Reinhold, 2 ed., 1986.

[60] C. Henry, "Theory Of the Linewidth of Semiconductor Lasers," IEEE J. Quantum Electron., vol. QE-18, no. 2, pp. 259–64, 1982.

[61] F. Dorgeuille and F. Devaux, "On The Transmission Performances and the Chirp Parameter of a Multiple-Quantum-Well Electroabsorption Modulator," IEEE J. Quantum Electron., vol. 30, no. 11, pp. 2565 –2572, 1994.

[62] N. Suzuki and Y. Hirayama, "Comparison of Effective /Spl Alpha/ Parameters for Multiquantum-Well Electroabsorption Modulators," IEEE J. Photon. Technol. Lett., vol. 7, no. 9, pp. 1007 –1009, 1995.

[63] J. Cartledge, "Comparison of Effective /Spl Alpha/-Parameters for Semiconductor Mach-Zehnder Optical Modulators," IEEE J. Lightwave Technol., vol. 16, no. 3, pp. 372 –379, 1998.

[64] R. A. Saunders, J. King, and I. Hardcastle Electronics Letters, vol. 30, p. 1336, 1994.

[65] O. Mitomi, K. Wakita, and I. Kotaka, "Chirping Characteristic of Electroabsorption-Type Optical-Intensity Modulator," IEEE J. Photon. Technol. Lett., vol. 6, no. 2, pp. 205 –207, 1994.

[66] C. Thirstrup, "Refractive Index Modulation Based on Excitonic Effects in GaInAs-InP Coupled Asymmetric Quantum Wells," IEEE J. Quantum Electron., vol. 31, no. 6, pp. 988 –996, 1995.

[67] F. Devaux, F. Dorgeuille, A. Ougazzaden, F. Huet, M. Carre, A. Carenco, M. Henry, Y. Sorel, J.-F. Kerdiles, and E. Jeanney, "20 Gbit/S Operation of a High-Efficiency InGaAsP/InGaAsP MQW Electroabsorption Modulator with 1.2-V Drive Voltage," IEEE J. Photon. Technol. Lett., vol. 5, no. 11, pp. 1288 –1290, 1993.

[68] T. Yamanaka, K. Wakita, and K. Yokoyama, "Pure strain effect on reducing the chirp parameter in InGaAsP/InP quantum well electroabsorption modulators," Appl. Phys. Lett., vol. 70, no. 1, pp. 87–9, 1997.

[69] F. Devaux, Y. Sorel, and J. Kerdiles, "Simple Measurement Of Fiber Dispersion and Of Chirp Parameter of Intensity Modulated Light Emitter," J. Lightwave Technol., vol. 11, no. 12, pp. 1937 –1940, 1993.

[70] S. Lin, P. Yu, and W. Chang, "Chirping of electroabsorption modulation in InGaAsP," Appl. Phys. Lett., vol. 55, no. 11, pp. 1100–2, 1989.

[71] H. Hou and T. Chang, "Nearly Chirp-Free Electroabsorption Modulation Using InGaAs-InGaAlAs-InAlAs Coupled Quantum Wells," IEEE J. Photon. Technol. Lett., vol. 7, no. 2, pp. 167 –169, 1995.

[72] J. Langanay, C. Starck, M. Boulou, M. Nicolardot, J. Emery, C. Fortin, P. Aubert, and D. Lesterlin, "Low spectral chirp and large electroabsorption in a strained InGaAsP/InGaAsP multiple quantum well modulator," Appl. Phys. Lett., vol. 62, no. 17, pp. 2066–8, 1993.

[73] J. Jeong and Y. Park, "Accurate determination of transient chirp parameter in high speed digital lightwave transmitters," Electron. Lett., vol. 33, no. 7, pp. 605 –606, 1997.

[74] J. Gopinath, E. Thoen, E. Koontz, M. Grein, L. Kolodziejski, E. Ippen, and J. Donnelly, "Recovery dynamics in proton-bombarded semiconductor saturable absorber mirrors," Appl. Phys. Lett., vol. 78, no. 22, pp. 3409–11, 2001.

[75] Z. Bakonyi, G. Onishchukov, C. Knoll, M. Golles, F. Lederer, and R. Ludwig, "In-Line Saturable Absorber in Transmission Systems with Cascaded Semiconductor Optical Amplifiers," IEEE J. Photon. Technol. Lett., vol. 12, no. 5, pp. 570 –572, 2000.

[76] I. Jung, F. Kartner, L. Brovelli, M. Kamp, and U. Keller, "Experimental verification of soliton mode locking using only a slow saturable absorber," Opt. Lett., vol. 20, no. 18, pp. 1892–4, 1995.

[77] J. R. Karin, R. J. Helkey, D. J. Derickson, R. Nagarajan, D. S. Allin, J. E. Bowers, and R. L. Thornton, "Ultrafast dynamics in field-enhanced saturable absorbers," Appl. Phys. Lett., vol. 64, no. 6, pp. 676–678, 1994.

[78] P. Smith, Y. Silberberg, and D. Miller, "Mode Locking of Semiconductor Diode Lasers Using Saturable Excitonic Nonlinearities," J. Opt. Soc. Am. B, vol. 2, no. 7, pp. 1228–36, 1985.

[79] S. Brorson, S. Bischoff, J. Mork, A. Moller-Larsen, and J. Nielsen, "Femtosecond Carrier Dynamics and Modelocking in Monolithic CPM Lasers," IEEE J. Photon. Technol. Lett., vol. 8, no. 10, pp. 1308 –1310, 1996.

[80] J. Karin, A. Uskov, R. Nagarajan, J. Bowers, and J. Mork, "Carrier heating dynamics in semiconductor waveguide saturable absorbers," Appl. Phys. Lett., vol. 65, no. 21, pp. 2708–10, 1994.

[81] K. Frojdh, S. Marcinkevicius, U. Olin, C. Silfvenius, B. Stalnacke, and G. Landgren, "Interwell carrier transport in InGaAsP multiple quantum well laser structures," Appl. Phys. Lett., vol. 69, no. 24, pp. 3695–7, 1996.

[82] A. Fox, D. Miller, G. Livescu, J. Cunningham, and W. Jan, "Quantum Well Carrier Sweep Out: Relation to Electroabsorption and Exciton Saturation," IEEE J. Quantum Electron., vol. 27, no. 10, pp. 2281–95, 1991.

[83] J. Cavailles, D. Miller, J. Cunningham, P. Wa, and A. Miller, "Simultaneous Measurements Of Electron And Hole Sweep-Out from Quantum Wells and Modeling of Photoinduced Field Screening Dynamics," IEEE J. Quantum Electron., vol. 28, no. 10, pp. 2486–97, 1992.

[84] I. Sizer, T., T. Woodward, U. Keller, K. Sauer, T.-H. Chiu, D. Sivco, and A. Cho, "Measurement of Carrier Escape Rates, Exciton Saturation Intensity, and Saturation Density in Electrically Biased Multiple-Quantum-Well Modulators," IEEE J. Quantum Electron., vol. 30, no. 2, pp. 399 –407, 1994.

[85] A. Miller, C. Park, and P. LiKamWa, "Time resolved measurements of cross-well transport in a multiple quantum well p-i-n modulator at high photogenerated carrier densities," Appl. Phys. Lett., vol. 60, no. 1, pp. 97–9, 1992.

[86] T. Yoshida, T. Hoshida, Y. Nasu, M. Kishi, and M. Tsuchiya, "Experimental investigation on carrier dynamics in SCH-MQW waveguide saturable absorber of passively mode-locked monolithic laser diode," Optical and Quantum Electronics, vol. 33, no. 7, 2001.

[87] A. Uskov, J. Karin, R. Nagarajan, and J. Bowers, "Dynamics of Carrier Heating and Sweepout in Waveguide Saturable Absorbers," IEEE J. Quantum Electron., vol. 1, no. 2, pp. 552 –561, 1995.

[88] M. Suzuki, H. Tanaka, and S. Akiba, "Effect of hole pile-up at heterointerface on modulation voltage in GaInAsP electroabsorption modulators," Electron. Lett., vol. 25, no. 2, pp. 88 –89, 1989.

[89] J. Zhang, M. Yao, X. Chen, L. Xu, M. Chen, and Y. Gao, "Bit Error Rate Analysis of OTDM System Based on Moment Generation Function," IEEE J. Lightwave Technol., vol. 18, no. 11, pp. 1513–18, 2000.

[90] M. Vaa, Ph.D. Thesis, Optical Time Division Multiplexing for High Capacity Photonic Networks. Kgs. Lyngby, DK-2800 Denmark: Technical University of Denmark, Dept. of Electromagnetic Systems, 1997.

[91] P. Borri, F. Romstad, W. Langbein, A. Kelly, J. Mork, and J. Hvam, "Separation of coherent and incoherent nonlinearities in a heterodyne pump-probe experiment," Optics Express, vol. 7, no. 3, 2000.

[92] J. Mork, A. Mecozzi, and C. Hultgren, "Spectral effects in short pulse pump-probe measurements," Appl. Phys. Lett., vol. 68, no. 4, pp. 449–51, 1996.

[93] C. Hultgren and E. Ippen, "Ultrafast refractive index dynamics in AlGaAs diode laser amplifiers," Appl. Phys. Lett., vol. 59, no. 6, pp. 635–7, 1991.

[94] J. Karin, Ph.D. Thesis, Ultrafast Dynamcs in Semiconductor Laser Structures. Departement of Electrical and Computer Engineering, University of California at Santa Barbara, 1994.

[95] L. Brovelli, J. Hugi, H. Jackel, and H. Melchior, "Optical Pulse Mixing Measurement of Carrier Lifetime and Absorption Recovery Time in Reverse-Biased GaAs/AlGaAs Single Quantum Well Laser Structures," J. Appl. Phys., vol. 76, no. 12, pp. 7713–19, 1994.

[96] H. Tsang, P. Vasil'ev, I. White, R. Penty, and J. Aitchison, "First demonstration of two photon absorption in a semiconductor waveguide pumped by a diode laser," Electron. Lett., vol. 29, no. 18, pp. 1660 –1661, 1993.

[97] L. Spiekman, U. Koren, M. Chien, B. Miller, J. Wiesenfeld, and J. Perino, "All-Optical Mach-Zehnder Wavelength Converter with Monolithically Integrated DFB Probe Source," IEEE J. Photon. Technol. Lett., vol. 9, no. 10, pp. 1349 –1351, 1997.

[98] C. Harder, K. Vahala, and A. Yariv, "Measurement of the linewidth enhancement factor alpha of semiconductor lasers," Appl. Phys. Lett., vol. 42, no. 4, pp. 328–30, 1983.

[99] T. Durhuus, B. Mikkelsen, C. Joergensen, S. Lykke Danielsen, and K. Stubkjaer, "All-Optical Wavelength Conversion by Semiconductor Optical Amplifiers," IEEE J. Lightwave Technol., vol. 14, no. 6, pp. 942 –954, 1996.